이학박사 학위논문

Self-Assembling Polymers for Plasmonic Applications in Nanostructured Materials

나노소재의 플라즈모닉 응용을 위한

자기조립 고분자에 관한 연구

2012 년 8 월

서울대학교 대학원

화학부 고분자화학

김 기 세

Self-Assembling Polymers for Plasmonic Applications in Nanostructured Materials

지도 교수 손 병 혁

이 논문을 이학박사 학위논문으로 제출함
2012 년 8 월

서울대학교 대학원
화학부 고분자화학
김 기 세

김기세의 박사 학위논문을 인준함
2012 년 8 월

위 원 장 이 진 규 (인)

부위원장 손 병 혁 (인)

위 원 남 좌 민 (인)

위 원 최 태 림 (인)

위 원 Rudolf Zentel (인)

Abstract

Self-Assembling Polymers for Plasmonic Applications in Nanostructured Materials

Ki-Se Kim

Department of Chemistry

The Graduate School

Seoul National University

Controlling the near-field interactions among the fluorescent dyes, semiconductor quantum dots (QDs), and metal nanoparticles (NPs) is a key factor in a wide range of applications, such as photonic, plasmonic, nano, and bio system. For examples, such photonic coupling among multiple fluorophores as fluorescence resonance energy transfer (FRET) has been utilized for optoelectronic devices, including organic photovoltaic cells and light-emitting diodes, in which efficient light harvesting and energy transfer from donor to acceptors play a critical role for device performance. In addition, the collective oscillation of electrons in metal NPs known as localized surface plasmon resonances (LSPRs) gained much attention since light-matter interaction can be engineered by positioning metal NPs in the vicinity of fluorophores such as fluorescent dyes, QDs, and conjugated

polymers. In this context, LSPRs excitation results in significantly enhanced local fields at the metal NPs and engineer the radiative decay and non-radiative decay rate of fluorophores, which give rise to fundamentally interesting phenomena as plasmon-enhanced fluorescence, plasmon-enhanced FRET, nanometal surface energy transfer (NSET), surface plasmon amplification by stimulated emission of radiation (SPASER), and so on. The consequences of this understanding now open widespread possibilities in optoelectronics, optics, cell-imaging, and biology.

Since photonic coupling among fluorescent dyes, QDs, and metal NPs strongly depends on their mutual distance and position in a nanometer scale, the precise control on their relative location in a thin film is crucial to achieve novel photoluminescence properties for photonic applications. Polymeric self-assemblies of block copolymer micelles and Layer-by-Layer (LbL) assemblies of polyelectrolytes can be a promising solution for the effective control over the position of photonic materials with the nanoscale precision in a thin film.

In this thesis, we demonstrate how to utilize nanostructures of self-assembling polymers to effectively control the near-field interactions such as FRET, NSET, and surface-plasmon-coupled fluorescence among photonic nanomaterials in thin films.

In Chapter 1, we demonstrated controlled light emission from thin films having two different fluorescent dyes in separate layers by the LbL

assembling methods. Based on spectral overlap between fluorescent dyes, we selected rhodamine 123 (R123) and rhodamine B (RB) as the donor and acceptor, respectively. Before LbL deposition, a complex consisting of each dye and polyelectrolytes was first prepared. Multilayered thin films consist of alternate layers of oppositely charged polyelectrolytes. In the deposition procedure, a complex of R123 (or RB) and polyelectrolytes was incorporated into a layer of multilayered thin films. By adjusting the number of polyelectrolyte layers between R123 and RB, the distance between them was precisely controlled, leading to tune the light emission from the multilayered thin film by the controlled FRET.

In Chapter 2, we described precise control of multiple FRET within LbL assemblies to produce simultaneous light emission with enhanced intensity from a single excitation with a blue wavelength. Three different fluorescent dyes were attached to neat polyelectrolytes and then incorporated into the LbL assembly. With designed deposition sequence, the layer of blue-absorbing dyes was placed in the adjacent layer of green- and red-emitting dyes, while the layers of emitting dyes were separated with each other beyond their Förster radius by inserting neat polyelectolytes between them. The LbL assemblies not only allowed FRET from the absorbing dyes to the emitting dyes but also prohibited FERT between the emitting dyes to produce simultaneously enhanced green and red emission.

In Chapter 3, we discussed the strong correlation of micellar structures with surface-plasmon-coupled fluorescence. The inherent self-segregating property of block copolymer micelles sets clear bounds for the arrangement of fluorophores in the vicinity of metal nanoparticles for the fluorescence enhancement that would not be easily achieved by other assembling methods. A single-layered film of block copolymer micelles with fluorescent dyes was fabricated on Ag NP substrate. In this film, dyes were located in the micellar core whereas Ag NPs around the corona of micelles. Thus, the mutual distance between dyes and NPs was controlled by adjusting the size of copolymer micelles to achieve the fluorescence enhancement by Ag NPs. Moreover, with the same micellar nanostructure, simultaneous emission of two different dyes with enhanced intensity was produced by isolating them in different micelles, the corona structure of which worked as an effective blockade for FRET between two dyes. These features of copolymer micelles can find many opportunities in plasmonic applications. Relevance-future direction can be suggested as the modification of chemical structures of the copolymer to form a thin metal on the micelles. By coating metal shells on the coronas of micelles that contain dyes in the cores, dual functionalities of plasmon and fluorescence might be achieved, which can be a promising blueprint for cell-imaging and diagnostics.

In Chapter 4, we investigated the near-field interactions among QDs, dyes, and metal NPs in nanostructured micellar thin films. It has been noticed

that surface plasmon resonance of metal NPs can alter the intrinsic properties of nearby fluorophores. Field enhancement and radiative decay engineering are major principles for understanding a number of experimental observations such as enhanced and quenched emission of fluorophores in the vicinity of metal NP. At the same time, there are apparent similarities between surface-plasmon-coupled fluorescence and FRET as both are near-field through-space interactions. From this perspective, we hypothesize that donor-acceptor interaction in the FRET can be altered by metal nanoparticles. Our approach is based on diblock copolymer micelles which have been widely applied for nanoscale arrangement of functionalities. By applying self-assembling techniques of copolymer micelles to organize the spatial location of semiconductor quantum dots, fluorescent dyes, and metal nanoparticles, the FRET in hybrid assemblies can be switched off by plasmonic effects.

Keywords: Self-Assembly, Block Copolymer Micelles, Layer-by-Layer Assembly, Fluorescence, Surface Plasmon

Student Number: 2006-20355

Contents

List of Figures

Chapter 1

Chapter 2

Chapter 3

Chapter 4

List of Tables

Chapter 3

Chapter 4

Chapter 1

Controlled Light Emission in Spin-Assisted Layer-by-Layer Assemblies with Fluorophores

1.1. Introduction

Fluorescence resonance energy transfer (FRET) involves non-radiative energy transfer from excited-state donors to ground-state acceptors through dipole–dipole interactions, which strongly depend on the distance between donors and acceptors.[1] FRET between fluorophores has been widely utilized in the manufacture of efficient optoelectronic devices such as solar cells and organic light-emitting diodes, in which conveying processes of absorbed energy from donors to acceptors play a critical role.[2–5] The successful application of energy-transferring processes, however, requires the accurate organization of donors and acceptors in nanometer-scale precision as well as the placement of fluorophores in a thin film.

To place fluorophores at a specific location in a thin film, synthetic nanostructures such as dendrimers,[6] block copolymer micelles,[7] zeolites,[8] sol–gel thin films,[9] and layer-by-layer thin films[10-12] can be employed. In particular, the layer-by-layer (LbL) assembling method, which is based on the spontaneous ionic adsorption of oppositely charged materials, can be utilized to fabricate multilayered films with fluorophores.[10–17] The LbL technique is an extremely simple process because of its self-assembling nature. But it can create tailored multilayered thin films by incorporating functional species.[18,19] A variety of donor–acceptor pairs of fluorescent dyes that are either pre-complexed with polyelectrolytes,[10,11] multiply charged by themselves,[12–14] or covalently attached to polyelectrolytes[15–17] have been incorporated into a layer of multilayered thin films by alternating deposition with polyelectrolytes. Since FRET is strongly dependent on the distance

between donors and acceptors,[1] the emission from multilayered films can be effectively tuned by adjusting the deposition sequences of layers of donors and acceptors with respect to each other.[13–17] Although the conventional dip LbL method can be employed to fabricate multilayered thin films with fluorescent dyes, the spin-assisted LbL method can be effective in terms of minimizing the interpenetration between layers and the unwanted release or penetration of dyes into the assembly during the dipping process.[10,20] In addition, the spin-assisted LbL method facilitates the rapid fabrication of multilayered thin films with a well-ordered structure.[21]

In this study we report upon the precise control of light emissions from spin-assisted LbL assemblies containing a donor-acceptor pair of fluorescent dyes. We selected rhodamine 123 (R123) and rhodamine B (RB) as the donor and acceptor, respectively. Before LbL deposition, a complex consisting of each dye and polyelectrolytes was first prepared. Multilayered thin films consist of alternate layers of oppositely charged polyelectrolytes. In the deposition procedure, a complex of R123 (or RB) and polyelectrolytes was incorporated into a layer of multilayered thin films. By adjusting the number of polyelectrolyte layers between R123 and RB, the distance between them was precisely controlled, leading to tune the light emission from the multilayered thin film by the controlled FRET.

1.2. Experimental Section

Poly(allyamine hydrochloride) (PAH, Mw = 70,000 g/mol), poly(styrene 4-sulfonate) (PSS, Mw = 70,000 g/mol), rhodamine 123 (R123), and rhodamine B (RB) were purchased from Sigma-Aldrich and were used as received. For LbL deposition, PAH and PSS were dissolved in deionized water to yield 0.01 M solutions. R123 (or RB) was added to an aqueous solution of PSS and stirred for at least 24 hr to form a complex of PSS and R123 (or RB). The molar ratios of R123 and RB to PSS were 0.01 and 0.1, respectively. Silicon wafers and quartz plates were cleaned in a piranha solution (70/30 v/v of concentrated H_2SO_4 and 30-% H_2O_2) to create a negatively charged surface.[22] LbL assemblies were fabricated by the sequential deposition of oppositely charged polyelectrolytes by spin coating, typically at 3000 rpm for 30 sec. Prior to the deposition of a luminescent layer of PSS complexed with R123 (or RB), introductory layers consisting of five [PAH/PSS] bilayers were first prepared to ensure a uniform surface charge on the substrate. After the deposition of each layer, there was a washing step with deionized water.

UV-Vis spectra were obtained on a Sinco-3100 spectrophotometer. Photoluminescence (PL) was measured on an Acton Spectra Pro with a 500 W Xenon light source. The thickness of the thin films was measured by ellipsometry (Gatner Scientific, L2W15S380) with a 632.8 nm He-Ne laser.

1.3. Results and Discussion

To incorporate a fluorescent dye into an LbL assembly, an interpolyelectrolyte complex of a dye (R123 and RB) having a charge with a polyelectrolyte (PSS) having multiple charges was employed. Figure 1.1 shows the molecular structures of the PAH, PSS, R123 and RB used in this study. Although we selected these molecules as a model system, a variety of fluorescent dyes and polyelectrolytes can be utilized to control the FRET in order to tune the emitting light by means of the methodology that we will demonstrate. Since multiple charges are necessary as building material for an LbL assembly,[18,19] neither R123 nor RB can be used to form an LbL assembly with PSS, as they each have a single positive charge. However, a complex of this dye with a negatively charged PSS can form an alternating multilayer with a positively charged PAH, because some negative charges remain in the PSS after the formation of the complex with R123 or RB.[10,11] Moreover, we can adjust the amount of dyes in each layer by varying the molar ratio of the dye to the polyelectrolyte when we prepare their interpolyelectrolyte complex. UV-Vis (dashed line) and PL (solid line) spectra of PSS-dye complexes in an aqueous solution are shown in Figure 1.2. The concentration of the PSS-dye complex was 0.01 M, and the molar ratio of the dye to the repeat unit of PSS was 0.001. Hereafter, a complex of PSS with R123 (or RB) will be called simply as PSS-R123 (or PSS-RB). The maximum absorption and emission of PSS-R123 are located at 510 nm and 540 nm (green emission), respectively, whereas those of PSS-RB at 560 nm and 590 nm (orange-red emission), respectively. The excitation wavelength for the PL

spectra was 460 nm. Because the emission spectrum of PSS-R123 overlaps well with the absorption spectrum of PSS-RB, we utilized PSS-R123 as a donor and PSS-RB as an acceptor. Based on the Förster formalism,[1] the Förster radius can be calculated by

$$R_0 = [9000(\ln 10)k^2 Q_D J / 128\pi^5 n^4 N_{AV}]^{1/6} \quad \text{---------- Eq. (1.1)}$$

where Q_D is the fluorescence quantum yield of the donor, k^2 describes the dipole orientation of the donor relative to the acceptor, n is the refractive index of the medium, and J is the donor-acceptor overlap integral.

The overlap integral can be calculated by

$$J = \int_0^\infty f_D(\lambda)\varepsilon_A(\lambda)\lambda^4 d\lambda \quad \text{---------- Eq. (1.2)}$$

where $f_D(\lambda)$ is the normalized emission intensity of the donor, $\varepsilon_A(\lambda)$ is the wavelength dependent extinction coefficient of the acceptor, and λ is the wavelength. The value used for Q_D, n, and J are 0.80, 1.54, and 3.31 × 10^{15} ($M^{-1}cm^{-1}nm^4$), respectively. We assume that the value of k^2 is 2/3, which is the average orientation factor in solution. The Forster radius derived from these values is 5.5 nm. If all dye molecules are aligned parallel to the plane of the film, the value of k^2 can be increased to 0.895,[23] resulting in a Forster radius of 5.8 nm. The error range can be ~5 % in the Foster radius associated with the value of k^2.

For an LbL assembly, the concentration was adjusted to 0.01 M for both PSS-R123 and PSS-RB. However, the molar ratio of the dye to the repeat unit of PSS was 0.01 for PSS-R123 and 0.1 for PSS-RB in order to obtain

similar emission intensities for both complexes because of the higher quantum yield of PSS-R123 (~ 0.8), as compared to that of PSS-RB (~ 0.28). PSS-dye complexes were alternately assembled with a positive PAH polyelectrolyte by the spin-assisted LbL method which can be better than the dip LbL method here in terms of minimizing the inter-penetration between layers and the unwanted release or penetration of dyes in the assembly during the dipping process.[10,20]

In the LbL assembly of $[PAH/PSS\text{-}R123]_n$ (n = the number of bilayers), the absorption of R123 at 510 nm increases linearly with the increase in the number of bilayers (Figure 1.3a). This indicates that an equal amount of R123 was incorporated into the assembly by each deposition step of the PSS-R123 layer. The regular deposition of RB into the assembly was also confirmed by the linear increase in the absorbance of RB at 560 nm (Figure 1.3b). We note that the higher molar absorption of RB than R123 was responsible for the higher slope of RB in the plots in Figure 1.3. The equal deposition of dyes by each assembling step was also verified by PL spectra with an increase in the number of bilayers, which is shown in Figure 1.4.

In both LbL assemblies with PSS-R123 and RSS-RB, PL spectra increase with an increase in the number of [PAH/PSS-dye] bilayers, as shown in Figure 1.4. The linear increase of the maximum intensities at 540 nm for R123 and at 590 nm for RB as shown in the insets confirms the equal deposition of dyes by each assembling step. In addition, the maximum of PL spectra remained at the same wavelength peak as the number of bilayers increased, implying that it is not necessary to consider the aggregation of dyes

between layers, which can cause a red shift of the spectra. From the UV-Vis and PL spectra with the increase of the [PAH/PSS-dye] bilayer (Figures 1.3 and 1.4), we confirmed that a regular amount of dye can be incorporated into the LbL assembly at each deposition step. This is crucial to the study of the FRET between PSS-R123 and PSS-RB, where the space between them is varied by using the LbL assembling method.

By the ellipsometry, we also measured the increase of the thickness as the number of the bilayers increased (Figure 1.5). Regardless of the type of the bilayer, whether [PAH/PSS-R123], [PAH/PSS-RB] or [PAH/PSS], the thickness of the assembly increased linearly and fit into a single slope, indicating that all the bilayers had an equal thickness of 2.6 nm, because a small amount of dye in the PSS-dye layer did not affect the thickness of the bilayer. By measuring the thickness after the deposition of each single layer, the thickness of a single PAH layer was 0.7 nm, whereas that of a single PSS layer was 1.9 nm.

In order to tune the light emission by controlling the FRET between PSS-R123 and PSS-RB, we designed the layers in the LbL assemblies as shown in the schematics of Figure 1.6. Since the spin-assisted LbL assembling technique can provide precise control over the thickness between layers, we varied the distance between the PSS-R123 layer and the PSS-RB layer by the number of [PAH/PSS] layers. The bilayers without dyes essentially work as a spacer between the donors and acceptors. In the schematic, PSS-R123 and PSS-RB are represented by a green and a red layer, respectively. PAH is marked as a gray layer, whereas PSS without dyes as a bright blue layer. Thus,

a bilayer with PSS-R123, PSS-RB, or PSS always comes with PAH. We first deposited an acceptor of the [PAH/PSS-RB] bilayer and the desired number of [PAH/PSS] spacers, and then, a donor of the [PAH/PSS-R123] bilayer. The number of [PAH/PSS] spacers (*n*) is controlled to 0, 1, 2, 4, and 8. We note that the total spacer between the PSS-R123 donor and the PSS-RB acceptor is $[PAH/PSS]_n$ layers and a single PAH layer because of the donor layer consisting of a single PAH layer and a single PSS-R123 layer. In all cases, five [PAH/PSS] bilayers were first coated on the substrate before constructing LbL assemblies. The PL spectra of each LbL assembly in the schematics in Figure 1.6 are shown in Figure 1.7. We note that each PL measurement was performed with a triply repeated LbL assembly of each schematic of Figure 1.6 with the same number of [PAH/PSS] spacers between the repeats as that in each LbL assembly to obtain reliable PL intensities.

In Figure 1.7a, the PL spectra of the LbL assemblies of [PAH/PSS-R123] and [PAH/PSS-RB] are shown as green and red curves, respectively. The maximum emission intensity of [PAH/PSS-R123] is slightly higher than that of [PAH/PSS-RB], although we adjusted the molar ratio of the dye to the repeat unit of PSS to obtain similar emission intensities. When the [PAH/PSS-R123] and [PAH/PSS-RB] bilayers were directly contacted without a spacer (Figure 1.6b), an intense emission of RB around 590 nm with a decreased emission of R123 around 540 nm was observed (Figure 1.7b) because of the FRET from R123 to RB by their close contact, although the emission of R123 was not completely quenched. Since both R123 and RB formed complexes with a negative PSS, a layer of positive PAH between PSS-R123 and PSS-RB

was necessary for the construction of the LbL assembly, which did not allow direct contact between PSS-R123 and PSS-RB. Thus, the PAH layer between PSS-R123 and PSS-RB can be partly responsible for the weak emission of R123 in Figure 1.7b.

As the number of the [PAH/PSS] space layer increases (Figsure 1.6c～f), the emission intensity of R123 increases (Figsure 1.7c～f) and finally becomes the same as that of [PAH/PSS-R123] because of the restricted FRET as a result of the large separation between PSS-R123 and PSS-RB. The emission intensity of RB also decreased accordingly. We note that the maximum position of the RB emission was slightly changed in each LbL assembly, although that of R123 remained at the same wavelength. A clear explanation of the variations in the peak position of RB cannot be given in the current state.

The distance between the distance between R123 and RB can be estimated either by calculation of the FRET efficiency from the PL spectra (Figure 1.7) or by direct measurement of the layer thickness by ellipsometry (Figure 1.5). From the PL spectra, we can evaluate the FRET efficiency (Φ) by $\Phi = 1 - E_{DA} / E_D$, where E_{DA} and E_D are the integrated intensities of the donor emission with and without an acceptor, respectively.[14-16] E_D can be obtained from the R123 emission in Figure 1.7a. E_{DA} can be also acquired from the R123 emission in Figure 1.7b～f by the process of deconvolution. The FRET efficiency (Φ) can be estimated as 0.94 (n = 0), 0.53 (n = 1), 0.31 (n = 2), 0.13 (n = 0), and 0.004 (n = 8). Then, the distance

between donors and acceptors can be calculated by $\Phi = R_0^4/(R_0^4 + r^4)$, where R_0 and r are Förster radius and the donor-to-acceptor distance, respectively.[14-16] The estimated distance between R123 and RB in the LbL assembly of [PAH/PSSRB]/[PAH/PSS]$_n$/[PAH/PSS-R123] from the PL spectra (Figure 1.7) is 2.7 nm (n = 0), 5.3 nm (n = 1), 6.7 nm (n = 2), 8.7 nm (n = 4), and 21.2 nm (n = 8). The error range in the calculated distance can be ~5 %, which is associated to the assumption in the calculation of the Förster radius as well as the deconvolution process in the calculation of the FRET efficiency.

In addition, the distance between R123 and RB can be evaluated from the layer thickness by ellipsometry. We assumed that the distance between R123 and RB is the same as the center-to-center distance between the PSS-R123 layer and the PSS-RB layer. Consequently, it was estimated as 2.6 nm (n = 0), 5.2 nm (n = 1), 7.8 nm (n = 2), 13.0 nm (n = 4), and 23.4 nm (n = 8). These values are more or less in agreement with those obtained from the PL spectra. However, the donor-to–acceptor distance estimated from the PL spectra is more reliable because the PL spectrum basically reflects the actual distribution of R123 and RB in the LbL assembly.

With the estimated donor-to-acceptor distances, the PL spectra in Figure 1.7 can then be explained. Without the [PAH/PSS] spacer (Figure 1.7b), the distance between R123 and RB was close enough to allow the FRET, resulting in the intense emission of RB acceptors with the quenched emission of R123. As the number of [PAH/PSS] spacers increased, the distance

between R123 and RB became larger than the Förster radius, leading to the restricted FRET. Thus, as shown in the PL spectra of Figures 1.7c to 1.7f, a gradual increase in R123 emission as well as a gradual decrease in RB emission was evident. With eight [PAH/PSS] spacers (Figure 1.7f), the distance between R123 and RB is much larger than the Förster radius. Thus, there was no energy transfer from R123 and RB, resulting in a combined PL spectrum composed of the two independently measured spectra of R123 and RB shown in Figure 1.7a. Therefore, the LbL assembling method enabled the precise control on the distance between R123 donors and RB acceptors to tune the light emission from the multilayered thin film by the controlled FRET.

1.4. Conclusion

We demonstrated the precise control of the FRET in spin-assisted LbL assemblies containing a donor–acceptor pair of fluorescent dyes. Since the LbL assembly of a donor of R123 and an acceptor of RB can be independently fabricated, we incorporated them into the same LbL assembly with a sequence of [PAH/PSSRB]/[PAH/PSS]$_n$/[PAH/PSS-R123]. By controlling the number of [PAH/PSS] bilayers from 0 to 8, the distance between the PSS-R123 layer and the PSS-RB layer was adjusted from 2.7 nm to 21.2 nm. Since the FRET was strongly dependent on the distance between donors and acceptors, the efficiency of the FRET was controlled from 0.94 to 0.004, which resulted in tuned light emissions from the thin films. When the

number of [PAH/PSS] spacers was large enough to separate R123 and RB beyond their Förster radius (5.5 nm), the FRET was effectively restricted, resulting in simultaneous emission from both R123 and RB. When the number of [PAH/PSS] spacers was decreased, the donor-to-acceptor distance was reduced accordingly, resulting in a decrease in R123 donor emission as well as an increase in RB acceptor emission.

1.5. References

[1] J. R. Lackowicz, *Principles of Fluorescence Spectroscopy*, Plenum, New York, **1983**.

[2] A. F. Nogueira, C. Longo, M. A. De Paoli, *Coord. Chem. Rev*. **2004**, *248*, 1455.

[3] U. Bach, D. Lupo, P. Comte, J. E. Moser, F. Weissörtel, J. Saleck, H. Spreitzer, M. Grätzel, *Nature* **1998**, *395*, 583.

[4] M. A. Baldo, M. E. Thompson, S. R. Forrest, *Nature* **2000**, *403*, 750.

[5] A. A. Shoustikov, Y. You, M. E. Thompson, *IEEE J. Sel. Top. Quantum Electron* **1998***, 4*, 3.

[6] a) T. Weil, E. Reuther, K. Mullen, *Angew. Chem. Int. Ed*. **2002**, *41*, 1900; b) A. Adronov and J. M. J. Frechet, *Chem. Commun.* **2000***,* 1701.

[7] a) S. I. Yoo, J. H. Lee, B. H. Sohn, I. Eom, T. Joo, S. J. An, G. C. Yi, *Adv. Funct. Mater.* **2008**, *18*, 2984; b) S. I. Yoo, S. J. An, G. H. Choi, K. S. Kim, G. C. Yi, W. C. Zin, J. C. Jung, B. H. Sohn, *Adv. Mater.* **2007***, 19*, 1594.

[8] Y. Wada, M. Sato, and Y. Tsukahara, *Angew. Chem. Int. Ed.* **2006**, *45*, 1925.

[9] P. N. Minoofar, B. S. Dunn, J. I. Zink, *J. Am. Chem. Soc.* **2005***, 17*, 2656.

[10] H. Chen, G. Zeng, Z. Wang, X. Zhang, M. L. Peng, L. Z. Wu, C. H. Tung, *Chem. Mater.* **2005***, 17*, 6679.

[11] S. Das, A. J. Pal, *Langmuir* **2002**, *18*, 458.

[12] K. Ariga, Y. Lvov, T. Kunitake, *J. Am. Chem. Soc.* **1997**, *119*, 2224.

[13] T. Tang, J. Qu, K. Müllen, and S. E. Webber, *Langmuir* **2006**, *22*, 7610.

[14] W. J. Baur, M. F. Rubner, J. R. Reynolds, S. H. Kim, *Langmuir* **1999**, 15, 6460 .

[15] G. M. Lowman, N. Daoud, R. M. Case, P. J. Carson, S. K. Buratto, *Nano Lett.* **2001**, *1*, 677.

[16] B. Richter and S. Kirsein, *J. Chem. Phys.* **1999**, *111*, 5191.

[17] D. M. Kaschak and T. E. Mallouk, *J. Am. Chem. Soc.* **1996**, *118*, 4222.

[18] P. T. Hammond, *Adv. Mater.* **2004**, *16*, 1271.

[19] G. Decher, *Science* **1997**, *277*, 1232.

[20] C. Tedeschi, F. Caruso, H. Molhwald, and S. Kirstein, *J. Am. Chem. Soc.* **2000**, *122*, 5841.

[21] a) P. A. Chiarelli, M. S. Johal, J. L. Casson, J. B. Roberts, J. M. Robinson, H. L. Wang, *Adv. Mater.* **2001**, *13*, 1167; b) J. H. Cho, K. H. Char, J. D. Hong, and K. B. Lee, *Adv. Mater.* **2001**, *13*, 1076.

[22] B. H. Sohn, T. H. Kim, and K. H. Char, *Langmuir* **2002**, *18*, 7770.

[23] J. Baumann, M. D. Fayer, *J. Chem. Phys*. **1986**, *85*, 4087.

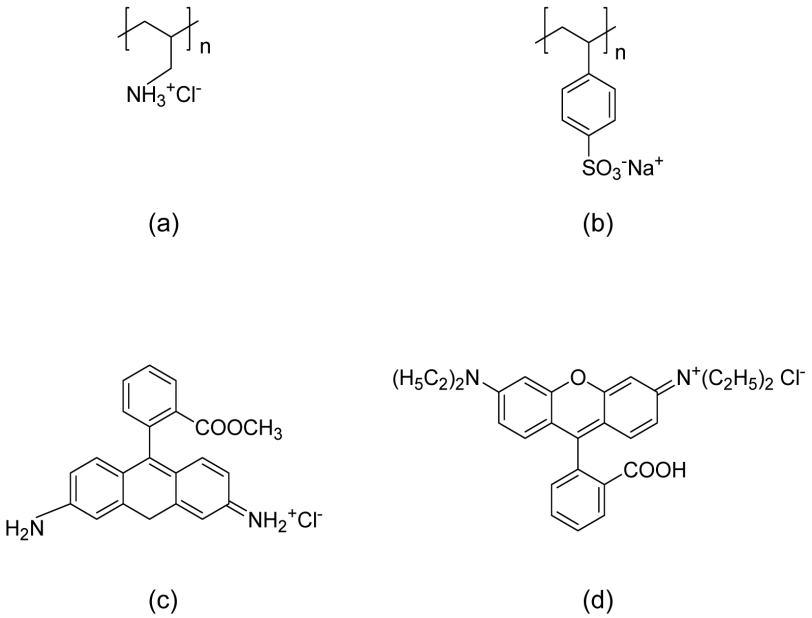

Figure 1.1. Molecular structure of polyelectrolytes and fluorescent dyes: (a) poly(allyamine hydrochloride) (PAH); (b) poly(styrene sulfonate) (PSS); (c) rhodamine 123 (R123); (d) rhodamine B (RB).

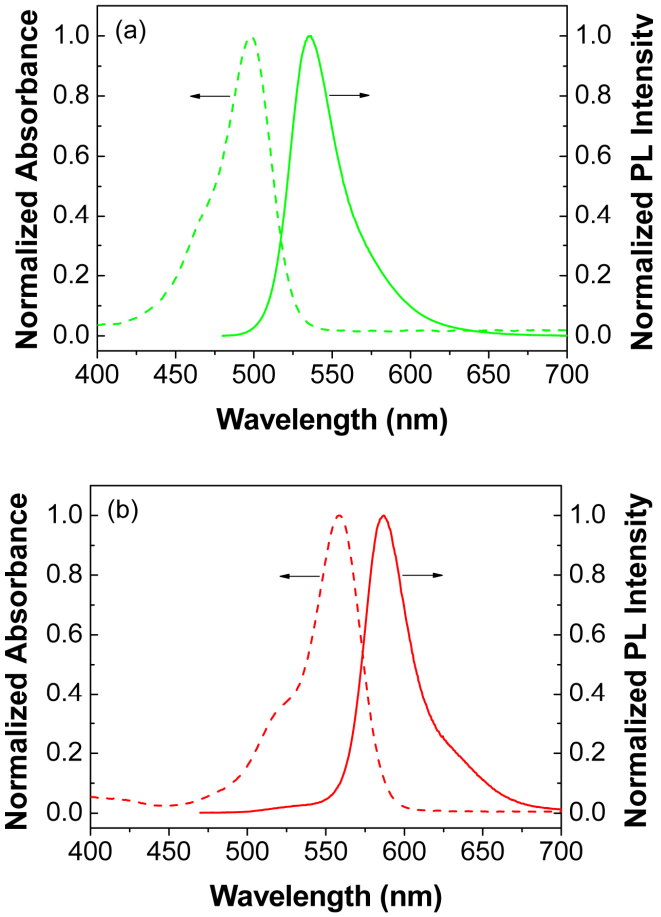

Figure 1.2. Normalized UV-Vis (dashed line) and PL (solid line) spectra of PSS-dye complexes in an aqueous solution: (a) PSS-R123; (b) PSS-RB. The concentration of the PSS-dye complex was 0.01 M and the molar ratio of the dye to the repeat unit of PSS was 0.001. The excitation wavelength was 460 nm.

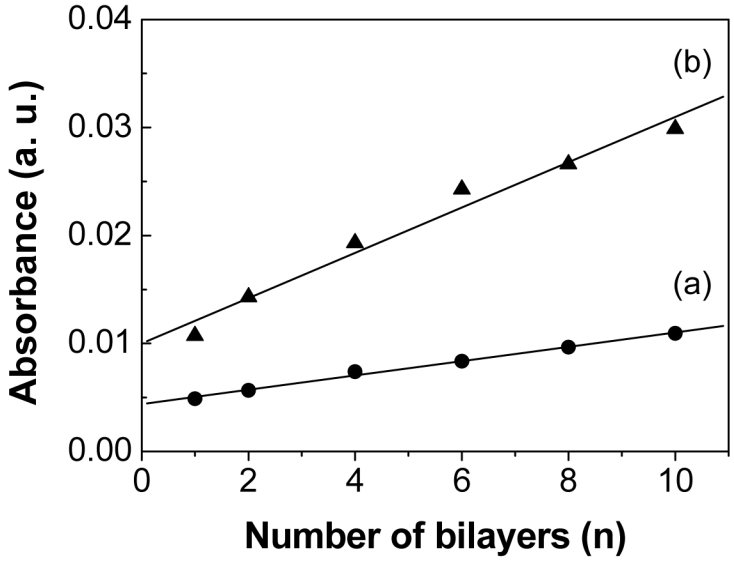

Figure 1.3. Absorbance as a function of the number of bilayers: (a) $[PAH/PSS\text{-}R123]_n$ at 510 nm; (b) $[PAH/PSS\text{-}RB]_n$ at 560 nm.

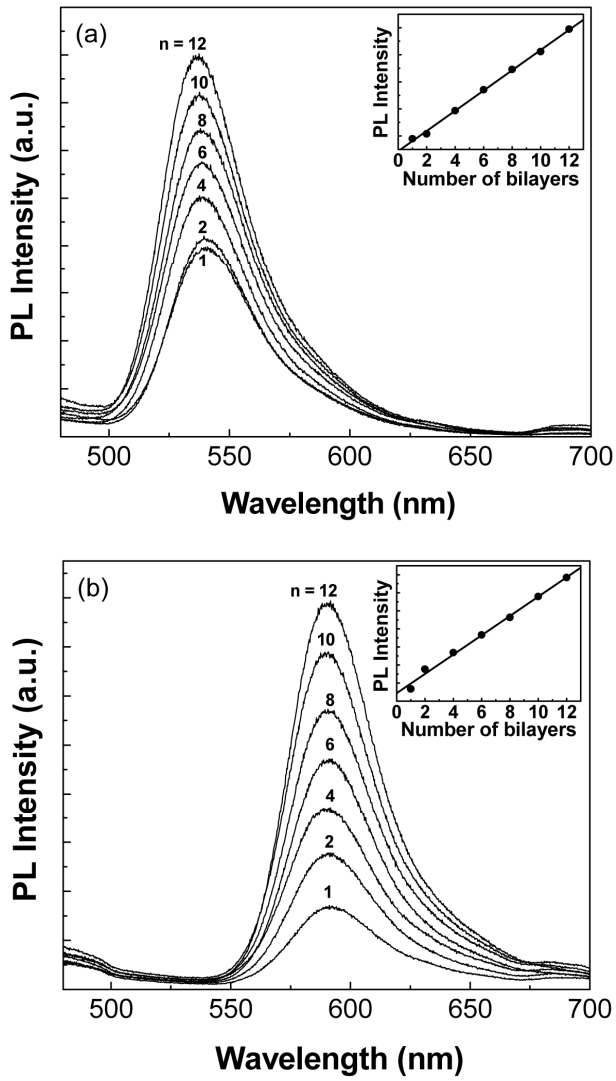

Figure 1.4. PL spectra as a function of the number of bilayers: (a) $[PAH/PSS\text{-}R123]_n$; (b) $[PAH/PSS\text{-}RB]_n$. PL intensities at 540 nm and at 590 nm as a function of the number of bilayers are inserted in (a) and (b), respectively. The excitation wavelength was 460 nm.

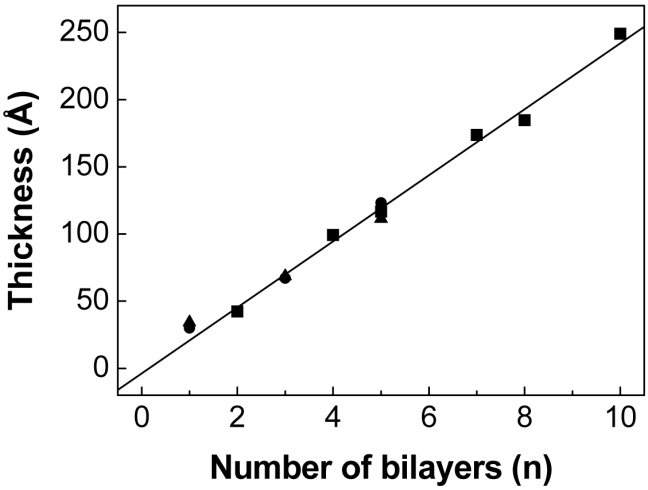

Figure 1.5. Film thickness as a function of the number of bilayers in $[PAH/PSS\text{-}R123]_n$ (●), $[PAH/PSS\text{-}RB]_n$ (▲), and $[PAH/PSS]_n$ (■).

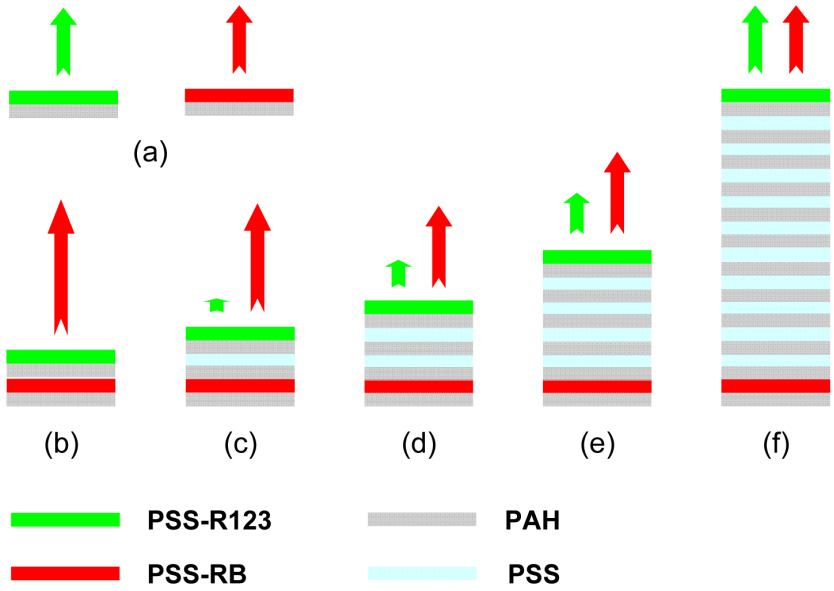

Figure 1.6. Schematics of the layers in LbL assemblies to control the FRET for tuning the emitting color: (a) [PAH/PSS-R123] and [PAH/PSS-RB]; (b)~(f) $[PAH/PSS\text{-}RB]/[PAH/PSS]_n/[PAH/PSS\text{-}R123]$, where n = 0, 1, 2, 4, and 8.

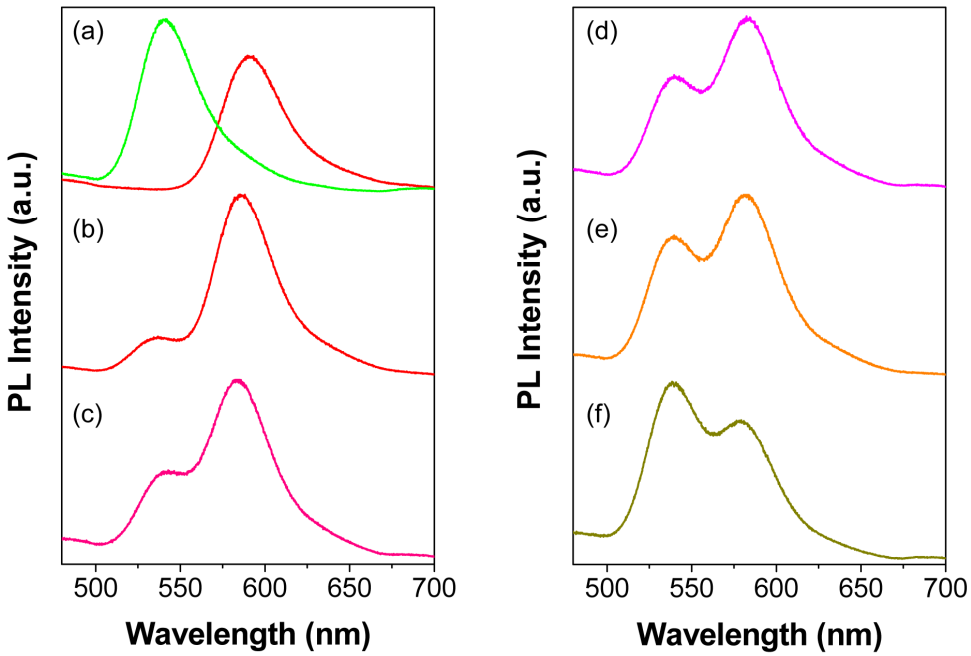

Figure 1.7. PL spectra of LbL assemblies with various numbers of [PAH/PSS] spacers between [PAH/PSS-R123] and [PAH/PSS-RB]: (a) [PAH/PSS-R123] and [PAH/PSS-RB]; (b)-(f) [PAH/PSS-RB]/ $<$[PAH/PSS]$>_n$/ [PAH/PSS-R123], where n = 0, 1, 2, 4, and 8. The layers in each LbL assembly are shown in the schematics in Figure 1.6. The excitation wavelength was 460 nm.

Chapter 2

Controlled Fluorescence Resonance Energy Transfer from Multiple Fluorophores in Layer-by-Layer Assemblies

2.1. Introduction

Recent developments in the nanofabrication techniques employing self-assembled materials enable the precise organization of functionalities within thin films of synthetic nanostructures such as block copolymers,[1,2] layer-by-layer (LbL) assemblies,[3-6] dendrimers,[7] zeolites,[8] anodized aluminum oxides,[9] and others.[10] A variety of functional materials have been incorporated into specific positions of the self-assembled structures utilizing specific chemical or physical interactions. In particular, LbL assemblies based on alternating electrostatic absorption between oppositely charged materials have been widely investigated to produce multilayered thin films with designed functionalities.[11-18] The LbL assembling The LbL assembling technique is a simple process because of its self-assembling nature. However, it also makes possible the use of versatile and universal protocols for the incorporation of various functionalities into the multilayered thin films with suitable selection and surface-modification of building materials. For examples, LbL assemblies with nanoparticles,[11,12,20] carbon nanotubes,[18,20] fluorescent dyes,[13,15–17] proteins,[14] and others have been successfully fabricated with designed physical and chemical properties. In addition, more than one type of functionality can be incorporated into different layers to produce multifunctional LbL assemblies. For examples, CdTe nanoparticles having unique photoluminescent properties have been assembled onto Fe_3O_4 magnetic nanoparticles using LbL assembly to produce magnetic luminescent composites.[19]

In particular, LbL assemblies have been employed as model structures

to investigate fluorescence resonance energy transfer (FRET) that involves non-radiative energy transfer from excited-state donors to ground-state acceptors.[13,21–27] A variety of donor/acceptor pairs of fluorescent dyes and semiconductor nanoparticles that are either multiply charged by themselves[13,21,22] or covalently attached to polyelectrolytes[23–27] have been incorporated into the layers of LbL assemblies to control the energy transfer process. Since FRET strongly depends on the donor-to-acceptor distance,[28,29] the emissions from the thin film can be tuned by adjusting the deposition sequence of neat polyelectrolytes and fluorophores. However, most of the previous studies have been focused on a single kind of FRET event with a donor/acceptor pair of fluorophores.[13,21–27] The application of FRET in photonics and optoelectronics, however, requires further controls over multiple FRET events.[30–33] In a light-emitting diode (LED), for example, the energy transfer from a single excitation source to multiple fluorophores is essential for the production of different colors.[31–35] At the same time, multicolor emissions from several fluorophores are required for color tuning, which necessitates restricted energy transfers among dissimilar fluorophores.[36,37]

Here, we demonstrate how to utilize LbL assemblies to create simultaneous emission of different fluorophores with enhanced intensities by a single excitation source. We designed LbL assemblies that not only allow FRET from light-absorbing fluorophores to light-emitting fluorophores but also restrict FRET between emitting fluorophores. For this purpose, three different kinds of fluorescent dyes with distinct emission wavelengths have

been selected and covalently attached to polyelectrolytes. LbL assemblies with fluorophore-labeled polyelectrolytes were fabricated by alternating deposition with neat polyelectrolytes. The emission intensities of the green-emitting and red-emitting fluorophores using a blue excitation source were considerably enhanced by introducing a layer of blue-absorbing fluorophores into the adjacent layer of emitting fluorophores. The blue excitation collected mostly on the absorbing fluorophores was efficiently conveyed to the emitting fluorophores. Furthermore, simultaneous green and red emission with enhanced intensities was produced by an LbL assembly with a planed sequence in which a layer of blue-absorbing fluorophores was incorporated into adjacent layers of green- and red-emitting fluorophores while the layers of emitting fluorophores were alienated beyond their Förster radius.

2.2. Experimental Section

Poly(allyamine hydrochloride) (PAH, Mw = 56000 g/mol), poly-(styrene sulfonate) (PSS, Mw = 70000 g/mol), 7-diethylamino- coumarin-3-carboxylic acid succinimidyl ester (Cou), fluorescein-5-isothiocyanate (Flu), rhodamine B isothiocyanate (Rho), and all other chemicals were purchased from Sigma-Aldrich and were used as received.

PAH was covalently labeled with Cou, Flu, and Rho (denoted by Cou-PAH, Flu-PAH, and Rho-PAH hereafter) as in the literature.[25–27] The molar ratio of dye to the repeat unit of PAH was adjusted by adding different

amounts of dye to the reaction solution and was estimated as 0.006 for Cou-PAH, 0.005 for Flu-PAH, and 0.002 for Rho-PAH, based on the extinction coefficient of each dye.[25,26]

To fabricate LbL assemblies, PAH, fluorophore-labeled PAH, and PSS were dissolved in deionized water to yield 0.01 M solutions. Silicon wafers and quartz plates were cleaned in a piranha solution (70/30 vol.-% of concentrated H_2SO_4 and 30 % H_2O_2) to create a negatively charged surface. LbL assemblies were fabricated by the alternating spin coating (3000 rpm for 30 s) of oppositely charged polyelectrolytes. Prior to the deposition of fluorophore-labeled PAH, three [PAH/PSS] bilayers were first spin-coated to produce uniform surface charges on the substrate. After the deposition of each layer, the LbL films were washed with deionized water.

UV-Vis spectra were obtained on a Sinco-3100 spectrophotometer. Photoluminescence (PL) was measured on an Acton Spectra Pro with a He-Cd laser (442 nm) as the excitation source. The thickness of the LbL thin films on silicon wafers was measured by ellipsometry (Gatner Scientific, L2W15S380) with a 632.8 nm He-Ne laser. Time-resolved fluorescence (TRF) was obtained using the time-correlated single-photon counting (TCSPC) technique. The excitation source is a self-mode-locked femtosecond Ti:sapphire laser (Coherent model Mira 900) pumped by an Nd:YVO_4 laser (Coherent Verdi diode-pumped laser). The laser output has a pulse width of 200 fs and can span excitation wavelengths in the range of 350–490 nm by second-harmonic generation. The excitation wavelength was 420 nm. All measurements were performed at room temperature.

2.3. Results and Discussion

To investigate multiple energy transfers within LbL assemblies, we first selected Cou, Flu, and Rho fluorescent dyes based on the spectral overlap between emission and absorption of these dyes for the good FRET efficiencies (Figure 2.1). Since multiple charges are required for the building materials in LbL thin films, each dye molecule was first covalently attached to the polyelectrolytes of PAH. Figure 2.2 shows the molecular structures of the polyelectrolytes of PAH and PSS, fluorophore-labeled PAH.

From the building materials in Figure 2.2, LbL assemblies with each fluorophore were prepared by depositing cationic PAH, cationic fluorophore-labeled PAH, and anionic PSS. Before spin coating the fluorophore-labeled PAH, three [PAH/PSS] bilayers were deposited to produce uniform surface charges on the substrate. The fluorophore-labeled PAH was subsequently spin-coated. Figure 2.3 shows the PL spectrum from the LbL assembly of $[PAH/PSS]_3$/Cou-PAH, $[PAH/PSS]_3$/Flu-PAH, and $[PAH/PSS]_3$/Rho-PAH with an excitation wavelength of 442 nm. The molar ratios of dye to monomer units of PAH were 0.006, 0.005, and 0.002 for Cou, Flu, and Rho, respectively. The amount of dye molecules in each layer can be adjusted by varying the molar ratio of dye to PAH during the labeling step. The PL intensity maxima of LbL films with Cou-PAH, Flu-PAH, and Rho-PAH were located at 480, 525, and 585 nm, respectively. The PL intensity from the thin film with Cou-PAH showed much stronger emission than those of Flu-PAH and Rho-PAH. This can be ascribed to the high absorption of Cou-PAH at the excitation wavelength of 442 nm (Figure 2.1). The quantum yield of each dye might also

affect the PL intensity, but the effect of the molar extinction coefficient could be more significant in this case. Fluorescein of Flu-PAH in the LbL film could be in a dianionic state when the UV-Vis and PL spectra (Figure 2.1) are compared with those in the literature.[38]

Since each fluorophore-labeled PAH can be incorporated into separate LbL films using electrostatic interaction with PSS, we can easily produce LbL assemblies with both donors and acceptors of fluorophores. For this purpose, we designed LbL assemblies with the schematics shown in Figure 3 that not only allow efficient FRET from light-harvesting fluorophores to light-emitting fluorophores but also restrict FRET between emitting fluorophores. In these schematics PAH and PSS are represented by dark gray and light gray lines, respectively. The Cou, Flu, and Rho fluorescent dyes are depicted as black, dark gray, and light gray spheres, respectively.

We first demonstrate effective collection and transportation of the excitation energy within the LbL assembly by depositing a donor/acceptor pair of fluorophore-labeled PAH into adjacent layers (Figure 2.4a and b). We utilized Cou-PAH and Flu-PAH as a donor/acceptor pair based on the spectral overlap between the emission of Cou-PAH and the absorption of Flu-PAH (see Figure 1). Then, LbL thin film of $[PAH/PSS]_3$/[Cou-PAH/PSS]/Flu-PAH was prepared (Figure 2.4a), the PL spectrum of which is shown in Figure 2.5a (gray solid). The molar ratios of Cou and Flu to PAH were 0.006 and 0.005, respectively. The PL spectra from the LbL assembly with only $[PAH/PSS]_3$/Cou-PAH (black dotted) and with only $[PAH/PSS]_3$/Flu-PAH (gray dotted) are also displayed. From the comparison, the emission of Flu at

525 nm was dramatically enhanced, whereas the emission of Cou at 480 nm was significantly quenched by the excitation of 442 nm. This indicates that the FRET from Cou-PAH to Flu-PAH was effectively preceded by placing both dyes in adjacent layers. The energy transfer process was further analyzed by TRF of Cou-PAH before and after deposition of Flu-PAH (Figure 2.5b). The monitoring wavelength was 480 nm. The solid lines are multiexponential fits to the TRF data. The TRF of Cou-PAH without Flu-PAH (black), i.e., $[PAH/PSS]_3$/Cou-PAH, showed a slow decay profile with an average lifetime of 2.92 ns. When the layer of Flu-PAH, i.e., $[PAH/PSS]_3$/[Cou-PAH/PSS]/Flu-PAH, was introduced, the fluorescence decay of Cou-PAH (gray) became faster with an average lifetime of 1.62 ns, which can be attributed to the fast quenching of the excited Cou-PAH by FRET.

The enhanced Flu-PAH emission by FRET can be explained by comparing the donor-to-acceptor distance with the Förster radius. Based on the Förster formalism[28,29] the Förster radius of Cou-PAH and Flu-PAH was estimated about 2.6 nm using the quantum yield of Cou-PAH(~ 0.013) in an aqueous solution. The donor-to-acceptor distance in the LbL assemblies was assumed to be the thickness of a PSS layer between the layers of Cou-PAH and Flu-PAH, which was measured as 1.9 nm by ellipsometry. Since the donor-to-acceptor distance is shorter than the Förster radius, the FRET from the Cou-PAH layer to the Flu-PAH layer occurred, leading to the enhanced Flu-PAH emission with quenched Cou-PAH emission from the thin films.

With the same method, we were able to enhance the emission of Rho by incorporating a Cou-PAH and Rho-PAH donor/acceptor pair into the

adjacent layers (Figure 2.4b). From the spectral overlap (Figure 2.1), Cou-PAH and Rho-PAH were selected as a donor and an acceptor, respectively. The LbL assembly of $[PAH/PSS]_3$/[Cou-PAH/PSS]/Rho-PAH was prepared as described in the previous case, and then PL spectrum was obtained with the same 442 nm excitation wavelength (Figure 2.6a). The PL spectra from LbL assemblies with only $[PAH/PSS]_3$/Cou-PAH (black dotted) and only $[PAH/PSS]_3$/Rho-PAH (gray dotted) were also inserted for comparison. The emission of Rho-PAH was greatly enhanced with quenched Cou-PAH emission at the excitation wavelength of 442 nm (Figure 2.6a). In addition, the TRF of Cou-PAH became faster with an average lifetime of 1.47 ns after the Rho-PAH deposition (Figure 2.6b), indicative of another donor/acceptor pair with efficient FRET. The enhanced Rho emission by Cou-PAH can be also explained by a shorter donor-to-acceptor distance (~ 1.9 nm) than the estimated Förster radius of Cou-PAH and Rho-PAH (2.5 nm).

To produce simultaneous emission of Flu-PAH and Rho-PAH with enhancement by Cou-PAH, a LbL assembly of $[PAH/PSS]_3$/[Cou-PAH/PSS]/[Flu-PAH/PSS]/$[PAH/PSS]_{10}$/[Cou-PAH/PSS]/Rho-PAH was prepared (Figure 2.4d). Here, we introduced a layer of light-absorbing Cou-PAH as the adjacent layer to the light-emitting Flu-PAH (and Rho-PAH). At the same time, the layer of Flu-PAH was separated from that of Rho-PAH by inserting ten bilayers of neat [PAH/PSS] between them. Flu-PAH and Rho-PAH work as a donor/acceptor pair because of their spectral overlap (Figure 2.1). Additionally, the energy transfer from Flu-PAH to Rho-PAH in the LbL assemblies can be completely restricted by inserting a number of [PAH/PSS]

bilayers between them (Figure 2.4c). This can alienate the donor-to-acceptor distance beyond the Förster radius of the pair, which will be demonstrated again later.

By excitation at 442 nm, the LbL assembly showed predominant emission from both Flu-PAH and Rho-PAH, shown in the PL spectrum (black solid) of Figure 2.7. For comparison, the PL spectrum from the LbL assembly having the same sequence but without the layer of Cou-PAH, i.e., $[PAH/PSS]_3$/[Flu-PAH/PSS]/$[PAH/PSS]_{10}$/Rho-PAH, is also inserted (black dotted). In the PL spectrum, light emission from both Flu-PAH and Rho-PAH was greatly enhanced by introducing a layer of Cou-PAH, indicating efficient FRET from Cou-PAH to Flu-PAH and Rho-PAH. The simultaneous emission of Flu-PAH and Rho-PAH (black solid) in Figure 2.7 is a combination of the two enhanced emissions of Flu-PAH in $[PAH/PSS]_3$/[Cou-PAH/PSS]/Flu-PAH (Figure 2.5a) and Rho-PAH in $[PAH/PSS]_3$/[Cou-PAH/PSS]/Rho-PAH (Figure 2.6a). This indicates energy transfer from Flu-PAH to Rho-PAH was effectively prohibited by introducing neat [PAH/PSS] bilayers.

The multiple FRET events were further analyzed by the TRF of donors in the absence and presence of acceptors. In Figure 2.8a, the decay profile of Cou-PAH at 480 nm in the thin films of $[PAH/PSS]_3$/[Cou-PAH/PSS/Flu-PAH/PSS]/$[PAH/PSS]_{10}$/[Cou-PAH/PSS]/Rho-PAH (gray) showed faster decay, with an average lifetime of 1.45 ns compared to that in $[PAH/PSS]_3$/Cou-PAH (black). This indicated that the energy transfers from Cou-PAH to both Flu-PAH and Rho-PAH occurred in the LbL assembly as in the previous case. On the other hand, the TRF of Flu-PAH monitored at 525

nm as shown in Figure 2.8b was not altered by the presence of Rho-PAH in a separate layer, indicating complete restriction of FRET between Flu-PAH and Rho-PAH. Therefore, the LbL assembly not only provided the efficient energy transfer from Cou-PAH light-harvesting donors to Flu-PAH and Rho-PAH light-emitting acceptors, but also the restricted energy transfer between the two emitting fluorophores of Flu-PAH and Rho-PAH by inserting [PAH/PSS] bilayers as a FRET barrier.

The controlled multiple energy transfers in the LbL assembly can be explained by the comparison of donor-to acceptor distances and Förster radii. As in the previous case, the donor-to-acceptor distance of a pair of Cou-PAH and Flu-PAH (or a pair of Cou-PAH and Rho-PAH) is shorter than each Förster radius when they were deposited into adjacent layers, allowing efficient energy transfers for the enhanced emissions. With respect to another donor/acceptor pair of Flu-PAH and Rho-PAH, on the other hands, they were separated by ten bilayers of [PAH/PSS]. From the ellipsometry measurements, the distance between the layers of Flu-PAH and the layer of Rho-PAH, i.e., the thickness of $[PAH/PSS]_{10}$ was 26 nm, which was much larger than their 5.1 nm Förster radius. Therefore, the energy transfer between Flu-PAH and Rho-PAH was prohibited to produce simultaneous emission.

2.4. Conclusion

We have demonstrated how multiple energy transfer processes can be precisely controlled within LbL assemblies. Since fluorophore-labeled PAH was inserted into designed layers of LbL thin films, LbL assemblies with multiple fluorescent dyes were prepared to control multiple FRET events. In particular, LbL assemblies showing enhanced intensity of simultaneous emission from Flu-PAH and Rho-PAH were fabricated by placing a layer of light-absorbing Cou-PAH into adjacent layers of both light-emitting Flu-PAH and Rho-PAH but separating each Flu-PAH and Rho-PAH layer beyond the Förster radius. The designed LbL assembly not only allowed FRET but also prohibited FRET when neat bilayers of [PAH/PSS] were utilized as FRET barriers. The method presented here can find applications where multiple controls of FRET events are necessary, for example, to produce white emission from a single excitation source.

2.5. References

[1] S. I. Yoo, S. H. Bae, K. S. Kim, B. H. Sohn, *Soft Matter* **2009**, *5*, 2990.

[2] M. R. Bockstaller, R. A. Mickiewicz, E. L. Thomas, *Adv. Mater*. **2005**, 17, 1331.

[3] Y. Wang, A. S. Angelatos, F. Caruso, *Chem. Mater*. **2008**, *20*, 848.

[4] K. Ariga, J. P. Hill, Q. Ji, Phys. *Chem. Chem. Phys.* **2007**, *9*, 2319.

[5] P. T. Hammond, *Adv. Mater*. **2004**, *16*, 1271.

[6] G. Decher, *Science* **1997**, *277*, 1232.

[7] A. Adronov, J. M. J. Fréchet, *Chem. Commun*. **2000**, 1701.

[8] D. Brühwiler, G. Calzaferri, T. Torres, J. H. Ramm, N. Gartmann, L.-Q. Dieu, I. López Duarte, M. V. Martínez-Díaz, *J. Mater. Chem*. **2009**, *19*, 8040.

[9] M. Steinhart, R. B. Wehrspohn, U. Go¨sele, J. H. Wendorff, *Angew. Chem., Int. Ed.* **2004**, *43*, 1334.

[10] L. D. Carlos, R. A. S. Ferreira, V. de Z. Bermudez, S. J. L. Ribeiro, *Adv. Mater*. **2009**, *21*, 509.

[11] J.-S. Lee, J. Cho, C. Lee, I. Kim, J. Park, Y.-M. Kim, H. Shin, J. Lee, F. Caruso, *Nat. Nanotechnol*. **2007**, *2*, 790.

[12] Z. Wu, D. Lee, M. F. Rubner, R. E. Cohen, *Small* **2007**, *3*, 1445.

[13] Q. Zhang, T. Atay, J. R. Tischler, M. S. Bradley, V. Bulović, A. V. Nurmikko, *Nat. Nanotechnol.* **2007**, *2*, 555.

[14] J. F. Quinn, A. P. R. Johnston, G. K. Such, A. N. Zelikin, F. Caruso, *Chem. Soc. Rev*. **2007**, *36*, 707.

[15] T. Tang, J. Qu, K. Müllen, S. E. Webber, *Langmuir* **2006**, *22*, 26.

[16] H. Chen, G. Zeng, Z. Wang, X. Zhang, M.-L. Peng, L.-Z. Wu, C.-H. Tung, *Chem. Mater*. **2005**, *17*, 6679.

[17] N. Ma, H. Zhang, B. Song, Z. Wang, X. Zhang, *Chem. Mater*. **2005**, *17*, 5065.

[18] M. A. Correa-Duarte, J. Pérez-Juste, A. Sánchez-Iglesias, M. Giersig, L. M. Liz-Marzán, *Angew. Chem. Int. Ed.* **2005**, *44*, 4375.

[19] X. Hong, J. Li, M. Wang, J. Xu, W. Guo, J. Li, Y. Bai, T. Li, *Chem. Mater.* **2004**, *16*, 4022.

[20] A. A. Mamedov, N. A. Kotov, M. Prato, D. M. Guldi, J. P. Wicksted, A. Hirsch, *Nat. Mater*. **2002**, *1*, 190.

[21] T. Tang, J. Qu, K. Mu¨llen, S. E. Webber, *Langmuir* **2006**, *22*, 7610.

[22] T. A. Klar, T. Franzl, A. L. Rogach, J. Feldmann, *Adv. Mater*. **2005**, *17*, 769.

[23] J. F. Baussard, J. L. Habib-Jiwan, A. Laschewsky, *Langmuir* **2003**, *19*, 7963.

[24] G. M. Lowman, N. Daoud, R. M. Case, P. J. Carson, S. K. Buratto, *Nano Lett*. **2001**, *1*, 677.

[25] B. Richter, S. Kirstein, *Chem. Phys*. **1999**, *111*, 5191.

[26] D. M. Kaschak, J. T. Lean, C. C. Waraksa, G. B. Saupe, H. Usami, T. E. Mallouk, *J. Am. Chem. Soc*. **1999**, *121*, 3435.

[27] D. M. Kaschak, T. E. Mallouk, *J. Am. Chem. Soc.* **1996**, *118*, 4222.

[28] B. Valeur, *Molecular Fluorescence: Principles and Applications*, Wiley-VCH, Weinheim **2002**.

[29] J. R. Lakowicz, *Principles of Fluorescence Spectroscopy*, Platinum, New York **1983**.

[30] B. E. Hardin, E. T. Hoke, P. B. Armstrong, J. H. Yum, P. Comte, T. Torres, J. M. J. Fréchet, M. K. Nazeeruddin, M. Grätzel, M. D. McGehee, *Nat. Photonics* **2009**, *3*, 406.

[31] A. L. Rogach, N. Gaponik, J. M. Lupton, C. Bertoni, D. E. Gallardo, S. Dunn, N. L. Pira, M. Paderi, P. Repetto, S. G. Romanov, C. O'Dwyer, C. M. S. Torres, A. Eychmüller, *Angew. Chem.Int. Ed.* **2008**, *47*, 6538.

[32] M. Achermann, M. A. Petruska, D. D. Koleske, M. H. Crawford, V. I. Klimov, *Nano Lett*. **2006**, *6*, 1396.

[33] M. Achermann, M. A. Petruska, S. Kos, D. L. Smith, D. D. Koleske, V. I. Klimov, *Nature* **2004**, *429*, 642.

[34] X.-G. Li, Y.-W. Liu, M.-R. Huang, S. Peng, L.-Z. Gong, M. G. Moloney, *Chem. Eur. J*. **2010**, *16*, 4803.

[35] X.-G. Li, H. Li, M.-R. Huang, *Chem. Eur. J*. **2007**, *13*, 8884.

[36] B. W. D'Andrade, S. R. Forrest, *Adv. Mater*. **2004**, *16*, 1585.

[37] J. H. Park, J. Y. Kim, B. D. Chin, Y. C. Kim, J. J. Kim, O. O. Park, *Nanotechnology* **2004**, *15*, 1217.

[38] M. M. Martion, L. Lindqvist, *J. Lumin*. **1975**, *10*, 381.

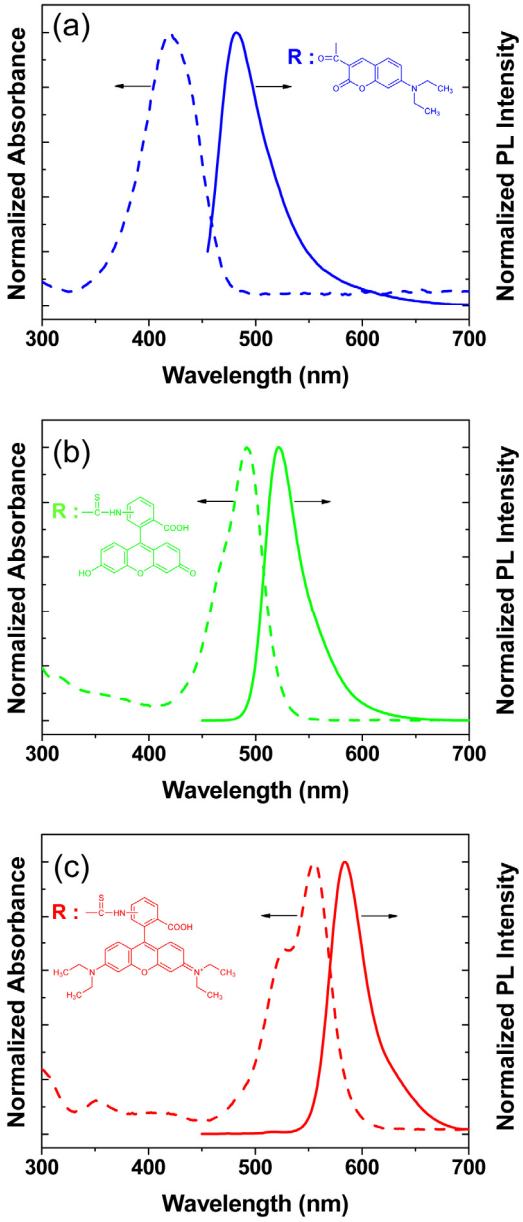

Figure 2.1. Normalized UV-Vis absorption (dotted line) and PL spectra (solid line) of Dye-PAH in water: (a) Cou-PAH; (b) Flu-PAH; (c) Rho-PAH. The concentration was 1.0×10^{-4} M in all cases. The excitation wavelength was 442 nm. Chemical structures of dyes are also inserted.

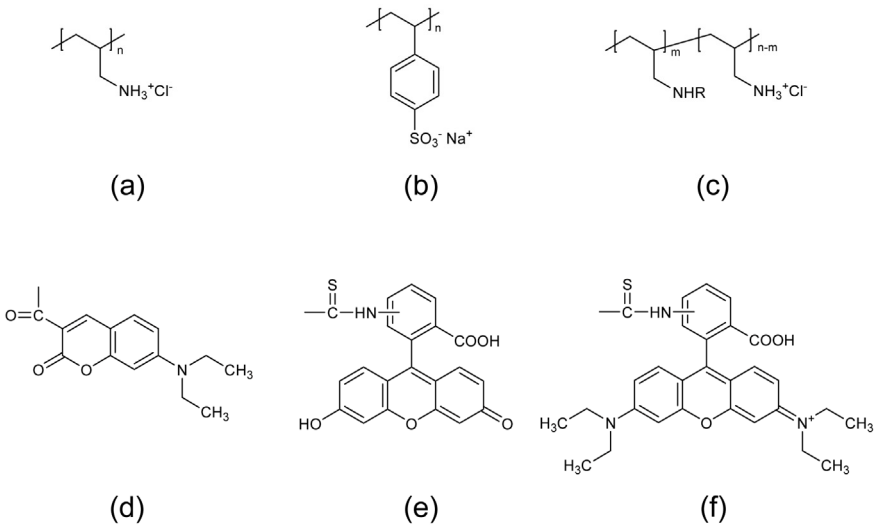

Figure 2.2. Molecular structures of polyelectrolytes and fluorescent dyes: (a) poly(allylamine hydrochloride) (PAH); (b) poly(stryrene sulfonate) (PSS); (c) PAH labeled with R; (d) R = Cou; (e) R = Flu; (f) R = Rho.

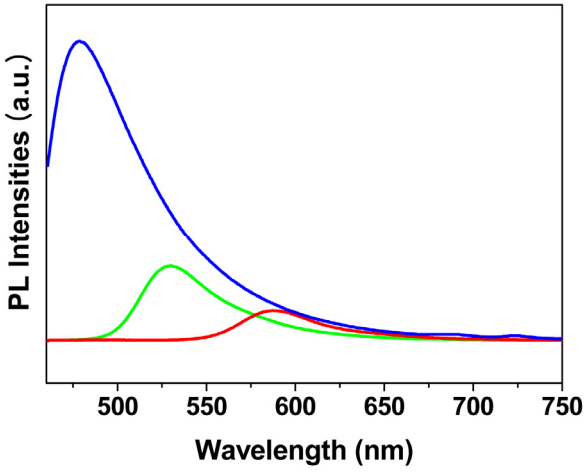

Figure 2.3. PL spectra from LbL assemblies of $[PAH/PSS]_3$/Cou-PAH (blue), $[PAH/PSS]_3$/Flu-PAH (green), and $[PAH/PSS]_3$/Rho-PAH (red). The excitation wavelength was 442 nm.

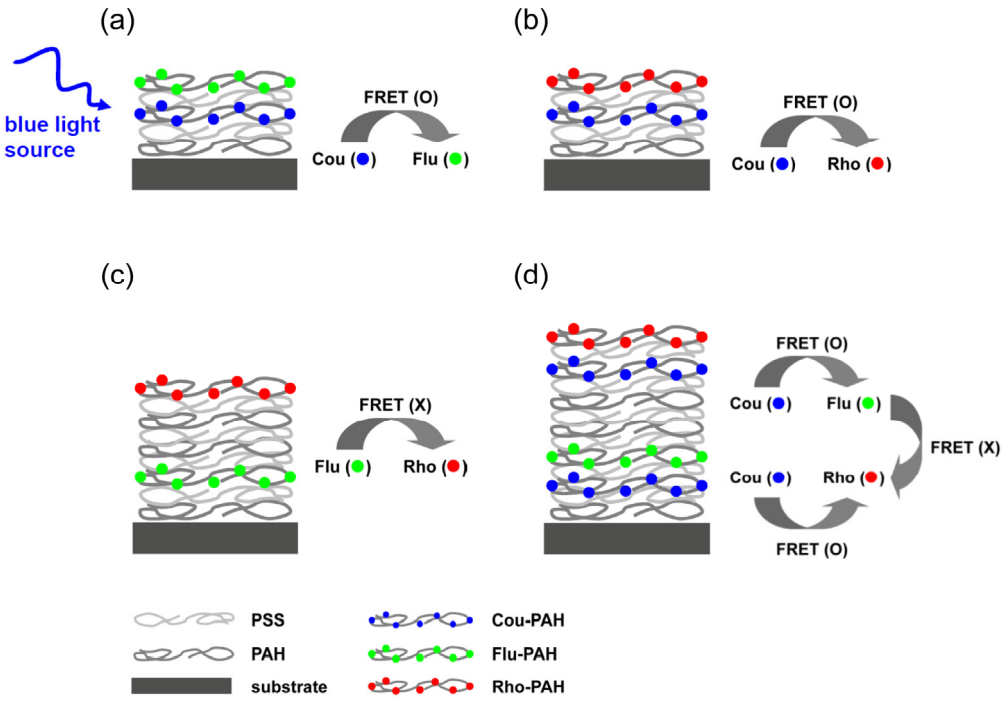

Figure 2.4. Schematics of LbL assemblies with different fluorophores: (a, b) allowed FRET; (c) restricted FRET; (d) combination of allowed and restricted FRET.

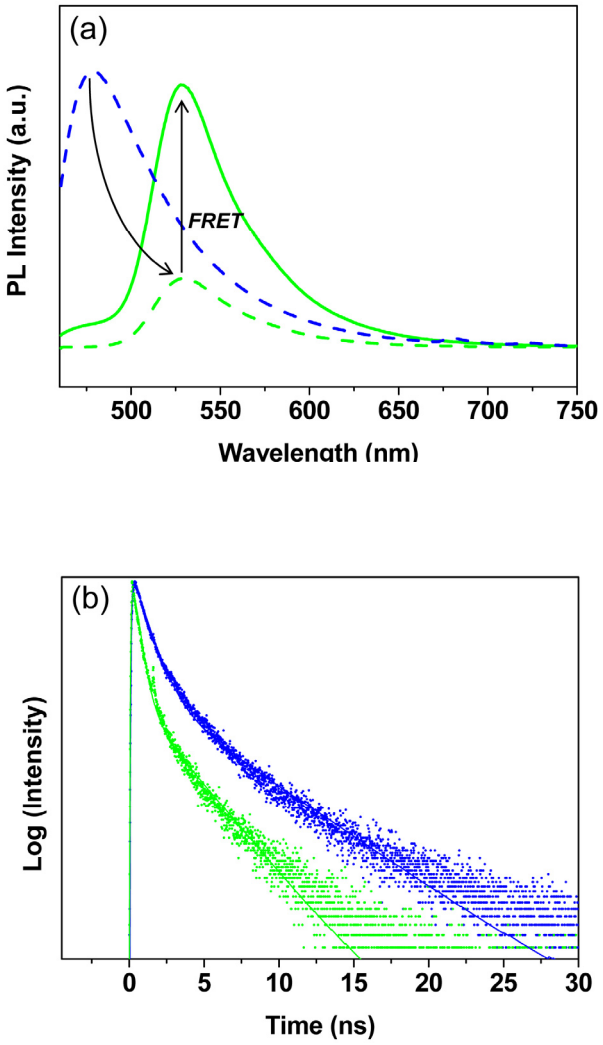

Figure 2.5. PL spectra from LbL assemblies of $[PAH/PSS]_3$/[Cou-PAH/PSS]/Flu-PAH: (a) enhanced emission of Flu-PAH by Cou-PAH; (b) TRF of Cou-PAH at 480 nm before (blue) and after (green) deposition of Flu-PAH.

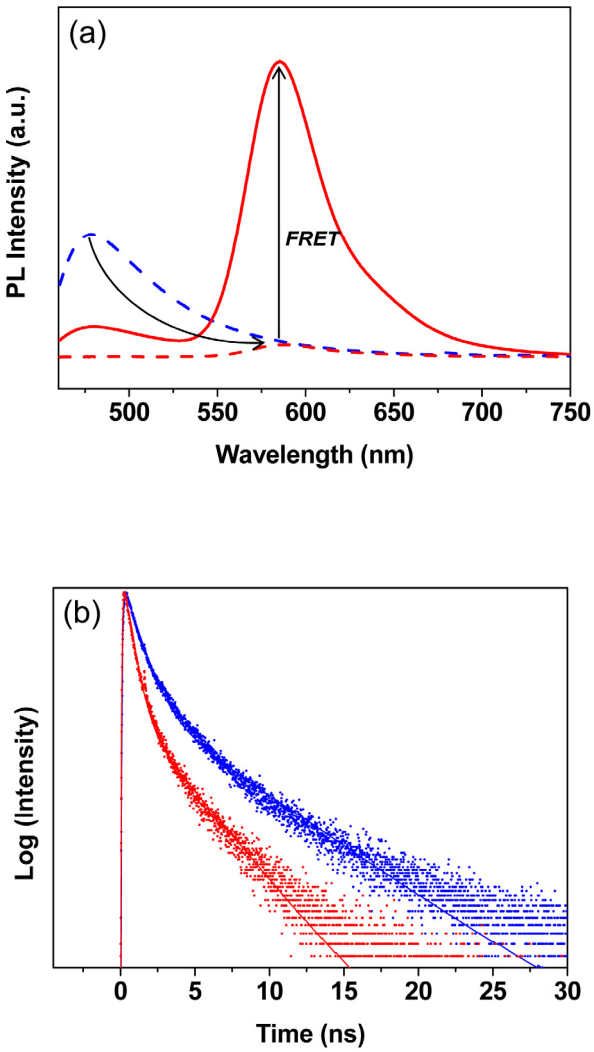

Figure 2.6. PL spectra from LbL assemblies of $[PAH/PSS]_3$/[Cou-PAH/PSS]/Rho-PAH: (a) enhanced emission of Flu-PAH by Cou-PAH; (b) TRF of Cou-PAH at 480 nm before (blue) and after (red) deposition of Rho-PAH.

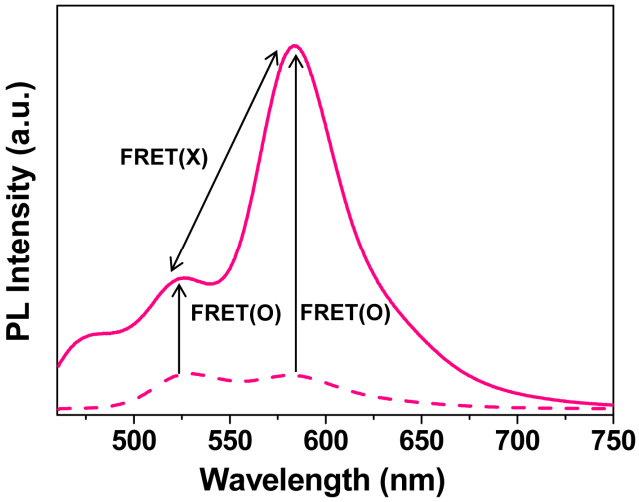

Figure 2.7. PL spectra from LbL assembly of $[PAH/PSS]_3$/[Cou-PAH/PSS/Flu-PAH/PSS]/$[PAH/PSS]_{10}$/[Cou-PAH/PSS]/Rho-PAH (solid) and $[PAH/PSS]_3$/[Flu-PAH/PSS]/ $[PAH/PSS]_{10}$/Rho-PAH (dotted).

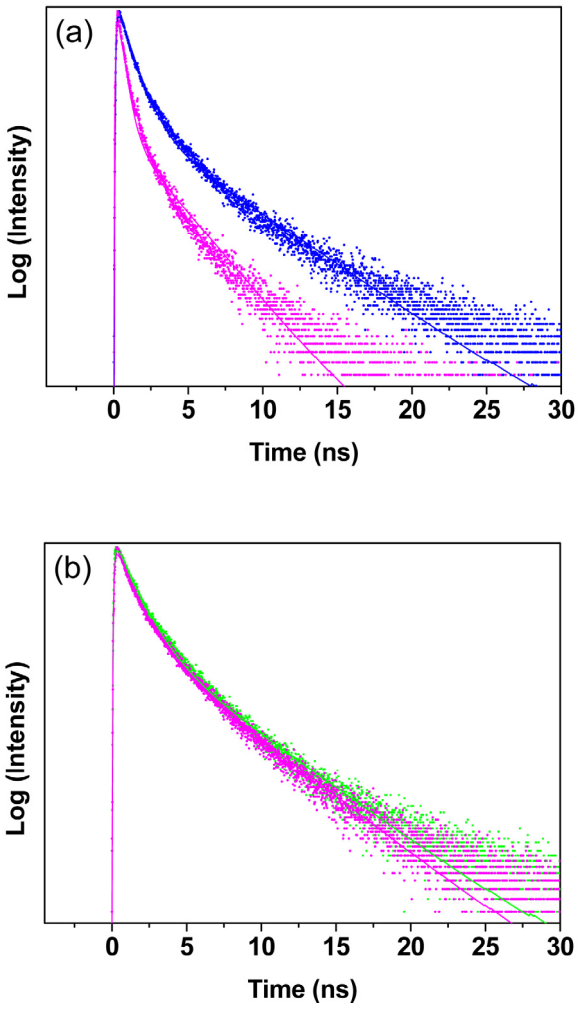

Figure 2.8. TRF spectra of LbL assemblies with Cou-PAH, Flu-PAH and Rho-PAH: (a) Cou-PAH at 480 nm from $[PAH/PSS]_3$/Cou-PAH (blue) and $[PAH/PSS]_3$/[Cou-PAH/PSS/Flu-PAH/PSS]/$[PAH/PSS]_{10}$/[Cou-PAH/PSS]/ Rho- PAH (pink); (b) Flu-PAH at 525 nm from $[PAH/PSS]_3$/[Cou-PAH/PSS]/ Flu-PAH (green) and $[PAH/PSS]_3$/[Cou-PAH/PSS/Flu-PAH/PSS]/ $[PAH/PSS]_{10}$/[Cou-PAH/PSS]/Rho-PAH (pink).

Chapter 3

Correlation of Micellar Structures with Surface-Plasmon-Coupled Fluorescence in Strategy for Fluorescence Enhancement

3.1. Introduction

Light incident on metal nanoparticles (NPs) induces a collective Light incident on metal nanoparticles (NPs) induces a collective oscillation of the conduction electrons in metal NPs, which can produce strong electromagnetic fields in the proximity of the NP surfaces. This unique property of metal NPs, known as localized surface plasmon resonance, gives rise to a new understanding of light-matter interactions that can be manipulated in the nanometer size region.[1-7] In this scope, metal NPs serve as either antennas to enhance local electric fields around the NPs or waveguides to control the propagation of light in a specific direction.[1,2,4] The consequences of this understanding now opens widespread possibilities in optoelectronics,[4,5,8] cell-imaging,[3,9] diagnostics,[6,10] and biology.[7,11] For example, metal NPs can be implemented into light-emitting diodes to increase the quantum efficiency of the emitting materials.[4,8] If fluorophore-labeled DNA strands or proteins are bound to metal NPs, the spectral characteristics of fluorophores can be modified in terms of intensity or wavelength to allow sensitive detection of biological reactions.[1,7,10,11] Also, the light-harvesting function of photosynthetic proteins has been found to be enhanced by metal NPs.[11b,c] These stimuli from different research areas are in large part originated from the strong near-field interactions between metal NPs and fluorophores. When fluorophores, such as quantum dots, fluorescent proteins, or dyes, are placed in the vicinity of metal NPs, their intrinsic excitation rates and radiative/non-radiative decay rates can be altered to exhibit abnormal response in fluorescence signal such as enhanced or quenched emission.[1,4,6,11]

Now, the question arose from NP effects is how to or what kind of assembling methods can be applied to engineer NP-fluorophore interactions. Recent studies have revealed that these interactions are strongly correlated with (a) the extinction characteristics of metal NPs,[3,6,12] (b) the spectral properties of fluorophores,[11d,13] and (c) the distance between metal NPs and fluorophores.[10a,11,14] In other words, those experimental parameters are the problems that one has to solve for the practical prospects of plasmonic effects. Problems (a) and (b) might be readily solved if one can rely on available synthetic methods. For example, the extinction spectrum of a given metal NPs, that is a sum of absorption and scattering spectra, can be tuned by the composition, size, and shape of NPs.[1,3,15] Citrate reduction of $HAuCl_4$ can produce spherical Au NPs having ~ 10 nm in a diameter. Since Au NPs with this diameter possess a strong absorption component in their extinction spectrum, they potentially quench the fluorescence of nearby fluorophores.[10a,13a,14b] On the other hands, seed-mediated growth of Au and Ag NPs can produce larger and faceted NP structures with a superior scattering factor, which tends to enhance the fluorescence.[1,3,12,13c] As for the problem (b), the spectral properties of fluorophores, one may use different types of fluorescent dyes to label proteins or DNA.[6,10a,13a,b] If quantum dots are to be used, their absorption and emission spectra can be tuned by quantum confinement.[12a,c,16a] Therefore, the main problem associated with NP-fluorophore interaction is how to control the spatial arrangement of metal NPs and fluorophores.

To solve this problem, self-assembling techniques such as layer-by-

layer assemblies,[14a,b,d] multilayered core-shell particles,[16] and bio-conjugates[10a,11,13] have been utilized. These studies then reached several lines of consistent observations; (1) if fluorophores are closely placed to the surface of metal NPs (< 5 nm), fluorescence is quenched by non-radiative energy transfer to metal NPs, (2) no specific NP-fluorophore interaction is expected for larger separation (> 30 nm) because the local fields around metal NPs rapidly decrease with distance, and (3) fluorescence can be enhanced in the region 5 ~ 30 nm from the surface of the NPs if the scattering component of the given NPs is higher than the absorption component in the extinction spectrum.[1,4,6,11,14] However, these pre-engaged assembling methods have some inherent drawbacks in practical and fundamental aspects because they either require multiple rounds of assembling steps to reach dimensions of tens of nanometers or entail significant loss of materials by centrifuge-based purification.[14a,b] If NP-fluorophore complexes were assembled in a solution state, conformational changes of conjugating molecules such as polymers or proteins could cause significant deviations in the NP-fluorophore distance.[10a,11d]

These limitations implicate the potential usefulness of other assembling methods of a different nature and in this sense we envisioned that diblock copolymers can take advantages of their self-segregating properties. In a selective solvent, for example, diblock copolymers self-associate into spherical micelles consisting of soluble coronas and insoluble cores.[17] The cores of the micelles can be further functionalized by fluorophores, such as fluorescent dyes[18a,b,c] and quantum dots.[18d] This assembling method is

parallel, produces size-tunable nanodomains in a range of ~ 10 nm to ~ 100 nm depending on the molecular weight of the polymers, and can be applied to a thin film state with a fixed physical dimension.[17,18] These features of copolymer micelles have a direct relevance to the solution of the problem, however, no research has been performed in this perspective. Here, we will deal with those issues addressed so far by block copolymer micelles to make a certain emphasis on the strategy for the fluorescence enhancement as a proof-of-concept.

3.2. Experimental Section

Polystyrene-poly(4-vinylpyridine) (PS-PVP) was purchased from Polymer Source, Inc. The molecular weight of PS and PVP blocks were 25,000 g/mol and 7,000 g/mol, respectively, with a polydispersity index (PDI) of 1.10. Rhodamine 123 (R123) and sulforhodamine 101 (S101) were purchased from Sigma-Aldrich and were used as received. PS-PVP copolymers were dissolved in toluene (0.5 wt%), stirred at 70 °C for 3 h, and then cooled to room temperature. To incorporate R123 and S101 into the PVP core of the micelles, each dye was added to a toluene solution ([dye]/[VP] = 0.005) with vigorous stirring (~ 7 days).

Ag NPs were synthesized according to the literature with a slight modification.[19] Briefly, 100 ml aqueous solution of 1.0 mM silver nitrate was heated to reflux and 0.5 ml of 0.3 M solution of sodium citrate was added

immediately with vigorous stirring. The resulting solution was kept boiling for 30 min and then cooled down to room temperature. A quartz or Si-wafer substrate was cleaned by piranha solution (70/30 v/v of concentrated H_2SO_4 and 30 % H_2O_2) to create negative charges on the surface.[23] Then, aqueous solutions (0.01 M) of positively-charged poly(allylamine hydrochloride) (PAH, Mw = 56,000 g/mol) and negatively-charged poly(styrene 4-sulfonate) (PSS, Mw = 70,000 g/mol) were alternatively spin-coated (3000 rpm for 30 sec) on the piranha-cleaned substrate to produce a multi-layered film consisting of three bi-layers of [PAH/PSS] and a top layer of PAH (this structure was denoted as $[PAH/PSS]_3$/PAH in the main text). During the deposition step for each PAH or PSS layer, the film was rinsed twice with deionized water by spin coating. The chemically modified substrate was immersed in the solution of Ag NPs for 3 h to deposit Ag NPs on the substrate.

UV-Vis spectra were recorded on a Varian Cary-5000 spectrophotometer. Steady-state fluorescence was measured on an Acton SpectraPro with a He-Cd laser (442 nm) as the excitation source. Time-resolved fluorescence (TRF) was measured using a Streak Camera system (Hamamatsu C4742). Samples were excited with the frequency-doubled output of a Ti:Sapphire amplifier system (LIBRA-HE, Coherent) at a repetition rate of 1 kHz and a pulse width of 100 fs. The excitation wavelength was 400 nm. All measurements were performed at room temperature. Transmission electron microscopy (TEM) was carried out on a Hitachi 7600 operating at 100 kV. For TEM, a micellar film was coated on a mica substrate and then floated off from the substrate onto deionized water

and collected on a carbon-coated grid. For the contrast in the TEM, PVP blocks were selectively stained by I_2 vapor. Surface morphologies were investigated by field-emission scanning electron microscopy (FE-SEM, JSM-6700F JEOL) and atomic force microscopy (AFM, Nanoscope IIIA, Digital Instrument) in tapping mode with Si cantilevers.

3.3. Results and Discussion

Polystyrene-poly(4-vinyl pyridine), PS-PVP, diblock copolymers self-associate into spherical micelles consisting of a soluble PS corona and an insoluble PVP core in toluene that is a selective solvent for the PS block.[17,18] We selected PS-PVP copolymers with PS and PVP blocks having molecular weights of 25000 g/mol and 7000 g/mol, respectively, and with a polydispersity index (PDI) of 1.10 (Polymer Source Inc). This selection was based on the aggregation behavior of PS-PVP in toluene and aimed to produce a specific physical dimension of micelles for an effective NP-fluorophore interaction, which will be discussed throughout this study. After PS-PVP micelles were produced in toluene (0.5 wt%), they were spin-coated onto solid substrates to form a single-layered film of micelles. As the TEM image of Figure 3.1a, spherical PS-PVP micelles are arranged in a hexagonal order with a dark PVP core and a bright PS matrix without multi-layered structures. The average diameter of the PVP cores and the center-to-center distance between micelles were estimated as ~ 14 nm and ~ 34 nm, respectively.

For a NP-fluorophore pair, negatively charged Ag NPs were synthesized by reducing silver nitrate with sodium citrate in an aqueous solution.[16c,19] Ag NPs from this method have been extensively studied in the past and were proved to have a strong scattering property.[19] Most of the synthesized NPs have a spherical shape with a diameter of ~ 58 nm ± 12 nm but some faceted structures were also found in the transmission electron microscopy (TEM) images (Figure 3.1b). To place Ag NPs on solid substrates, poly(allyamine hydrochloride) (PAH) and poly(styrene 4-sulfonate) (PSS) were alternatively coated onto quartz or Si-wafers to prepare a thin film of $[PAH/PSS]_3$/PAH, at which positively charged PAH was placed on top of the multilayered film (see Experimental section). This process was introduced to facilitate the deposition of Ag NPs onto quartz by electrostatic interaction between negatively charged Ag NPs and positively charged PAH. The chemically modified quartz substrates were then immersed into an aqueous solution of Ag NPs for 3 h. In Figure 3.1c, Ag NPs are homogeneously dispersed on the substrates without noticeable particle agglomeration and the surface coverage of the substrate by NPs was estimated as ~ 25 %. The extinction spectrum of Ag NPs on the quartz showed a plasmon resonance at around 400 nm (Figure 3.2) and its intensity was not varied at different preparation times indicating a reproducible amount of NPs on the substrates. The extinction spectra of Ag NPs vary in a solution and thin film state. For instance, the extinction spectrum of Ag NPs in an aqueous solution has a maximum around 430 nm (Figure 3.2a), while that of the same Ag NPs coated on the quartz substrate was blue-shifted to ~ 400 nm (Figure 3.2b). This

behavior can be understood by the decrease in the refractive index (n) of the surroundings (n = 1.33 for water and n = 1.0 for air). In order to confirm the uniform deposition of Ag NPs, we measured the extinction intensity of Ag NPs on the quartz substrates and it was nearly identical at each preparation time. In addition, after coating PS-PVP micelles on the NP substrate, the peak position was further shifted to ~ 454 nm (Figure 3.2c) because of the higher refractive index of PS coronas (n = 1.59).

As counterparts to the Ag NPs, commercially available dyes of rhodamine 123 (R123) and sulforhodamine 101 (S101) were selected because these dye molecules have strong hydrophilic characters without any solubility in toluene. While both R123 and S101 dyes were not soluble and remained powdery in toluene without micelles (for longer than several months), a homogenous solution was formed after adding dye molecules to the micellar solution with vigorous stirring (~ 7 days) by the selective inclusion of the dyes into the hydrophilic PVP cores ([dye]/[PVP] = 0.005).[18a,b] Then, PS-PVP micelles containing R123 or S101 in the cores were spin-coated on the NP-deposited quartz substrate (denoted as a NP substrate hereafter). In the atomic force microscopy (AFM) image (Figure 3.1d), small-sized PS-PVP micelles now cover NP-uncoated areas on the substrates without structural changes and also found to be attached to the surface of Ag NPs by XPS analysis. (Figure 3.3)

To verify whether the surface of Ag NPs was coated by PS-PVP micelles, XPS spectra of Ag (3d) photoelectron peak were compared before (black line) and after (red line) being coating by PS-PVP micelles (Figure 3.3).

While the clear decrease in the intensity of Ag peak strongly indicates that the NP surface was covered by PS-PVP micelles, the resident Ag peak implies that the NP surface was not fully coated by the micelles. Since the formation of a micellar film can be driven by the lateral assembly of micelles, i.e., by a lateral capillary force, the presence of the curved NP surface may interrupt the capillary action to prevent the full coverage of the NP surface.

With the micellar system, near-field interactions between Ag NPs and dye molecules were studied by several spectroscopy techniques. In the first set of experiments, PS-PVP micelles containing R123 in the core were spin-coated on the NP substrate and also on a bare substrate without NPs. Then, steady-state fluorescence spectra from the micelles with R123 were collected in the absence (gray dashed line) and presence (green solid line) of Ag NPs with an excitation wavelength of 442 nm (Figure 3.4a). Noticeably, the fluorescence intensity of R123 in the PVP core at 540 nm was significantly enhanced by 10 times when coated on the NP substrate. Even though the presence of NPs increases the surface area of the substrate by a certain degree, such a huge enhancement in the fluorescence cannot be attributed to the increased amount of micelles. Hence, this observation is a strong verification that dye molecules are substantially coupled with the surface plasmon of Ag NPs.

To closer examine the NP-fluorophore interactions, the photoluminescence dynamics of R123 over the entire range of its emission was recorded using a Streak Camera setup.[20,21] In the Streak-Camera plots (time-wavelength plots) shown in Figure 3.4b and 3.4c, the yellow and red

colors reflect higher photoluminescence intensity than the blue color. Since the signal intensity obtained from streak camera images is proportional to the fluorescence intensity of dyes, it can be concluded that the fluorescence decay of R123 on the NP substrate (Figure 3.4c) became much faster than that on the bare substrate (Figure 3.4b). However, the intensities in Figure 3.4b and 3.4c do not necessarily reflect the total amount of photons that arrived at the camera because the photons were only collected up to 10.0 ns. For a more quantitative comparison, the time-resolved fluorescence (TRF) dynamics at a monitoring wavelength of 540 nm (denoted as a dashed line) were extracted from the streak camera images. In Figure 3.4g, green circles represent the decay curve of R123 on the NP substrate, while gray circles represent the decay on the bare substrate. By fitting the TRF spectra with a multi-exponential decay, the average lifetimes of R123 in the absence and presence of NPs could be calculated to 1.84 ns and 0.71 ns, respectively (see Table 1 for details).

To get some physical insights into the above observations, a brief discussion on the general aspects of fluorescence may be useful. In the absence of metal NPs, the fluorescence dynamics are determined by a competition between the intrinsic radiative decay rate (k_{rad}^0) and the non-radiative decay rate (k_{nr}^0) of fluorophores and thus the quantum yield (Q^0) and lifetime (τ^0) can be expressed as $Q^0 = k_{rad}^0/(k_{rad}^0+ k_{nr}^0)$ and $\tau^0 = 1/(k_{rad}^0+ k_{nr}^0)$.[1,6, 21] On the other hand, fluorophores in the vicinity of metal NPs can undergo excitation enhancement (increased light absorption), emission enhancement (increased radiative decay rate), or quenching (increased non-

radiative decay rate) altering their intrinsic properties.[1,4,6,11-14] In this context, the shortened lifetime of R123 illustrated by the faster decay observed in the TRF spectrum (Figure 3.4g) indicates that either k_{rad}^0 or k_{nr}^0 was increased by the Ag NPs. However, an increase in k_{nr}^0 is not reasonable, because we clearly observed a fluorescence enhancement. Therefore, the main observations shown in Figure 3.4(a, b, c, g) and the impact of the NPs can only be a substantial increase in k_{rad}^0 that raises the quantum yield of the dyes. However, we do not entirely rule out the possibility of a minor alternation in k_{nr}^0.

In another set of experiments, PS-PVP micelles containing S101 in the core were applied to the NP substrate and their fluorescence properties were compared to the same micelles on a bare substrate. As demonstrated in Figure 3.4(d, e, f, h), qualitatively similar results as for R123 were obtained; the steady-state fluorescence peaking at 600 nm showed a noticeable fluorescence enhancement of S101 on the NP substrate (by 11 times), and streak-camera images with TRF spectra further implied an increase in the radiative decay rate for S101. From the TRF results, the average fluorescence lifetimes of S101 were calculated to 1.21 ns and 0.45 ns in the absence and presence of NPs, respectively.

A better understanding of the NP effects shown in Figure 3.4 can be obtained from the structural features depicted in Figure 3.1. As already discussed, dye molecules are selectively located inside the PVP core with a diameter of ~ 14 nm and are separated from the NPs by PS coronas of micelles (Figure 3.1). Also, the diameter of micelles, i.e., center-to-center distance, was ~ 34 nm. This physical dimension of micelles now sets the

lower and upper bounds on the NP-fluorophore distance, which can be evaluated from the size of the micelles; the lower bound can be determined by subtracting the core radius (~7 nm) from the micellar radius (~ 17 nm) and the upper bound can be found by adding the core diameter (~ 14 nm) to the lower limit. Therefore, the lower and upper bounds defined by the micellar structures permit the placement of fluorophores in a region of 10 nm ~ 24 nm from the surface of NPs and this region is particularly important as long as NP-fluorophore interactions are concerned. From the knowledge in past, it has been found that no specific near-field interactions might be expected if fluorophores are separated from the surface of NPs beyond ~ 30 nm.[1,6,14] This is because the local fields around metal NPs rapidly decrease with distance. In this sense, the upper bound prevents the large alienation of the dyes beyond the effective NP-fluorophore distance. At the same time, the lower bound restricts the dyes from approaching closer than 10 nm to the surface of NPs and this separation can prevent the quenching effect.[1,6,14] In fact, the excited-state energy of fluorophores can be transferred to metal NPs and then dissipated as heat. This non-radiative energy transfer is inversely proportional to the 4th power of NP-fluorophore distance[13a] and typically occurs if fluorophores are located too close to the NP surface. By setting the value of the lower bound to the minimum NP-fluorophore distance, the maximum efficiency of the non-radiative energy transfer process was calculated using nanometal surface energy transfer (NSET) model.

To examine the quenching effect by non-radiative energy transfer to metal NPs, we calculated the quenching efficiency (E_{ET}) according to a

recent empirical equation[24]

$$E_{ET} = 1 - \frac{1}{1 + (d_0 / d)^4} \text{ ---------- Eq. (3.1)}$$

where d_0 is the characteristic distance at which 50 % quenching occurs, and d is the distance between dyes and the surface of metal NPs, which can be considered as the value of lower bound (10 nm).

The characteristic distance of d_0 can be calculated by

$$d_0 = \left(\frac{0.225 c^3 Q^0}{\omega_{donor}^2 \omega_F k_F} \right)^{1/4} \text{ ---------- Eq. (3.2)}$$

where c is the speed of light (3×10^{10} cm s^{-1}), Q^0 is the quantum yield of the dyes, ω_{donor} is the angular frequency for the donor (R123 = 3.49×10^{15} s^{-1}, S101 = 3.14×10^{15} s^{-1}), ω_F is the angular frequency for bulk silver (8.3×10^{15} s^{-1}), and k_F is the Fermi wavevector for bulk silver (1.2×10^8 cm^{-1}).[24a] The quantum yields of R123 and S101 were determined as 0.43 and 0.25, respectively, by referencing dilute ethanol solutions of the same dyes. By inserting these values into Eq. (3.2), the values of d_0 were determined as 6.8 nm for R123 and 6.3 nm for S101. Therefore, the efficiencies of non-radiative energy transfer could be evaluated from Eq. (3.1) and were 0.17 for R123 and 0.14 for S101.

Hence, the quenching effect by this energy-transfer mechanism can be substantially prevented by the micellar structures. Based on these considerations, one can conclude that the micellar structure optimizes the NP-

fluorophore distance for fluorescence enhancement. At the same time, another aspect that has to be considered is the extinction of metal NPs, which can be separated into absorption and scattering spectra by Mie theory.[1,3,6,15] Calculations with Mie theory clearly showed that Ag NPs in this study have a superior scattering component in their extinction spectrum (Figure 3.5). Since NP agglomeration is not noticeable (Figure 3.1c) and the shape of Ag NPs is mostly spherical (Figure 3.1b), Mie theory can be utilized to resolve the extinction spectrum of Ag NPs. To this end, we used MieCalc program that is available as an open source.[25] By specifying the value of diameter of Ag NP (58 nm in Figure 3.1b), the center of the extinction spectrum (454 nm in Figure 3.5c), and the refractive index of the medium (n = 1.59 for PS block), the extinction spectrum of Ag NPs was resolved into scattering and absorption components (Figure 3.5), which clearly illustrates the superior scattering component (red dashed line) compared to the absorption component (green dashed line). It would be instructive to note that the calculated extinction spectrum (solid line in Figure 3.5) is quite similar to the measured extinction spectrum of Ag NPs in Figure 3.2c.

Therefore, they potentially enhance the fluorescence if the NP-fluorophore distance was engineered as described above. All together, these features are responsible for the spectroscopic results in Figure 3.4 and can be considered as a solution to the problems that could not be easily solved by other assembling methods. It needs to be further emphasized that the increase in micellar size by changing the molecular weight of the copolymers gave rise to a gradual decrease in the fluorescence enhancement (Figure 3.6).

To adjust the size of the PVP core and PS corona, we employed a series of PS-PVP copolymers having different molecular weights. Namely, PS(25)-PVP(7), PS(51)-PVP(18), and PS(128)-PVP(34) were selected, at which the numbers in the parentheses are the number average molecular weights of each block in kg/mol (Polymer Source, Inc.). Further information on the copolymers can be found in Table 3. In fact, PS(25)-PVP(7) was used for the results in the main text but also included here for a clear comparison. With the same procedure, a 0.5 wt% toluene solution of each PS-PVP micelle was prepared and then spin-coated on the substrate. Then, the internal structures of the micellar films were compared in TEM images (Figure 3.6 (a, c, e)). Clearly, the sizes of the PVP cores and PS coronas gradually increased with molecular weight of the copolymers from Figure 3.6a to 3.6e. After analyzing the TEM images, the average core diameter and center-to-center distance of the micelles were calculated in each case (Table 3).

In the solution of PS-PVP micelles, R123 was incorporated into the PVP core with the same condition before ([R123]/[VP] = 0.005). Then, micelles with R123 were coated on the NP substrate and a bare substrate to understand the size effect. From the steady-state fluorescence in Figure 3.6b–3.6f, the enhancement factor was calculated by the ratio of the fluorescence intensity on the NP substrate (solid line) to that on the bare substrate (dashed line) and it gradually decreased with the micellar sizes. The calculated enhancement factor from each micelle was included in Table 3. In other words, the increase of micellar size alienated dye molecules from the optimum NP-fluorophore distance defined by PS(25)-PVP(7) micelles, which resulted in

the gradual decrease in the fluorescence enhancement.

Having verified the fundamental aspects in Figure 3.1 and 3.4, another opportunity was brought to our attention that is surface-plasmon-enhanced simultaneous fluorescence. Before discussing this, several aspects have to be addressed.[18,21] (1) Because of the spectral overlap between the emission of R123 and absorption of S101, they work as a donor-acceptor pair for fluorescence resonance energy transfer (FRET) (Figure 3.7a). Figure 3.7a is normalized UV-Vis (dashed line) and fluorescence (solid line) spectra from ethanol solutions (2.0×10^{-5} M) of R123 (green) and S101 (red), which clearly shows the spectral overlap between the emission of R123 and absorption of S101. (2) When R123 and S101 were mixed in a solution state, the fluorescence from S101 was mainly observed by FRET from R123 (donor) to S101 (acceptor) (Figure 3.7b). When independently-prepared solutions of R123 and S101 were mixed at a 1:1 ratio, the fluorescence of R123 at 550 nm was substantially quenched while that of S101 at 605 nm was noticeably enhanced (violet line in Figure 3.7b), indicating an effective FRET from R123 (donor) to S101 (acceptor). For comparison, the fluorescence spectra from only R123 (green) and from only S101 (red) are also included. (3) Separation of R123 and S101 beyond their Förster radius can inhibit FRET, allowing simultaneous fluorescence from both R123 and S101. (4) If multiple fluorophores are coupled with the surface plasmon of metal NPs to enhance their fluorescence simultaneously, in principle, the consequence can be applied to many fields of science necessitating multi-color signaling such as white emission in optoelectronics[1,4,8] or multiplex cell-imaging.[9,10b,22]

Conceiving of this opportunity, we decided to mix independently prepared micelles with R123 and micelles with S101 in equal amounts. Then, a single-layered film of mixed micelles containing R123 and S101 in different cores was spin-coated on the NP substrate and bare substrate. In Figure 3.8a, steady-state fluorescence clearly shows that the fluorescence of R123 at 540 nm and S101 at 600 nm are simultaneously enhanced on the NP substrate (pink solid line) compared to the same mixed micelles on the bare substrate (gray dashed line). However, the degrees of fluorescence enhancement of R123 and S101 are reduced compared to the independent enhancement shown in Figure 3.4. The decreased amount of each dye in the mixed micellar film is responsible for this observation because we mixed independently-prepared micelles in a 1:1 ratio before coating. Time-dependant spectral changes of both dyes on the bare substrate (Figure 3.8b) and on the NP substrate (Figure 3.8c) were further compared by the Streak Camera technique. In the comparison, we found that initial intensity of both the R123 and S101 fluorescence on the NP substrate became much higher as illustrated by the colors. However, in the case of the mixed micelles, the fluorescence decay of the dyes has to be more carefully analyzed in order to confirm that the near-field interactions arose not only from the close proximity of the dyes to Ag NPs but also from proximity of R123 and S101. In this respect, the Streak Camera technique proves to be very useful as it allows the extraction of decay profiles of R123 and S101 at different wavelengths. The TRF spectra of R123 at 540 nm (Figure 3.8d) and S101 at 600 nm (Figure 3.8e) clearly show that the decays of R123 (green circles) and S101 (red circles) on the NP substrate

became much faster than those on the bare substrate (gray circles). The average lifetimes were calculated as 1.93 ns for R123 and 1.33 ns for S101 on the bare substrate, but shortened to 0.63 ns for R123 and 0.49 ns for S101 on the NP substrate (see Table 2). Strikingly, those values are virtually similar to the average lifetimes independently obtained in Figure 3.4. In other words, the fluorescence dynamics of both R123 and S101 in the mixed micellar film remained unaffected in comparison with the independent experiments in Figure 3.4g and 3.4h. Therefore, it can be concluded that fluorescence enhancement occurs separately in each micellar core without FRET between R123 and S101, which produces the steady-state fluorescence result in Figure 3.8a. If FRET occurred in the micellar film, the lifetime of R123 in the mixed film had to be decreased in the presence of S101.[18b,21] It appears that the separation of R123 and S101 in different micellar cores beyond their Förster radius is responsible for FRET inhibition.

FRET efficiency (E_{FRET}) can be determined by[21]

$$E_{FRET} = \frac{R_0^6}{R_0^6 + r^6} \text{ ---------- Eq. (3.3)}$$

where R_0 is the Förster radius and r is the donor-acceptor distance. In order to understand the restricted FRET in Figure 3.8, we first calculated R_0 and r in the micellar system.

The Förster radius (R_0) of R123 and S101 can be calculated by[21]

$$R_0 = 0.211[k^2 n^{-4} Q_D J(\lambda)]^{1/6} \text{ ---------- Eq. (3.4)}$$

where Q_D is the quantum yield of the donor (measured as 0.43), k^2 is the

orientation factor (assumed as 2/3 corresponding to a random orientation), n is the refractive index of the medium (1.59 for PS blocks), and $J(\lambda)$ is the donor-acceptor overlap integral .

The overlap integral can be obtained by

$$J(\lambda) = \int_0^\infty f_D(\lambda)\varepsilon_A(\lambda)\lambda^4 d\lambda \text{ ---------- Eq. (3.5)}$$

where f_D is the normalized emission intensity of the donor, ε_A is the wavelength-dependent extinction coefficient of the acceptor, and λ is the wavelength in nanometer. $J(\lambda)$ was evaluated as 3.62×10^{15} M^{-1} cm^{-1} nm^4 from the absorption and fluorescence spectra of R123 and S101 in the micelles (not shown). By inserting the value of $J(\lambda)$ in Eq. (3.5), R_0 was evaluated as 4.9 nm. At the same time, the donor-acceptor distance (r) in the mixed-micellar film containing R123 (donor) and S101 (acceptor) in different cores is at least the thickness of the PS coronas separating each PVP core. From Figure 1a, the thickness of the PS corona was evaluated as 20 nm. With this information, the FRET efficiency was calculated as 2.16×10^{-4} from Eq. (3.3), indicating negligible FRET in the mixed-micellar film.

3.4. Conclusions

In conclusion, we discussed the strong correlation of micellar structures with surface-plasmon-coupled fluorescence. The inherent self-segregating property of block copolymer micelles sets clear bounds for the arrangement of fluorophores in the vicinity of NPs for the fluorescence enhancement that would not be easily achieved by other assembling methods. These features of copolymer micelles can find many opportunities in plasmonic applications. Relevance-future direction can be suggested as the modification of chemical structures of the copolymer to form a thin metal shell on the micelles. By coating metal shells on the coronas of micelles that contain dyes in the cores, dual functionalities of plasmon and fluorescence might be achieved, which can be a promising blueprint for cell-imaging and diagnostics.

3.5. References

[1] V. Giannini, A. I. Fernández-Domíguez, S. C. Heck, S. A. Maier, *Chem. Rev.* **2011**, *111*, 3888.

[2] L. Novotny, N. Van Hulst, *Nat. Photonics* **2011**, *5*, 83.

[3] M. Rycenga, C. M. Cobley, J. Zeng, W. Li, C. H. Moran, Q. Zhang, D. Qin, Y. Xia, *Chem. Rev.* **2011**, *111*, 3669.

[4] J. A. Schuller, E. S. Barnard, W. Cai, Y. C. Jun, J. S. White, and M. L. Brongersma, *Nat. Mater*. **2010**, *9*, 193.

[5] H. A. Atwater, A. Polman, *Nat. Mater*. **2010**, *9*, 205.

[6] J. R. Lakowicz, K. Ray, M. Chowdhury, H. Szmacinski, Y. Fu, J. Zhang, K. Nowaczyk, *Analyst* **2008**, *133*, 1308.

[7] J. N. Anker, W. P. Hall, O. Lyandres, N. C. Shah, J. Zhao, R. P. Van Duyne, *Nat. Mater*. **2008**, *7*, 442.

[8] a) T. H. Kim, K. S. Cho, E. K. Lee, S. J. Lee, J. Chae, J. W. Kim, D. H. Kim, J. Y. Kwon, G. Amaratunga, S. Y. Lee, B. L. Choi, Y. Kuk, J. M. Kim, K. Kim, *Nat. Photonics* **2011**, *5*, 176; b) A. Kinkhabwala, Z. Yu, S. Fan, Y. Avlasevich, K. Müllen, W. E. Moerner, *Nat. Photonics*, **2009**, *3*, 654.

[9] P. K. Jain, X. Huang, I. H. El-Sayed, M. A. El-Sayed, *Acc. Chem. Res*. **2008**, *41*,1578.

[10] a) S. Mayilo, M. A. Kloster, M. Wunderlich, A. Lutich, T. A. Klar, A. Nichtl, K. Kürzinger, F. D. Stefani, J. Feldmann, *Nano Lett.* **2009**, *9*, 4558; b) N. L. Rosi, C. A. Mirkin, *Chem. Rev*. **2005**, *105*, 1547.

[11] a) J. M. Slocik, A. O. Govorov, R. R. Naik, *Nano Lett.* **2011**, *11*, 701; b) S. R. Beyer, S. Ullrich, S. kudera, A. T. Gardiner, R. J. Cogdell, J. Köhler, *Nano Lett.* **2011**, *11*, 4897; c) S. Mackowski, S. Wörmke, A. J. Maier, T. H. P. Brotosudarmo, H. Harutyunyan, A. Hartschuh, A. O. Govorov, H. Scheer, C. Bräuchle, *Nano Lett*. **2008**, *8*, 558; d) J. Lee, T. Javed, T. Skeini, A. O. Govorov, G. W. Bryant, N. A. Kotov, *Angew. Chem. Int. Ed.* **2006**, *45*, 4819.

[12] a) K. Munechika, Y. Chen, A. F. Tillack, A. P. Kulkarni, I. J. L Plante, A. M. Munro, D. S. Ginger, *Nano Lett*. **2010**, *10*, 2598; b) R. Bardhan, N. K. Grady, J. R. Cole, A. Joshi, N. J. Halas, *Acs Nano* **2009**, *3*, 744; c) Y. Chen, K. Munechika, I. Jen-La Plante, A. M. Munro, S. E. Skrabalak, Y. Xia, D. S. Ginger, *Appl. Phys. Lett*. **2008**, *93*, 053106.

[13] a) M. P. Singh, G. F. Strouse, *J. Am. Chem. Soc*. **2010**, *132*, 9383; b) Y. Chem, K. Munechika, D. S. Ginger, *Nano Lett*. **2007**, *7*, 690; c) F. Tam, G. P. Goodrich, B. R. Johnson, N. J. Halas, *Nano Lett.* **2007**, *7*, 496.

[14] a) Y. Jin, X. Gao, *Nat. Nanotechnol*. **2009**, *4*, 571; b) G. Schneider, G. Decher, N. Nerambourg, R. Praho, M. H. V. Werts, M. Blanchard-Desce, *Nano Lett*. **2006**, *6*, 530; c) P. Anger, P. Bharadwaj, L. Novotny, *Phys. Rev. Lett*. **2006**, *96*, 113002; d) O. Kulakovich, N. Strekal, A. Yaroshevich, S. Maskevich, S. Gaponenko, I. Nabiev, U. Woggon, M. Artemyev, *Nano Lett*. **2002**, *2*, 1449.

[15] E. Hao, G. C. Schatz, *J. Chem. Phys.* **2004**, *120*, 357.

[16] a) N. Liu, B. S. Prall, V. I. Klimov, *J. Am. Chem. Soc*. **2006**, *128*, 15362; b) M. A. Noginov, G. Zhu, A. M. Belgrave, R. Bakker, V. M. Shalaev, E. E. Narimanov, S. Stout, E. Herz, T. Suteewong, U. Wiesner, *Nature*, **2009**, *460*, 1110; c) M. Lessard-Viger, M. Rioux, L. Rainville, D. Boudreau, *Nano Lett*. **2009**, *9*, 3066.

[17] a) R. Glass, M. Möller, J. P. Spatz, *Nanotechnology* **2003**, *14*, 1153; b) S. Förster, M. Antonietti, *Adv. Mater*. **1998**, *10*, 195.

[18] a) S. I. Yoo, S. J. An, G. H. Choi, K. S. Kim, G.-C. Yi, W.-C. Zin, J. C. Jung, B. H. Sohn, *Adv. Mater*. **2007**, *19*, 1594; b) S. I. Yoo, S. H. Bae, K. S. Kim, B. H. Sohn, *Soft Matter* **2009**, *5*, 2990; c) G. Rainò, T. Stöferle, C. Park, H. C. Kim, T. Topuria, P. M. Rice, I. J. Chin, R. D. Miller, R. F. Mahrt, *ACS Nano*, **2011**, *5*, 3536; d) M. Moffitt, A. Eisenberg, *Chem. Mater*. **1995**, *7*, 1178.

[19] a) Z. S. Pillai, P. V. Kamat, *J. Phys. Chem. B*. **2004**, *108*, 945; b) A. D. McFarland, R. P. Van Duyne, *Nano Lett*. **2003**, *3*, 1057.

[20] V. Kamm, G. Battagliarin, I. Howard, W. Pisula, A. Mavrinskiy, C. Li, K. Müllen, F. Laquai, *Adv. Energy Mater*. **2011**, *1*, 297.

[21] J. R. Lakowicz, in *Principles of Fluorescence Spectroscopy*, 3rd ed. Kluwer Academic/Plenum: New York, **2006**.

[22] a) S. H. Cao, W. P. Cai, Q. Liu, Y. Q. Li, *Annu. Rev. Anal. Chem*. **2012**, *5*, 317; b) R. Robelek, L. Niu, E. L. Schmid, W. Knoll, *Anal. Chem*. **2004**, *76*, 6160.

[23] B. H. Sohn, T. H. Kim, K. Char, *Langmuir* **2002**, *18*, 7770.

[24] a) S. Saraswat, A. Desireddy, D. Zheng, L. Guo, H. P. Lu, T. P. Bigioni, D. Isailovic, *J. Phys. Chem. C*. **2011**, *115*, 17587; b) T. L. Jennings, M. P. Singh, G. F. Strouse, *J. Am. Chem. Soc*. **2006**, *128*, 5462.

[25] C. F. Bohren and D. Huffman, MieCalc-freely configurable program for light scattering calculations (Mie theory), **2006**, http://www.lightscattering.de/MieCalc/eindex.html.

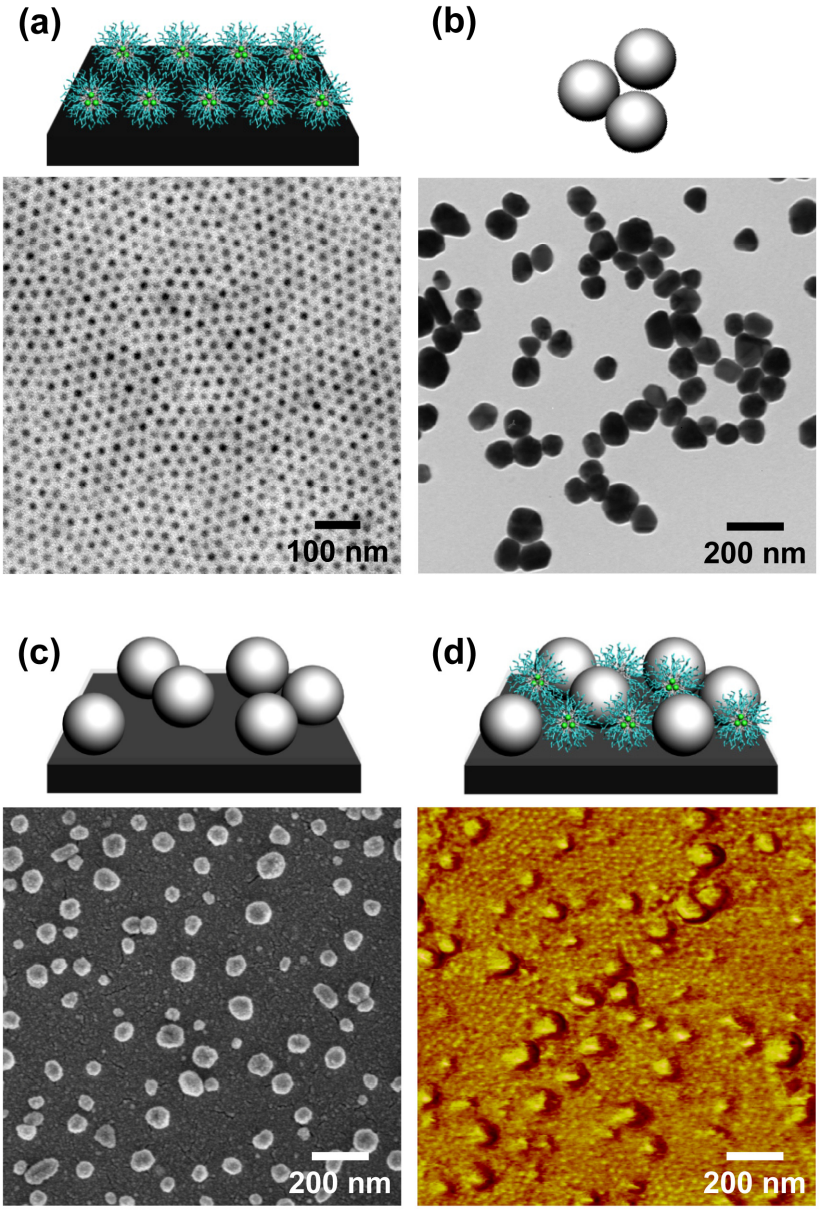

Figure 3.1. (a) TEM image of a single-layered film of PS-PVP micelles; (b) TEM image of citrate-stabilized Ag NPs; (c) SEM image of Ag NPs coated on $[PAH/PSS]_3/PAH$; (d) AFM image of PS-PVP micelles containing dyes coated on the NP substrate. In the TEM image, PVP blocks were stained by I_2 and appeared as dark spheres.

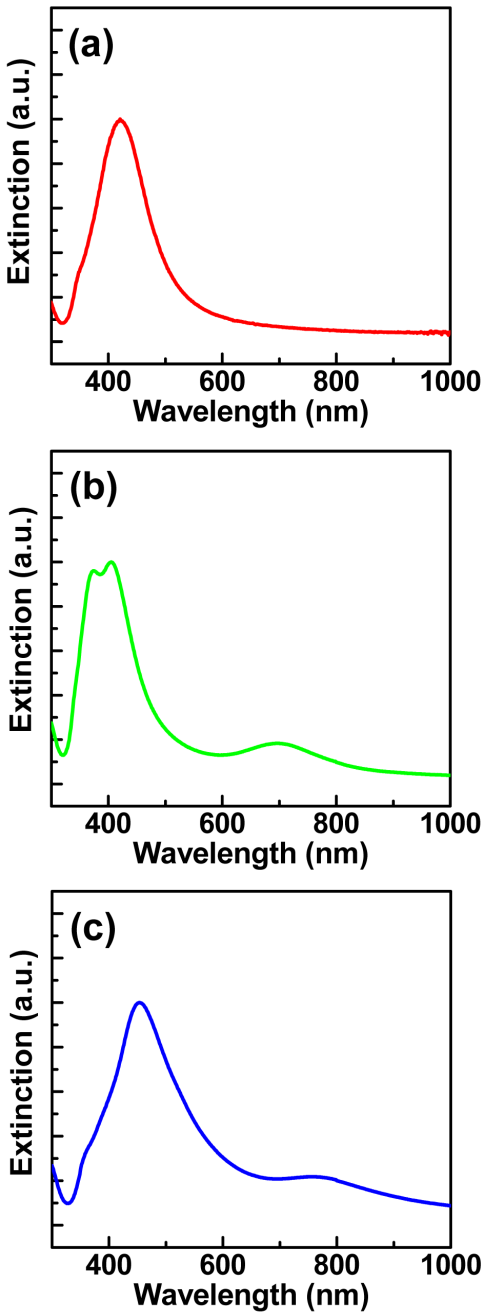

Figure 3.2. Extinction spectra of Ag NPs. (a) in aqueous solution; (b) on quartz substrate; (c) after being coated by PS-PVP micelles.

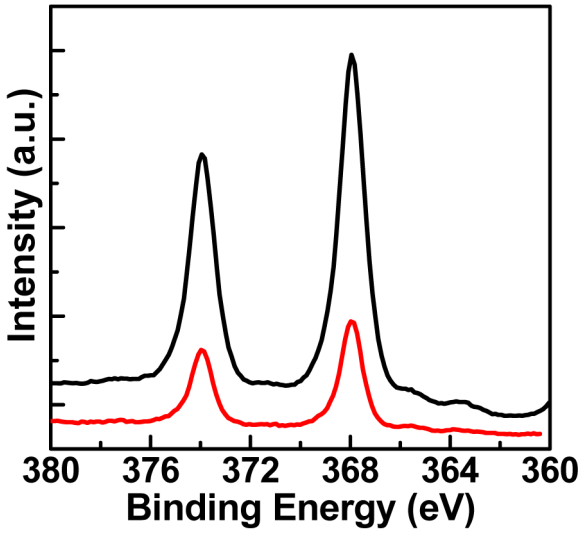

Figure 3.3. X-ray photoelectron spectra of Ag peak before (black) and after (red) being coating by PS-PVP micelles.

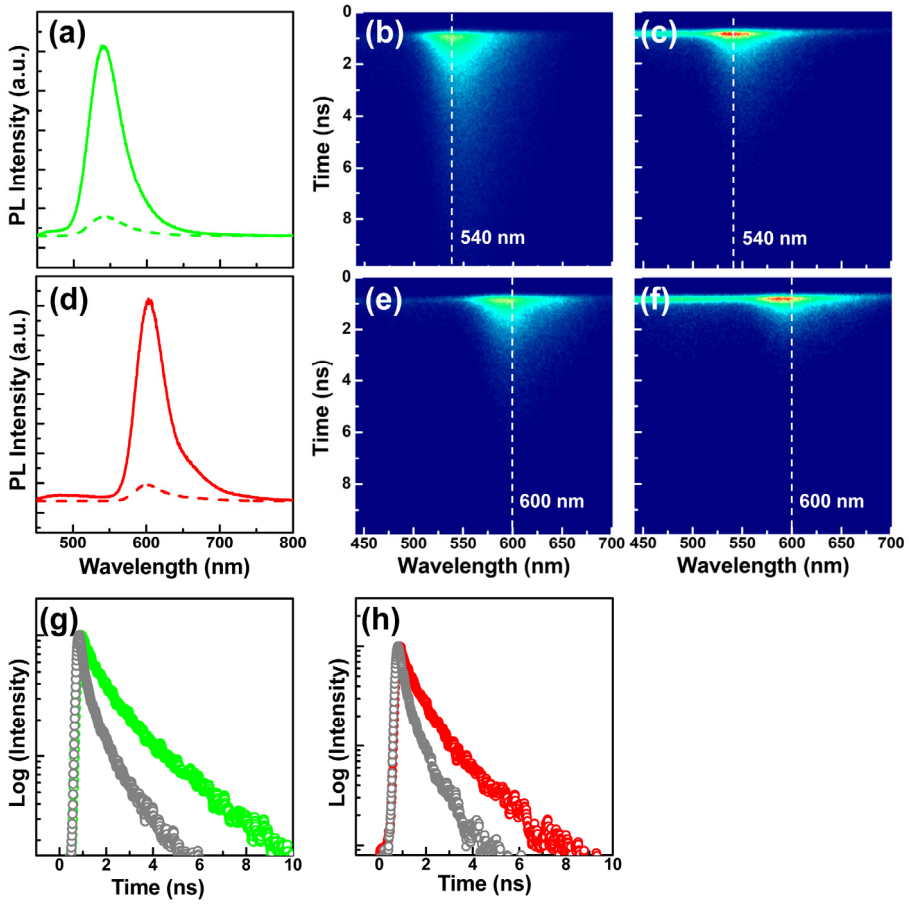

Figure 3.4. Spectroscopic results from single-layered films of micelles containing R123 and micelles containing S101. (a) Steady-state fluorescence spectra of R123 on the bare (gray dashed) and NP (green solid) substrates; (b, c) Streak camera images from R123 on the bare (b) and NP (c) substrates; (g) Normalized TRF spectra of R123 at 540 nm on the bare (gray open circles) and NP (green open circles) substrates. (d) Steady-state fluorescence spectra of S101 on the bare (gray dashed) and NP (red solid) substrates; (e, f) Streak camera images from R123 on the bare (e) and NP (f) substrates; (h) Normalized TRF spectra of S101 at 600 nm on the bare (gray open circles) and NP (red open circles) substrates.

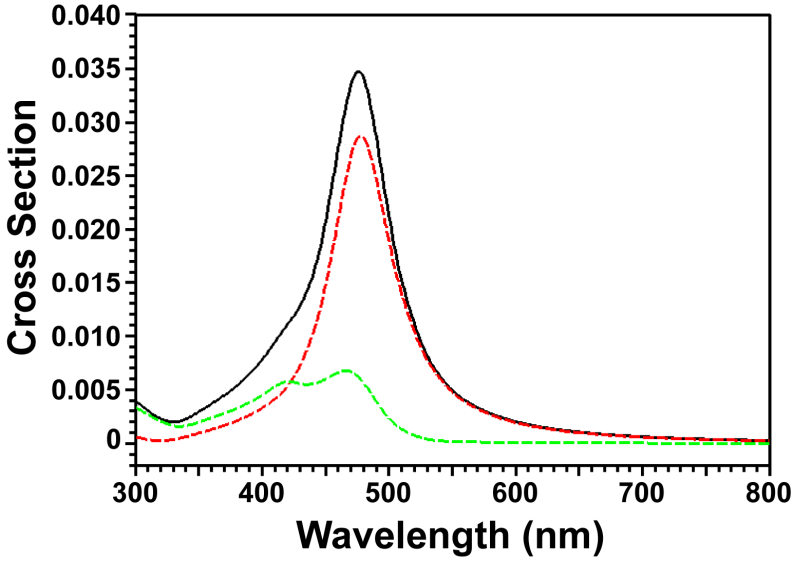

Figure 3.5. Calculated optical cross-section of the extinction spectrum of Ag NPs with a 58 nm diameter and a refractive index of the surrounding medium of 1.59. The extinction spectrum is a sum of the scattering component (red dashed) and absorption component (green dashed).

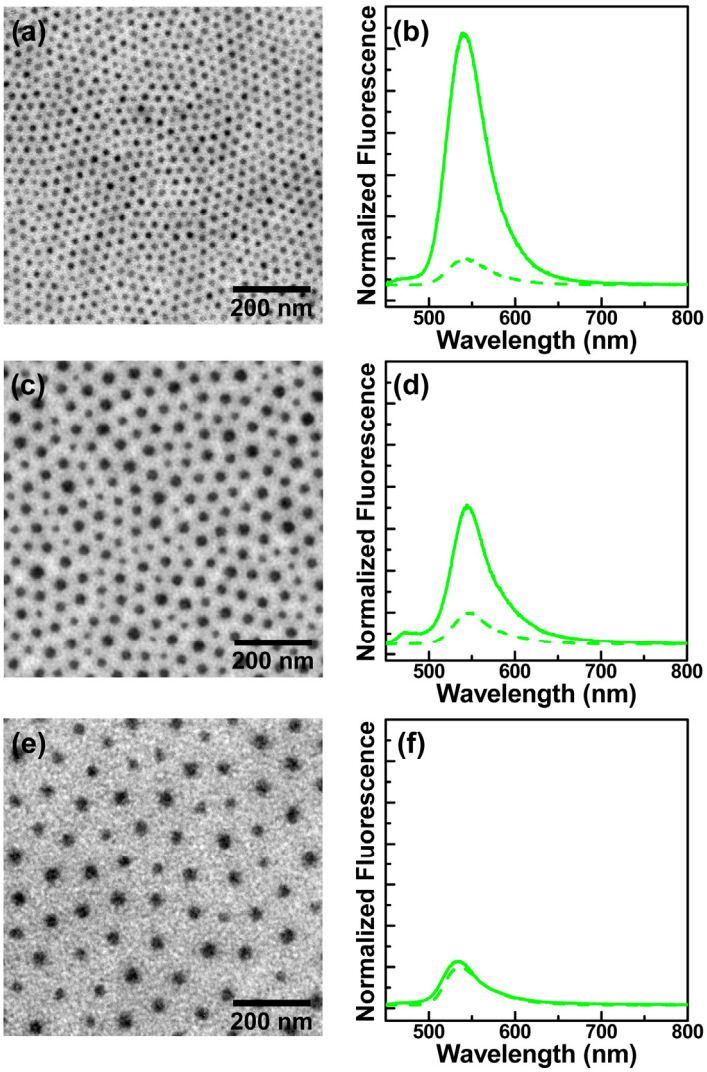

Figure 3.6. TEM images of single-layered films of PS-PVP micelles having different molecular weights of PS and PVP blocks. Steady-state fluorescence spectra from PS-PVP micelles with R123 on the bare (dashed line) and the NP (solid line) substrates: (a, b) PS(25)-PVP(7); (c, d) PS(51)-PVP(18); (e, f) PS(128)-PVP(34). Steady-state fluorescence was normalized by the maximum fluorescence intensity of the dyes on a bare substrate. The excitation wavelength was 442 nm.

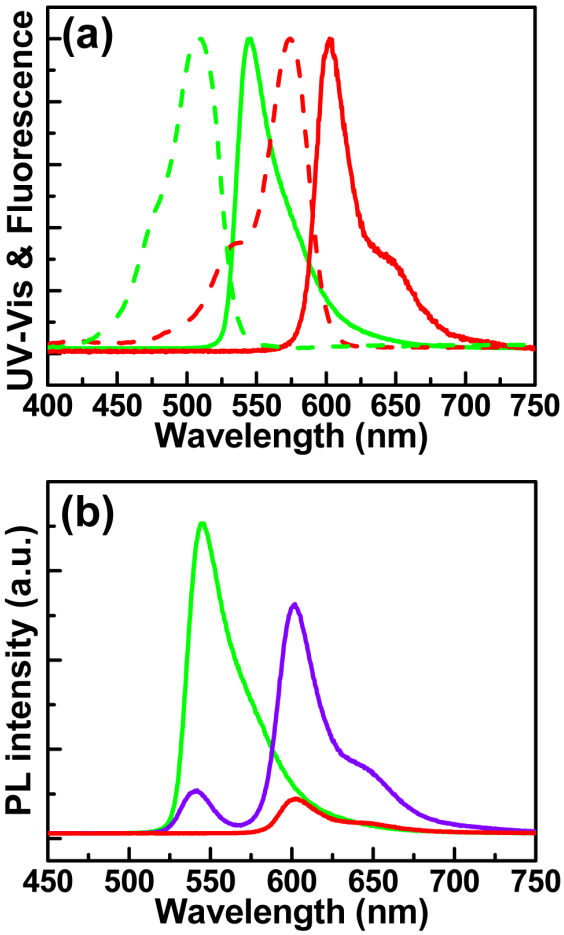

Figure 3.7. (a) Normalized UV-Vis (dashed line) and steady-state fluorescence (solid line) spectra from ethanol solutions of R123 (green) and S101 (red). (b) Steady-state fluorescence spectra of ethanol solutions of R123 (green), S101 (red), and mixture of R123 and S101 (purple). The excitation wavelength was 442 nm.

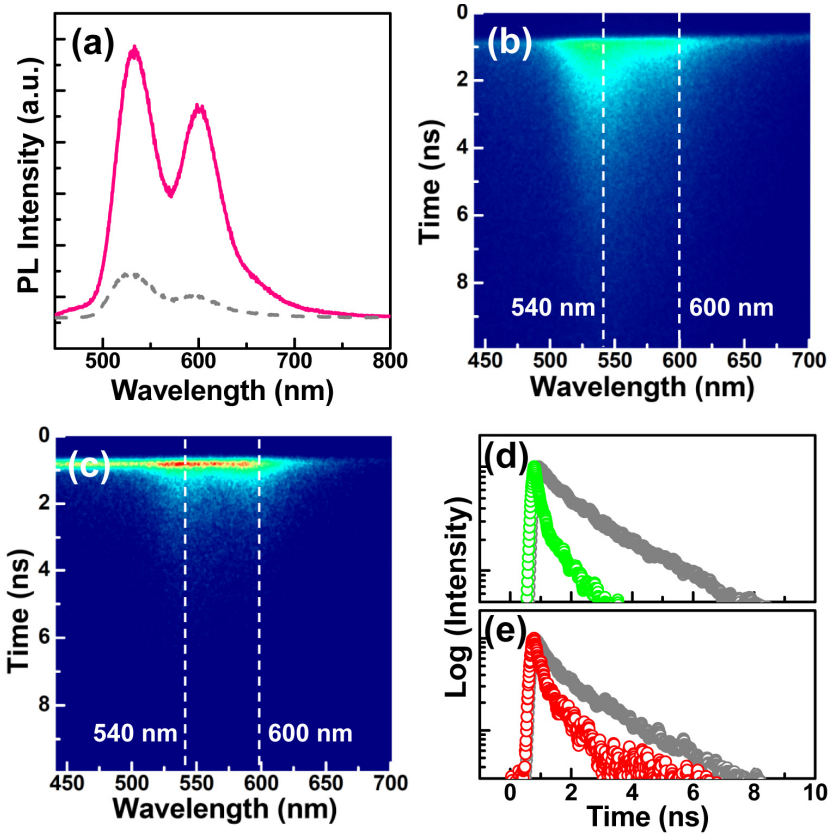

Figure 3.8. Spectroscopic results from a single-layered film of mixed micelles containing R123 and S101 in different cores. (a) Steady-state fluorescence spectra from mixed micelles on the bare (gray dashed) and NP (pink solid) substrates; (b, c) Streak camera images from mixed micelles on the bare (b) and NP (c) substrates; (d) Normalized TRF spectra of R123 at 540 nm from mixed micelles on the bare (gray circles) and NP (green circles) substrates; (e) Normalized TRF spectra of S101 at 600 nm from mixed micelles on the bare (gray circles) and NP (red circles) substrates.

Tables: Time components of TRF spectrum

The decay of fluorescence intensity (I(t)) can be modeled as the sum of individual exponentials that is described by[21]

$$I(\mathrm{t}) = \sum_i \alpha_i \exp(-t/\tau_i) \text{ ---------- Eq. (3.6)}$$

where τ_i are the individual lifetimes and α_i are the amplitudes. Here, we normalized the values of α_i to $\sum_i \alpha_i = 1$, so the average lifetime of the dyes can be obtained by $\tau_{ave} = \sum_i \alpha_i \tau_i$. After fitting the TRF results in Figure 3.4 and 3.8 with the multiexponential Eq. (3.6), the amplitude (α_i), lifetime (τ_i), and average lifetime (τ_{ave}) of the dyes on bare and NP substrates were calculated and summarized in Table 3.1 and 3.2.

samples	α_1 (%)	τ_1 (ns)	α_2 (%)	τ_2 (ns)	τ_{ave}(ns)
R123 (bare)	74	1.22	26	3.64	1.84
R123 (NPs)	72	0.36	28	1.61	0.71
S101 (bare)	62	0.64	38	2.17	1.21
S101 (NPs)	78	0.25	22	1.14	0.45

Table 3.1. Time components obtained from micelles containing R123 or micelles containing S101 on the bare and NP substrates, i.e., from Figure 2d and 2h.

samples	α_1 (%)	τ_1 (ns)	α_2 (%)	τ_2 (ns)	τ_{ave} (ns)
R123 (bare)	73	1.28	27	3.69	1.93
R123 (NPs)	74	0.25	26	1.68	0.63
S101 (bare)	52	0.42	48	2.31	1.33
S101 (NPs)	77	0.18	23	1.55	0.49

Table 3.2. Time components obtained from mixed micelles containing R123 and S101 on the bare and NP substrates, i.e., from Figure 3.8d and e.

block copolymer	PS (g/mol)[a]	PVP (g/mol)[a]	PDI	core diameter (nm)	center-to-center distance (nm)	enhancement factor[b]
PS(25)-PVP(7)	25,000	7,000	1.10	14	34	10.0
PS(51)-PVP(18)	51,000	18,000	1.15	27	52	4.4
PS(128)-PVP(34)	128,400	33,500	1.17	28	98	1.1

Table 3.3. Physical dimension of PS-PVP micelles and the corresponding enhancement factor. [a] the number average molecular weights of each block. [b] enhancement factor was calculated from Figure 3.6b–f.

Chapter 4

Switching Off FRET in the Hybrid Assemblies of Diblock Copolymer Micelles, Quantum Dots, and Dyes by Plasmonic Nanoparticles

4.1. Introduction

Hybridization of dissimilar building materials into highly-organized structures can tailor the functionality of each component by coupling phenomena.[1,2] In particular, the collective oscillation of electrons in metal nanoparticles (NPs) known as a localized surface plasmon resonance gained much attention since light-matter interaction can be engineered by positioning metal NPs in the vicinity of fluorophores such as semiconductor quantum dots (QDs) or fluorescent dyes.[3-6] In this context, metal NPs are often referred to as near-field antennas since they can (1) enhance local electric fields around NPs and (2) engineer the radiative and non-radiative decay rate of fluorophores.[3-6] To understand the nature of NP effect, chemically or lithographically fabricated metal NPs and nanostructures have been widely utilized and found that fluorophores in the vicinity of metal NPs undergo excitation enhancement (increased light absorption), emission enhancement (increased radiative decay), or quenching (increased non-radiative decay).[4-15] These competitive near-field interactions arose from several experimental parameters such as the extinction characteristics of metal NPs,[7-9] the distance between NPs and fluorophores,[10-12] and spectral overlap between absorption/emission of fluorophores and the extinction of metal NPs.[13,14] The consequence of those understandings now stimulates widespread applications in biology,[6] diagnostics,[15] photonics,[16] and optoelectronics.[17-19]

These recent findings on plasmonics with metal NPs may highlight the apparent similarity with fluorescence resonance energy transfer (FRET) between a donor-acceptor pair of fluorophores. As well formulated, FRET is a

non-radiative through-space energy flow from excited-state donors to ground-state acceptors by dipole-dipole interaction and occurs when the donor-to-acceptor distance is comparable to or smaller than their Förster radius (R_0).[20-25] Therefore, one may envision that donor-acceptor interactions in FRET can be modulated by near-field effects of metal NPs but such a research direction might be quite complex since multiple parameters aforementioned have to be carefully analyzed. Recently, surface-plasmon-coupled FRET systems have been investigated, however only to a limited degree, using self-assembling techniques such as layer-by-layer assembly[15,26] and multilayered core-shell particles.[27] The pre-existing results suggest that metal NPs can strongly enhance the FRET efficiency by increasing the Förster radius.[28,29] Lakowicz et al. inferred that the FRET enhancement might be strongly correlated with a distribution of local electric fields near metal NPs as such an enhancement was more facilitated with larger metal NPs and shorter distance between NPs and donor-acceptor pairs.[6,28] Considering that the Förster radius is usually in the range of 2 - 6 nm and is too short to be widely applicable for immunoassay of typical globular proteins and antibodies,[6,21] they are convinced that such an enhanced FRET will eventually find an opportunity in biological sensing systems.[6,28]

Another important aspect that needs to be considered is that FRET might also be restricted in the vicinity of metal NPs and such a restriction may facilitate new material design as in case of plasmon-coupled light-emitting diodes (LEDs).[17-19] In a current white LED, for example, multiple fluorophores, which can work as a donor–acceptor pair, are often applied to

LED structures to convert high energy photons to low energy ones.[30,31] With regard to the lower device performance, one can utilize metal NPs to enhance the spontaneous emission rate and quantum efficiency of emitting materials.[17-19] However, given that the color of LEDs originates from a composition of fluorophores as well as their interaction with metal NPs, the fine tuning of the emitted color may be quite intricate, unless FRET between multiple fluorophores is restricted.

Perceiving that surface-plasmon-coupled FRET has a fundamental and practical importance in many fields of science, it is important to realize highly-organized nano- or meso- structures consisting of metal NPs and fluorophores and to engineer their interactions on a nanometer scale. As a new step to this direction, we report here that FRET in hybrid assemblies of diblock copolymer micelles, QDs, and dyes can be turned off by silver NPs. Our finding strongly suggests that the decay channels of dissimilar fluorophores can be engineered by metal NPs in a way that inhibits FRET. Diblock copolymer micelles were originally selected because (1) a single-layered film of copolymer micelles in a hexagonal order can be easily fabricated by spin-coating,[32-34] (2) some dye molecules are found to be incorporated solely into the core of micelles,[35-37] and (3) QDs can be positioned at the peripheral region of micelles in their single-layered film.[38-40] These unique properties of copolymer micelles discovered by our group and others provide a precise tool for the nanoscale organization of dyes, QDs, and metal NPs to achieve novel material properties and better understanding of plasmonic effects of metal NPs.

4.2. Experimental Section

Polystyrene-poly(4-vinylpyridine) (PS-PVP) was purchased from Polymer Source, Inc. The number average molecular weight of PS and PVP blocks are 51000 g/mol and 18000 g/mol, respectively, with polydispersity index (PDI) of 1.15. PS-PVP copolymers were dissolved in toluene (0.5 wt%) at room temperature, heated to 70 °C for 3 h, and then cooled to room temperature with mild stirring. Rhodamine 123 (R123, Sigma-Aldrich) was added to a toluene solution of PS-PVP micelles with a molar ratio of [R123]/[VP] = 0.005 and then the solution was vigorously stirred for at least 7 days for a selective inclusion of R123 into PVP cores. QDs of core-shell CdSe@ZnS capped by oleic acid were synthesized as in the literature and then dried under vacuum.[43] Then, QDs in a powdery state were dissolved in the micellar solution (weight percent of QDs in micellar solution was 0.3 wt%). A single-layered film of PS-PVP micelles with and without dyes or QDs was prepared by spin-coating (2000 rpm, 60 s).

To synthesize polyvinylpyrrolidone-stabilized Ag NPs, 10 g of polyvinylpyrrolidone (10000 g/mol, Sigma-Aldrich) was dissolved in 50 mL of ethylene glycol at room temperature. Then, 800 mg of silver nitrate was added to the ethylene glycol solution. The reaction mixture was heated to 120 ^{o}C under stirring for 1 hr to reduce silver nitrate into Ag NPs.[44] To purify Ag NPs, excess amount of acetone was added to the NP solution and the solution was centrifuged at 4,000 rpm for 10 min. After carefully removing the supernatant, the precipitates were redispersed in ethanol. This process was repeated by 4 times. The final concentration of Ag NPs in ethanol was

adjusted as 10 mg/mL, which was used for spin-coating on quartz plates or Si-wafer (2000 rpm, 60 s). Before coating, the substrates were cleaned in a piranha solution (70/30 v/v of concentrated H_2SO_4 and 30 % H_2O_2).

UV-Vis absorption spectra were recorded on a Varian Cary-5000 spectrophotometer. Steady-state fluorescence was measured on an Acton SpectraPro with a He-Cd laser (442 nm) as the excitation source. Time-resolved fluorescence (TRF) was obtained using the time-correlated single-photon counting (TCSPC) technique. The excitation source is a self-mode-locked femtosecond Ti:Sapphire laser (Coherent model Mira 900) pumped by an Nd:YVO_4 laser (Coherent Verdi diode-pumped laser). The laser output has a pulse width of ~ 260 fs and can span excitation wavelengths in the range of 350 ~ 490 nm by second-harmonic generation. The excitation wavelength was 420 nm. All the standard electronics for the TCSPC system were from Edinburgh Instruments, which provided the temporal resolution less than 10 ps after deconvolution of instrument response function (IRF). This picosecond setup can measure the decay and the rise of fluorescence after laser pulse excitation.[52,53] All measurements were performed at room temperature. Surface morphologies of thin films of Ag NPs and hybrid assemblies of PS-PVP micelles, QDs, and dyes were investigated by atomic force microscopy (AFM Nanoscope IIIA. Digital Instrument) in tapping mode with Si cantilevers. The morphology of the nanoparticles and single-layered films of micelles was investigated by transmission electron microscopy (Hitachi 7600) and field-emission scanning electron microscopy (FE-SEM, JSM-6700F JEOL) after Pt coating on the sample.

4.3. Results and Discussion

Polystyrene-poly(4-vinyl pyridine), PS-PVP, diblock copolymers self-associate into spherical micelles consisting of a soluble PS corona and an insoluble PVP core in toluene, which is a selective solvent for PS blocks.[32,41,42] The molecular weight of PS and PVP blocks in this study are 51000 g/mol and 18000 g/mol, respectively, with a polydispersity index (PDI) of 1.15 (Polymer Source Inc). To produce PS-PVP micelles, as-received PS-PVP copolymers were dissolved in toluene (0.5 wt %), stirred for 3 hr at 70 ^{o}C, and then cooled down to room temperature. From the solution, a single-layer film of PS-PVP micelles was fabricated by spin-coating. Transmission electron miscopy (TEM) image (Figure 4.1) showed spherical micelles arranged in a hexagonal order with a dark PVP core and a bright PS matrix without multi-layered structures. The average diameter of PVP cores and the center-to-center distance between micelles were estimated as ~ 27 nm and ~ 52 nm, respectively. This single-layered film of micelles gives a modality for simultaneous positioning of QDs and dyes that will be described from now on.

For a donor-acceptor pair in this study, QDs of core-shell CdSe@ZnS capped by oleic acid were synthesized[43] as a donor and commercially available rhodamine 123 (R123) was selected as an acceptor. Since the emission/absorption spectra of QDs can be tuned by quantum confinement, one can easily induce the spectral overlap between emission of QD donor and absorption of dye acceptor, which is necessary for FRET studies.[20-25] To produce hybrid assemblies of PS-PVP micelles with QDs and dyes, we first loaded R123 into the PVP core of micelles with a molar ratio of [R123]/[VP]

= 0.005. While R123 dyes were not soluble and remained powdery in toluene without micelles, a homogenous solution was prepared after adding R123 to the micellar solution with vigorous stirring (~ 7 days) by a selective inclusion of dyes into the hydrophilic PVP cores.[36,37] The amount of R123 in the PVP core can be controlled by changing the molar ratio of [R123]/[VP], which was confirmed from a gradual change of fluorescence intensity in a dose-dependent manner (Figure 4.2). Different amount of dye molecules was added to a toluene solution of PS-PVP micelles and then the solution was stirred as in the previous case. Then, single-layered films of micelles with dyes were prepared to compare the fluorescence intensity of dyes in the PVP core. As shown in Figure 4.2, fluorescence intensity was gradually increased and then decreased with the molar ratio of [R123]/[VP]. At the same time, the maximum peak position was red-shifted, accordingly. Noticing that the decreased and red-shifted fluorescence can be ascribed to the self-quenching of dyes by their agglomeration in the PVP core, these results confirm that the amount of dyes in the PVP cores can be controlled in a dose-dependent manner.

Then, QDs (having ~ 8.7 nm in diameter) were added to the dye-loaded micellar solution (0.3 wt % to the micellar solution). The oleic acid coating on the surface of QDs provided appreciable solubility in toluene and also chemical stability.[43a] From the mixture, a single-layered film of micelles with R123 and QDs was prepared by spin-coating (2000 rpm, 60 sec), the structure of which was examined by TEM.

In Figure 4.3a, QDs appear as small dark spots and are distributed around spherical micelles while PS-PVP micelles are indirectly discernible in the region surrounded by QDs. In addition, PVP cores are recognizable by a gray spherical area in the center of each micelle even without staining due to their height difference. Noticeably, QDs are mostly located at the peripheral region of PS-PVP micelles without macroscopic separation from them. The center-to-center distance between micelles was increased from 52 nm to 59 nm by the inclusion of QDs. Since the surface of QDs was functionalized by oleic acid, they were not compatible with the polar PVP core or aromatic PS corona. Therefore, they are physically entrapped between the micelles by a lateral capillary force during the coating process.[38-40] In addition, QDs themselves are separated from each other in a regular spacing (~ 2.7 nm) without noticeable agglomerations due to the capping agent. While surface modification of QDs by thiol-functionalized polystyrene (PS) can provide compatibility with PS corona, PS coating also substantially increases the QD size.

To prepare PS-coated QDs, thiol-functionalized PS (5000 g/mol) was synthesized by RAFT (Reversible Addition-Fragmentation chain Transfer) polymerization as in the literature.[43b] For a ligand exchange reaction, excess amount of thiol-functionalized PS was added to a toluene solution of neat QDs and the solution was vigorously stirred for 24 hr. Then, excess amount of hexane, that is a poor solvent for PS, was added to the solution, followed by centrifugation (4000 rpm, 30 min). After removing the supernatant, the precipitates were collected and then dried. Since PS homopolymers cannot be

removed by this procedure, they are co-precipitated with PS-coated QDs. After that, PS-coated QDs were added to the micellar solution with a weight ratio of 0.3 wt%. From the mixture solution, micellar film with QDs was prepared by spin-coating, the internal structure of which was analyzed by TEM. In Figure 4.4, the hexagonal order of micelles is some or less deteriorated because the residual PS homopolymers can be blended with PS coronas of micelles. Nevertheless, most of PS-coated QDs are macroscopically separated from the micelles presumably because PS-coated QDs are too bulky to occupy the peripheral region of the micelles.

From TEM image of Figure 4.4, PS-coated QDs are found to be macroscopically separated from the micelles presumably because PS-coated QDs are too bulky to occupy the peripheral region of the micelles. With respect to the location of dye molecules, they are most likely located in the PVP cores (gray area in TEM image) because glassy PVP cores can not be reorganized during the fast spin-coating process.[36,37]

Confirming the fact that both QDs and dyes are simultaneously positioned in the micellar nanostructure, we subsequently focused on the analysis of FRET in the hybrid system with complementary spectroscopic techniques. Prior to that, a single-layered film of micelles with only R123 in the core or micelles with only QDs in the periphery was prepared as a reference. UV-Vis and fluorescence spectra from reference samples (Figure 4.5) showed a strong spectral overlap between QD emission (blue solid line) centered at 500 nm and dye absorption (green dashed line) at 510 nm. In the steady-state fluorescence from micelles with both dyes in the cores and QDs

in the periphery (pink solid line in Figure 4.3b), QD emission at 500 nm was dramatically quenched while dye emission at 545 nm was enhanced significantly with virtually no shift in the peak position. This indicated an effective energy transfer from the QDs to the dyes in the micellar hybrid. For a comparison, reference fluorescence spectra from micelles containing only QDs (blue dashed line) and micelles containing only R123 (green dashed line) are also included. The excitation wavelength was 442 nm in all cases. FRET was further analyzed by time-resolved fluorescence (TRF) of the QD donor at 500 nm (Figure 4.3c). Multi-exponential fits to the data are included as solid lines to extract some kinetic variables. For micellar films containing only QD donors (blue line), the average lifetime of the donor (τ_D) was 21.8 ns with two decay times of 23.9 ns (87.3 %) and 7.0 ns (12.7 %). In the case of micelles containing both QD donors and dye acceptors (pink line), the average lifetime of QDs (τ_{DA}) was considerably shortened to 4.30 ns with two rate constants of 1.77 ns (50.3 %) and 6.86 ns (49.7 %), which confirmed an efficient FRET in the micellar film. From the average lifetime, the FRET rate (k_{FRET}) was calculated to 0.187 ns^{-1} by the relation $k_{FRET} = 1/\tau_{DA} - 1/\tau_D$ [21] and this value will be discussed later.

Having verified FRET in micellar hybrids, it is important to apply the result to metal NP systems to exploit surface-plasmon-coupled FRET. To this end, Ag NPs stabilized by polyvinylpyrrolidone (10000 g/mol, Sigma-Aldrich) having a 34 nm in diameter (Figure 4.6a) were synthesized as described in the literature.[44] After centrifugation (4000 rpm, 10 min) by 4

times, Ag NPs were redispersed in ethanol at a final concentration of 10 mg ml^{-1}. Then, a film of Ag NPs was fabricated by spin-coating (2000 rpm, 60 sec), the extinction of which showed the well-known plasmon resonance at 437 nm (Figure 4.7). The thickness of the film was about ~ 1.2 μm as obtained from the cross-sectional scanning electron microscopy (SEM) image (Figure 4.6b), but direct visualization of Ag NPs was not possible due to the thick polymer coating on Ag NPs. Intriguingly, the surface of the Ag film was quite smooth as shown in the atomic force microscopy (AFM) image (Figure 4.6c), even if we used Ag NPs of 34 nm in diameter. The rms roughness of the film of the Ag NPs was 0.3 nm. Although the Ag NPs solution was washed several times, polyvinylpyrrolidone was not completely removed from the solution presumably due to its high viscosity. Hence, the residual polymer may flatten the surface morphology of the Ag films in turn reducing the surface area.

Given that the surface of the film of Ag NPs (denoted as NP film hereafter) is atomically flat and the solubility of polyvinylpyrrolidone in toluene is negligible (the solubility parameter of toluene and polyvinylpyrrolidone are 18.2, 25.6 $(J/cm^3)^{1/2}$, respectively),[45] we could spin coat additional single layer of micelles with dyes in the core or QDs in the periphery directly on the NP film. This allowed us to examine how QDs or dyes can interact with Ag NPs in the micellar film. After coating a single-layer of micelles containing only QDs from their mixture, we examined the surface topography by AFM. It should be noted that direct TEM analysis was not possible in this case due to the thick NP film. From AFM, the location of

QDs and micelles can be recognized by their size without chemical analysis as we employed small-sized QDs and large-sized micelles. In Figure 4.8a, hexagonally ordered micelles are surrounded by QDs with a center-to-center distance between micelles of 61 nm. This value was found to be virtually identical to that (59 nm) of the bare substrate. However, a sharp visualization of QDs was hindered in the AFM analysis, which further indicates that QDs are most likely located on the surface of the NP film with an appreciable overlap with the PS corona.

With this structural information, we focused on the NP effect on the fluorescence of QDs. In the steady-state fluorescence (Figure 4.8c) the QD emission at 500 nm on a bare substrate (dashed line) became strongly quenched when the same micellar film was coated on the NP film (solid line). To gain further insights into the NP effect, TRF of QDs was monitored at 500 nm in the absence and presence of NP films. In Figure 4.8c, the blue fitting curve was obtained from micelles with QDs on a bare substrate, which showed an average lifetime of 21.8 ns having two components of 23.9 ns (87.3 %) and 7.0 ns (12.7 %). When the same micellar film was coated on the NP film (gray line), the decay process of QDs became much faster with an average lifetime of 2.57 ns having two decay components of 3.16 ns (77.9 %) and 0.50 ns (22.1 %). In general, the lifetime of fluorophores is inversely proportional to the total decay rate (k_t^0) which is the sum of the radiative decay rate (k_{rad}^0) and the non-radiative decay rate (k_{nr}^0).[21] On the other hand, if fluorophores are placed in the vicinity of metal NPs, surface plasmons of

metal NPs can affect the intrinsic radiative and non-radiative decay rate of fluorophores.[4,6,46-48] Therefore, the shortened lifetime illustrated by a steeper slope in the TRF of QDs indicates that either k_{rad}^{0} or k_{nr}^{0} was increased by the NP film. However, the radiative decay rate cannot be increased in this case as we observed quenched QD emission in Figure 4.8b. Therefore, the shortened lifetime of QDs on the NP film can be attributed to an increased non-radiative decay rate by metal NPs. This quenched QD emission may be comparable to recent study by Mahrt and coworkers.[49] In their paper, they incorporated dye molecules and small Ag NPs (2 – 3 nm) simultaneously into the PVP core of PS-PVP micelles. As a result, the fluorescence of dyes was quenched with a shortened lifetime by the closeness of dyes to NPs, which was explained by non-radiative energy transfer process.

Subsequently, we spin coated micelles containing dyes in the cores on the NP film. AFM image showed a hexagonal array of spherical micelles with a center-to-center distance of 52 nm (Figure 4.8b) similar to those on a bare substrate. However, quite different results were obtained from the fluorescence data in the absence and presence of the NP film. Clearly, the dye emission at 545 nm on a bare substrate (dashed line in Figure 4.8d) was greatly enhanced after coating the same structure on the NP film (solid line). In addition, the peak position was blue-shifted from 545 nm to 537 nm. Therefore, one can speculate that the NPs exerted a different effect on QDs and dyes in micellar films. TRFs of dyes on a bare substrate (green line) and on the NP film (gray line) were also monitored at 540 nm (Figure 4.8f). The decay profile of dyes on a bare substrate showed an average lifetime of 1.96

ns with two decay components of 2.70 ns (64.2 %) and 0.62 ns (35.8 %). Since the dye molecules in a dilute ethanol solution showed a single-exponential decay with a lifetime of 3.89 ns (Figure 4.9), the short component of 0.62 ns can be attributed to some agglomeration of dye molecules in the PVP cores. When the same micelles were coated on the NP film, the average lifetime of dyes was increased to 3.17 ns with two decay components of 3.42 ns (90.7 %) and 0.75 ns (9.3 %). This increased lifetime apparently contradicts the general NP effect discussed before. In order to enhance dye emission, the intrinsic radiative decay rate of dyes has to be increased and therefore the lifetime of the dyes has to be reduced. The abnormality observed here can be attributed to the dye agglomeration in the micellar core. Note, such an agglomeration usually red-shifts the fluorescence peak position and also reduces the lifetime by a self-quenching mechanism.[21] Therefore, the NP effect on the dye molecules can be understood as reduction of the self-quenching process. This feature can explain a number of observations; (a) an increased lifetime of the dyes along with a reduced amplitude of the short time component in TRF and (b) the blue shifted steady-state fluorescence of dyes on the NP films. As we noted that this kind of NP effect has not been reported yet, a systematic study of the NP effect on the self-quenching process will follow in future work.

Based on the information collected so far, we decided to coat a single-layered film of micelles with both dyes in a core and QDs in the periphery on the NP film (denoted by micelles with QD/dye/NP hereafter). It is important to recall that the same micellar film on a bare substrate showed efficient

FRET from QD donors to dye acceptors in Figure 4.3. In stark contrast, when the same micelles containing both dyes and QDs were applied to the NP film, the fluorescence spectrum from QDs at 500 nm and dyes at 545 nm basically remained unaltered (pink line in Figure 4.10a) compared to the fluorescence spectra from micelles containing only QDs (blue line) and micelles containing only dyes (green line) on the NP film, i.e., the quenched QD emission and enhanced dye emission on the NPs film discussed in Figure 4.8. The slight decrease in the dye emission at 545 nm can be attributed to the reduced number of micelles because QDs replaced some of the micelles in the mixed film. Furthermore, the average lifetime and fluorescence time components of the QD donors were greatly maintained, even in the presence of dye acceptors when they were placed on the NP film (see TRF in Figure 4.10b). In other words, *Ag NPs completely switched off FRET from QDs to dyes in a micellar hybrid*. From the decay profile of the QD donors from micelles with QD/dye/NP (gray line) an average lifetime of 2.84 ns with two decay times of 3.33 ns (81.9 %) and 0.64 ns (18.1 %) was extracted. These values were nearly identical to those obtained from micelles with only QDs on NP films (pink line) which have an average lifetime of 2.57 ns with two decay times of 3.16 ns (77.9 %) and 0.50 ns (22.1 %). The inhibited FRET by Ag NPs was further confirmed by comparing TRF spectra of dye acceptors at 540 nm. When micelles with QDs and dyes were coated on a bare substrate, time-dependent intensity of dye fluorescence was increased with a rise component of 0.59 ns (Figure 4.11a). At first, we compared TRF spectra of dye acceptors on a bare substrate in the presence (pink line) and absence (green line) of QD

donors (Figure 4.11a). The monitoring wavelength was 540 nm. It would be instructive to recall that the lifetime of QD donors was substantially shortened in the presence of dye acceptors (Figure 4.3c). Alternatively, the efficient FRET on a bare substrate was further confirmed by time-dependent rise of dye fluorescence in the presence of QDs. On the other hands, when the same micellar film was coated on the NP film, TRF spectrum of dye acceptors was remained unchanged by the presence of QDs (Figure 4.11b). Therefore, the same conclusion can be reached that Ag NPs completely inhibited FRET from QDs to dyes. Time components after fitting the TRF spectra with multi-exponential equation were summarized in Table 4.1.

However, when the same micellar film was coated on the NP film, any rise component was not detected in the TRF spectrum (Figure 4.11b). Since the rise component is an indicative of additional excitation of dyes by energy transfer from QDs, it further confirms that FRET was inhibited by Ag NPs in the micellar hybrid.

How can FRET in micellar films be switched off by metal NPs? In order to answer this question, one has to consider all the near-filed interactions among QDs, dyes, and Ag NPs in their hybrid structures. At the beginning, it would be instructive to discuss general aspects of NP effects on nearby fluorophores and to quantitatively analyze the spectroscopic results in Figure 4.8 and 4.10 according to recent kinetic models.[4,6,46-48,50,51] In general, the emission rate of fluorophores can be described as $\gamma_{exc}^{0}Q^{0}$, where γ_{exc}^{0} is the excitation rate and Q^{0} is quantum yield of fluorophores. Metal NPs can

potentially affect the intrinsic excitation rate and quantum yield with the following processes. In the micellar hybrid of Figure 4.10, as the extinction spectrum of NP film is centered at 437 nm, the incident light (442 nm) excites the surface plasmon of Ag NPs, which subsequently creates a strong electromagnetic field. Thus, the excitation rate of QDs or dyes in the vicinity of Ag NPs can be enhanced. In addition, the excited fluorophores further induce an electron oscillation in the Ag NPs and lead to resonance between fluorophores and Ag NPs. This coupling effect can affect the quantum yield of fluorophores by modifying the intrinsic radiative (k_{rad}^{0}) and non-radiative decay (k_{nr}^{0}) rate with k_{rad} and k_{nr}, respectively. At the same time, the excited state energy of fluorophores can be transferred to metal NPs and then dissipated as heat. This non-radiative energy transfer to metal NPs is inversely proportional to the 4th power of the distance between the fluorophores and the surface of metal NPs and can be adequately described by the empirical nanometal surface energy transfer (NSET) mechanism.[50,51] Perceiving that QDs are stabilized by oleic acid and dyes are located in the PVP cores that are surrounded by PS coronas, the separation of QDs and dyes from the surface of Ag NPs can be evaluated from the thickness of stabilizers or PS coronas. Within this structural picture, the NSET efficiency was calculated to 0.99 for QDs and 0.08 for dyes in the micellar films, respectively.

The efficiency (E_{NSET}) of nanometal surface energy transfer (NSET) mechanism can be described as[50,51]

$$E_{NSET} = 1 - \frac{1}{1 + (d_0 / d)^4} \quad \text{---------- Eq. (4.1)}$$

where d_0 is the distance at which 50 % quenching occurs, and d is the distance between fluorophores and the surface of metal NPs. Therefore, Eq. (4.1) gives physical insight on NSET process in micellar systems. d_0 can be calculated as[50,51]

$$d_0 = \left(\frac{0.225 c^3 Q^0}{\omega_{donor}^2 \omega_F k_F} \right)^{1/4} \quad \text{---------- Eq. (4.2)}$$

where c is the speed of light (3×10^{10} cm s^{-1}), Q^0 is the quantum yield of fluorophores (QDs = 0.83, dyes = 0.45), ω_{donor} is the angular frequency for the donor (QDs = 3.76×10^{15} s^{-1}, dyes = 3.46×10^{15} s^{-1}), ω_F is the angular frequency for bulk silver (8.3×10^{15} s^{-1}), and k_F is the Fermi wavevector for bulk silver (1.2×10^8 cm^{-1}).[50,51] The values of d_0 were calculated as 77 and 69 Å for QDs and dyes, respectively.

In order to calculate the NSET efficiency, the surface of Ag NPs was assumed as the surface of the NP film. Since QDs are stabilized by oleic acid and dyes are located in the PVP cores that are surrounded by PS coronas, the separation of QDs or dyes from surface of NP film can be regarded as the thickness of stabilizers or PS coronas. Therefore, the values of d for QDs and dyes can be determined as the half of the spacing between QDs and PVP cores themselves in the TEM images (Figure 4.1 and 4.3a), and were evaluated as 1.4 nm and 12.5 nm, respectively. By inserting those values into Eq. (4.1), the

NSET efficiency was evaluated as 0.99 for QDs and 0.08 for dyes, respectively. The proximity of the QDs to the NP film facilitated the NSET process, while such a process is restricted to dyes in the PVP core due to the large separation by the PS coronas.

By combining aforementioned near-field interactions, the overall NP effect on the nearby fluorophores can be expressed as the total enhancement factor (E) which is a product of the excitation enhancement factor (E_{exc}) and the emission enhancement factor (E_{ems}) originating from the modified excitation rate and the decay rate by metal NPs.[4,6,13,46-48] Experimentally, the total enhancement factor can be determined from the intensity ratio of the steady-state fluorescence from bare substrates and from the NP film in Figure 4.8. Then, the total enhancement factor (E) can be further resolved into the excitation enhancement factor (E_{exc}) and the emission enhancement factor (E_{ems}) by the TRF spectra in Figure 4.8. By combining these enhancement factors with the lifetime information, all the decay rates (k_{rad}^0, k_{nr}^0, k_{rad}, k_{nr}, and k_{NSET}) can be determined, which are summarized in the Table 4.2.

In general, the emission rate of fluorophores in the absence of metal NPs can be written as $\gamma_{exc}^0 Q^0$, where γ_{exc}^0 is the excitation rate and Q^0 is quantum yield. The quantum yield is the probability of a photon emission from excited fluorophores by radiative decay process and is described as $Q^0 = k_{rad}^0/(k_{rad}^0 + k_{nr}^0) = k_{rad}^0/k_t^0$, where k_{rad}^0, k_{nr}^0, and k_t^0 is the radiative, non-radiative and total decay rate of fluorophores, respectively. Metal NPs

can potentially affect the excitation rate and all the decay processes. Therefore, the total enhancement factor (E) can be defined by the ratio of emission rate of fluorophores with metal NPs to that without metal NPs[13,14]

$$E = \frac{\gamma_{exc} Q}{\gamma_{exc}^0 Q^0} = \frac{\gamma_{exc}}{\gamma_{exc}^0} \frac{k_{rad}}{k_{rad}^0} \frac{k_t^0}{k_t} = E_{exc} E_{ems} \qquad \text{---------- Eq. (4.3)}$$
$$k_t^0 = k_{rad}^0 + k_{nr}^0, \qquad k_t = k_{rad} + k_{nr} + k_{NSET}$$

where γ_{exc} , Q , k_{rad} , k_{nr} , and k_t are the modified excitation rate, quantum yield, radiative decay rate, non-radiative decay rate, and total decay rate of fluorophores by metal NPs, respectively. The excitation enhancement and emission enhancement factors were defined as $E_{exc} = \gamma_{exc} / \gamma_{exc}^0$ and $E_{ems} = k_{rad} k_t^0 / k_{rad}^0 k_t$, respectively. k_{NSET} is the rate of non-radiative energy transfer to metal NPs.

To extract kinetic variables from spectroscopic results, we adapted recent models developed in the reference.[13,14] We first determined total enhancement factor (E) from the intensity ratio of steady-state fluorescence from bare substrate (I^0) and the NP film (I) by $E = I / I^0$. In the case of quenched QD emission, we obtained the value of E = 0.16 from Figure 4.8c. Total radiative decay rate in the absence of metal NPs (k_t^0) were obtained by $k_t^0 = k_{rad}^0 + k_{nr}^0 = 1/\tau^0$. As the average lifetime of QDs on a bare substrate (τ^0) was 21.8 ns, it corresponds to k_t^0 = 0.046 ns^{-1}. The intrinsic radiative decay (k_{rad}^0) and non-radiative decay (k_{nr}^0) rate in the absence of metal NPs can be determined from

$$Q^0 = \frac{k_{rad}^0}{k_{rad}^0 + k_{nr}^0} \text{ ---------- Eq. (4.4)}$$

where Q^0 is the quantum yield of QDs in the absence of metal NPs and was calculated as 0.83 by referencing dilute ethanol solution of coumarin 6. The calculated k_{rad}^0 and k_{nr}^0 were 0.038 ns^{-1} and 0.008 ns^{-1}.

The emission enhancement factor (E_{ems}) can be evaluated from fluorescence intensity obtained at t = 0 with a relation of [13,14]

$$E_{ems} = \frac{k_{rad}}{k_{rad}^0}\frac{k_t^0}{k_t} \qquad \frac{k_{rad}}{k_{rad}^0} = \frac{I(t=0)}{I^0(t=0)} \text{ ---------- Eq. (4.5)}$$

where $I^0(t=0)$ and $I(t=0)$ is the initial photon counts at t = 0 from TRF in the absence and presence of metal NPs. The omission of superscript always indicates decay processes were affected by metal NPs. It has been reported that the initial fluorescence intensity at t = 0 is proportional to the radiative decay rate.[13,14] While we used normalized TRF results in the main text for a better comparison, the raw data in a linear scale on Y axis were shown in Figure 4.12a. The ratio of k_{rad}/k_{rad}^0 was obtained as 0.239. Since k_t (total radiative decay rate of QDs on the NP film) is an inverse of average lifetime ($k_t = 1/\tau$ and τ = 2.57 ns^{-1}), E_{ems} was calculated as 0.028. The excitation enhancement factor (E_{exc}) was directly obtained from $E = E_{exc}E_{ems}$ and was 5.7.

To calculate non-radiative energy transfer to metal NPs (k_{NSET}), we included this term into the total decay rate as $k_t = k_{rad} + k_{nr} + k_{NSET}$. Here,

non-radiative decay rate (k_{nr}) of QDs can be assumed as (k^0_{nr}) as any quenching effect by metal NPs can be attributed to non-radiative energy transfer that were already included as k_{NSET}.[13,14,50,51] Since all the other variables were determined, the value of k_{NSET} was evaluated as 0.373 ns^{-1}.

Therefore, one can see that the excitation rate of QDs was significantly increased by the field enhancement effect of the NP film (E_{exc} = 5.7), because QDs are slightly separated from the NP film by oleic acid. However, E_{ems} was considerably decreased due to the NSET process which is much faster (k_{NSET} = 0.373 ns^{-1}) than all the other decay processes. The combined effect is the quenched QD emission as we discussed in Figure 4.8. All those values were summarized in Table 4.2.

The same procedure was used to extract kinetic variables for dyes molecules. We first obtained total enhancement factor of 6.8 from the steady-state fluorescence (Figure 4.8e). Then k^0_{rad} and k^0_{nr} were calculated as 0.230 ns^{-1} and 0.280 ns^{-1}. The quantum yield of dyes in the absence of metal NPs was estimated as 0.45 by referencing dilute ethanol solution of the same dyes. Then, the ratio of k_{rad} / k^0_{rad} was obtained as 1.30 from the initial fluorescence intensity at t = 0 (Figure 4.12b). From this, the emission enhancement factor (E_{ems}) was calculated as 2.11. Then, excitation enhancement factor (E_{exc}) was obtained as 3.2 by the relation of $E = E_{exc}E_{ems}$.

Excitation enhancement factor of dye molecules (E_{exc} = 3.2) is much less than that of QDs (E_{exc} = 5.7) because dyes are alienated from the surface of the NP film by the thicker PS coronas. However, emission enhancement factor in this case is still appreciable (E_{ems} = 2.11) as the NSET process for dye is restricted here, so the overall NP effect can be understood as an enhanced emission as in Figure 4.8d and 4.8f.

The main difference for analyzing spectroscopic results from dye molecules was that we excluded the k_{NSET} term in the total decay rate because NSET efficiency for dyes was quite negligible as already discussed. So, total decay process was equated as $k_t = k_{rad} + k_{nr}$ in the presence of metal NPs. Also note, non-radiative decay rate (k_{nr}) of dyes here cannot be assumed as (k_{nr}^0) in this case because of dye agglomeration in the PVP cores. With this consideration, k_{rad} and k_{nr} were calculated as 0.299 and 0.016 ns^{-1}. The non-radiative decay rate was reduced from k_{nr}^0 = 2.80 ns^{-1} to k_{nr} = 0.016 ns^{-1} by the NP effect, indicating relieved self-quenching process. All those values were summarized in Table 4.2.

All these considerations can provide a rationale on the inhibited FRET presented in Figure 4.10a and 4.10b. At the beginning, we considered all the near-field interactions among QDs, dyes, and NPs as depicted in Figure 4.10c. In the schematics, FRET, NSET, and excitation/emission enhancement factors were represented by green, blue, and red arrows, respectively. However, the excitation enhancement factor (E_{exc}) cannot change the intrinsic radiative and

non-radiative decay processes that are occurring after excitation and so this factor can be excluded in the discussion of inhibited FRET. The emission enhancement factor (E_{ems}) indeed altered the intrinsic decay processes and this effect was taken into consideration as k_{rad} and k_{nr}. Furthermore, the NSET process from dyes to metal NPs can be neglected by the thick PS coronas as we have already discussed. Therefore, after excluding the aforementioned interactions, the question on how the FRET from QDs to dyes was inhibited by metal NPs can be rephrased into which decay process is the more favorable one for the excited QDs. In other words, there is a competition among radiative decay, non-radiative decay, FRET and NSET processes for the excited QDs in the hybrid structure. Since the rate constants of radiative (k_{rad}), non-radiative (k_{nr}), NSET (k_{NSET}) processes in the presence of metal NPs were calculated as 0.009, 0.008, and 0.373 ns^{-1} (Table 4.2), respectively, and the FRET rate (k_{FRET}) was evaluated as 0.187 ns^{-1} in Figure 4.3, one can see the non-radiative energy transfer to Ag NPs (NSET) is much faster than all the other decay processes. All together, these features allow the donor (QDs)-acceptor (dyes) interaction in FRET to be turned off by metal NPs in the micellar hybrid.

Considering the fastest NSET process was created by the closeness of QDs to the NP film, it can be also blocked by introducing a spacer layer that alienates QDs from the NP film. To testify this idea, a spacer layer of poly(2-vinlypridine) (P2VP) homopolymer having 15.5 nm in a thickness was inserted between the NP film and the micellar film. In such a hybrid structure,

it turns out that NSET process becomes insignificant and FRET becomes the fastest decay processes for the excited QDs. As a result, FRET from QDs to dyes can be retrieved even in the presence of the NP film (see Figure 4.13).

To better understand the inhibited FRET by metal NPs, we inserted a spacer layer of poly(2-vinly prindine) (P2VP) homopolymer (14000 g/mol, Polymer Source, Inc.) between the NP film and the micellar film. To this end, 1, 4-dioxane solution of P2VP was prepared (2.0 wt%) and then spin-coated on the NP film by 2000 rpm and 60 sec (this structure will be denoted as P2VP/NP film). The thickness of the P2VP spacer layer was determined as 15.5 nm by ellipsometry.

To examine the effect of a P2VP spacer, a single-layered film of micelles containing only QDs was spin-coated on the P2VP/NP film. Then, the steady-state fluorescence of QDs on the P2VP/NP film (solid line) and bare substrate (dashed line) were compared in Figure 4.13a. Noticeably, QD emission on the P2VP/NP film was greatly maintained after introducing a spacer layer of P2VP, which is a sharp contrast to the strongly quenched QD emission on the NP film (Figure 4.8c in the main text). The substantial increase of QD-NP distance by P2VP layer can be responsible for this observation. From the thickness of P2VP layer, the efficiency of NSET was calculated as 0.04 from Eq. (4.1). In addition, a single-layered film of micelles containing only dyes in the core was spin-coated on the P2VP/NP film. In the steady-state fluorescence of in Figure 4.13b, dye emission on the P2VP/NP film (solid line) was basically the same compared to the dye emission on a bare substrate (dashed line). From this result, the effect of a P2VP spacer can

be understood as blockade for the NP-fluorophore interactions as the local field around metal NPs rapidly decreases with distance between metal NPs and fluorophores.

With the aforementioned results, we further spin-coated micellar film containing both dyes in the core and QDs in the periphery on the P2VP/NP film. In Figure 4.13c, the dashed line was obtained from a micellar film with QDs and dyes on a bare substrate and reflects the efficient FRET from QDs to dyes as discussed in Figure 4.3b (main text). Strikingly, the spectrum from micelles with QDs and dyes on the P2VP/NP film (solid line) is nearly identical to the same micelles on a bare substrate. Since we clearly observed the efficient FRET on a bare substrate, it indicates that the inhibited FRET on the NP film was retrieved by inserting a P2VP spacer layer. In this case, FRET rate (k_{FRET}) becomes the fastest decay processes for the excited QDs because NSET process from QDs to NPs can be excluded in the presence of a P2VP layer.

4.4. Conclusions

Our results strongly suggest that near-field interactions among QDs, dyes, and metal NPs can be engineered by nanoscale organization. Both the radiative and non-radiative decay processes of fluorophores were controlled in the vicinity of metal NPs to induce either enhanced or quenched fluorescence.

In particular, FRET from QDs to dyes was inhibited by the presence of metal NPs, which was explained by the fastest NSET decay process by the closeness of QDs and metal NPs. In addition, after introducing a spacer layer of P2VP homopolymer, the inhibited FRET can be retrieved even in the presence of the NP film. One can assess the prospects of this result from a perspective of turning on and off FRET by NP-fluorophore interactions. In this regard, metal NPs can be considered as an optical switch, which can potentially control FRET in optoelectric devices or in biological systems such as fluorophore-labeled proteins. Overall, a number of features discussed in this study can stimulate future interests on plasmonic effects on hybrid systems and also represents a new approach for engineering mutual interactions between dissimilar functionalities in the framework of block copolymers. Systematic tuning of the extinction spectrum of metal NPs may help a better understanding of the underling physical process and can be suggested as a future direction.

4.5. References

[1] Z. Nie, A. Petukhova, E. Kumacheva, *Nat*. *Nanotechnol*. **2010**, *5*, 15.

[2] J. Lee, P. Hernandez, J. Lee, A. O. Govorov, N. A. Kotov, *Nat*. *Mater*. **2007**, *6*, 291.

[3] L. Novotny, N. V. Hulst, *Nat. Photonics* **2011**, *5*, 83.

[4] V. Giannini, A. I. Fernández-Domíguez, S. C. Heck, S. A. Maier, *Chem. Rev.* **2011**, *111*, 3888.

[5] A. Kinkhabwala, Z. Yu, S. Fan, Y. Avlasevich, K. Müllen, W. E. Moerner, *Nat. Photonics* **2009**, *3*, 654.

[6] J. R. Lakowicz, K. Ray, M. Chowdhury, H. Szmacinski, Y. Fu, J. Zhang, K. Nowaczyk, *Analyst* **2008**, *133*, 1308.

[7] M. Rycenga, C. M. Cobley, J. Zeng, W. Li, C. H. Moran, Q. Zhang, D. Qin, Y. Xia, *Chem. Rev*. **2011**, *111*, 3669.

[8] R. Bardhan, N. K. Grady, J. R. Cole, A. Joshi, N. J. Halas, *Acs Nano* **2009**, *3*, 744.

[9] F. Tam, G. P. Goodrich, B. R. Johnson, N. J. Halas, *Nano Lett.* **2007**, *7*, 496.

[10] D. Ratchford, F. Shafiei, S. Kim, S. K. Gray, X. Li, *Nano Lett*. **2011**, *11*, 1049.

[11] K. Ray, R, Badugu, J. R. Lakowicz, *Chem*. *Mater*. **2007**, *19*, 5902.

[12] G. Schneider, G. Decher, N. Nerambourg, R. Praho, M. H. V. Werts, M. Blanchard-Desce, *Nano Lett*. **2006**, *6*, 530.

[13] K. Munechika, Y. Chen, A. F. Tillack, A. P. Kulkarni, I. J. L. Plante, A. M. Munro, D. S. Ginger, *Nano Lett*. **2010**, *10*, 2598.

[14] Y. Chem, K. Munechika, D. S. Ginger, *Nano Lett*. **2007**, *7*, 690.

[15] Y. Wang, B. Liu, A. Mikhailovsky, G. C. Bazan, *Adv. Mater*. **2010**, *22*, 656.

[16] M. A. Noginovl, G. Zhul, A. M. Belgravel, R. Bakker, V. M. Shalaev, E. E. Narimanov, S. Stoutl, E. Herz, T. Suteewong, U. Wiesner, *Nature* **2009**, *460*, 1110.

[17] T. H. Kim, K. S. Cho, E. K. Lee, S. J. Lee, J. Chae, J. W. Kim, D. H. Kim, J. Y. Kwon, G. Amaratunga, S. Y. Lee, *et al*. *Nat. Photonics* **2011**, *5*, 176.

[18] M. K. Kwon, J. Y. Kim, B. H. Kim, I. K. Park, C. Y. Cho, C. C. Byeon, S. J. Park, *Adv. Mater*. **2008**, *20*, 1253.

[19] E. Ozbay, *Science* **2006**, *311*, 189.

[20] K. E. Sapsford, L. Berti, I. L. Medintz, *Angew. Chem. Int. Ed*. **2006**, *45*, 4562.

[21] J. R. Lakowicz, *Principles of Fluorescence Spectroscopy*, 3rd ed.; Kluwer Academic/Plenum Publishers: New York, **2006**, pp 443-475.

[22] S. I. Yoo, S. H. Bae, K. S. Kim, B. H. Sohn, *Soft Matter* **2009**, *5*, 2990.

[23] F. Reil, U. Hohenester, J. R. Krenn, A. Leitner, *Nano Lett.* **2008**, *12*, 4128.

[24] I. L. Medintz, H. T. Uyeda, E. R. Goldman, H. Mattoussi, *Nat. Mater*. **2005**, *4*, 435.

[25] E. A. Jares-Erijman, T. M. Jovin, *Nat. Biotechnol.* **2003**, *21*, 1387.

[26] M. Lunz, V. A. Gerard, Y. K. Gun'ko, V. Lesnyak, N. Gaponik, A. S. Susha, A. L. Rogach, A. L. Bradley, *Nano Lett.* **2011**, *11*, 3341.

[27] M. Lessard-Viger, M. Rioux, L. Rainville, D. Boudreau, *Nano Lett*. **2009**, *9*, 3066.

[28] J. Zhang, Y. Fu, M. H. Chowhury, J. R. Lakowicz, *J. Phys. Chem. C* **2007**, *111*, 11784.

[29] R. P. Van Duyne, *Science* **2004**, *306*, 985.

[30] M. Achermann, M. A. Petruska, D. D. Koleske, M. H. Crawford, V. I. Klimov, *Nano Lett*. **2006**, *6*, 1396.

[31] M. Achermann, M. A. Petruska, S. Kos, D. L. Smith, D. D. Koleske, V. I. Klimov, *Nature* **2004**, *429*, 642.

[32] S. I. Yoo, J. H. Kwon, B. H. Sohn, *J. Mater. Chem.* **2007**, *17*, 2969.

[33] M. Aizawa, J. M. Buriak, *Chem. Mater*. **2007**, *19*, 5090.

[34] R. Glass, R. M. Möller, J. P. Spatz, *Nanotechnology* **2003**, *14*, 1153.

[35] G. Rainò, T. Stöferle, C. Park, H. C. Kim, I. J. Chin, R. D. Miller, R. F. Mahrt, *Adv. Mater*. **2010**, *22*, 3681.

[36] S. I. Yoo, J. H. Lee, B. H. Sohn, I. Eom, T. Joo, S. J. An, G. -C. Yi, *Adv. Funct. Mater*. 2**008**, *18*, 2984.

[37] S. I. Yoo, S. J. An, G. H. Choi, K. S. Kim, G.-C. Yi, W. C. Zin, J. C. Jung, B. H. Sohn, *Adv. Mater*. **2007**, *19*, 1594.

[38] H. Acharya, J. Sung, B. H. Sohn, D. H. Kim, K. Tamada, C. Park, *Chem. Mater*. **2009**, *21*, 4248.

[39] S. H. Bae, S. I. Yoo, W. K. Bae, S. Lee, J. K. Lee, B. H. Sohn, *Chem. Mater*. **2008**, *20*, 4185.

[40] B. H. Sohn, J. M. Choi, S. I. Yoo, S. H. Yoon, W. -C Zin, J. C. Jung, M. Kanehara, T. Hirata, T. Teranishi, *J. Am. Chem. Soc*. **2003**, *125*, 6368.

[41] T. Lohmueller, E. Bock, J. P. Spatz, *Adv. Mater.* **2008**, *20*, 2297.

[42] S. Förster, M. Antonietti, *Adv. Mater*. **1998**, *10*, 195.

[43] a) W. K. Bae, J. Kwak, J. W. Park, K. Char, K. C. Lee, S. Lee, *Adv. Mater*. **2009**, *21*, 1690; b) G. Moad, Y. K. Chong, A. Postma, E. Rizzardo, S. H. Thang, *Polymer* **2005**, *46*, 8458.

[44] P.-Y. Silvert, R. Herrer-Urbina, N. Duvauchelle, V. Vijayakrishnan, K. Tekaia-Elhsissen, *J. Mater. Chem.* **1996**, *6*, 573.

[45] J. Brandrup, E. H. Immergut, E. A. Grulke, Eds.; *Polymer Handbook*, 4th ed.; Wiley-Interscience: New York, **1999**.

[46] A. O. Govorov, G. W. Bryant, W. Zhang, T. Skeini, J. Lee, N. A. Kotov, J. M. Slocik, R. R. Naik, *Nano Lett.* **2006**, *6*, 984.

[47] E. Dulkeith, M. Ringler, T. A. Klar, J. Feldmann, *Nano Lett*. **2005**, *5*, 585.

[48] E. Dulkeith, A. C. Morteani, T. Niedereichholz, T. A. Klar, J. Feldmann, S. A. Levi, F. C. J. M. van Veggel, D. N. Reinhoudt, M. Möller, D. I. Gittins, *Phys. Rev. Lett*. **2002**, *89*, 203002.

[49] G. Rainò, T. Stöferle, C. Park, H.-C. Kim, T. Topuria, P. M. Rice, I.-J. Chin, R. D. Miller, R. F. Mahrt, *ACS Nano* **2011**, *5*, 3536.

[50] a) S. Saraswat, A. Desireddy, D. Zheng, L. Guo, H. P. Lu, T. P. Bigioni, D. Isailovic, *J. Phys. Chem. C* **2011**, *115*, 17587; b) M. P. Singh, G. F. Strouse, *J. Am. Chem. Soc*. **2010**, *132*, 9383.

[51] T. L. Jennings, M. P. Singh, G. F. Strouse, *J. Am. Chem. Soc*. **2006**, *128*, 5462.

[52] D. Soujon, K. Becker, A. L. Rogach, J. Feldman, H. Weller, D. V. Talapin, J. M. Lupton, *J. Phys. Chem. C*. **2007**, *111*, 11511.

[53] F. C. De Schryver, T. Vosch, M. Cotlet, M. Van Der Auweraer, K. Müllen, J. Hofkens, *Acc. Chem. Res*. **2005**, *38*, 514.

[54] G. Moad, Y. K. Chong, Postma, A.; Rizzardo, E.; Thang S. H. Advances in RAFT Polymerization: The Synthesis of Polymers with Defined End-Groups. *Polymer* **2005**, *46*, 8458-8468.

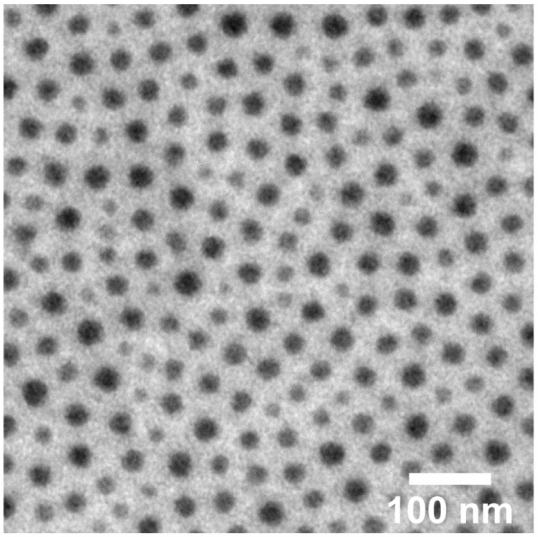

Figure 4.1. TEM image of a single-layered film of PS-PVP micelles.

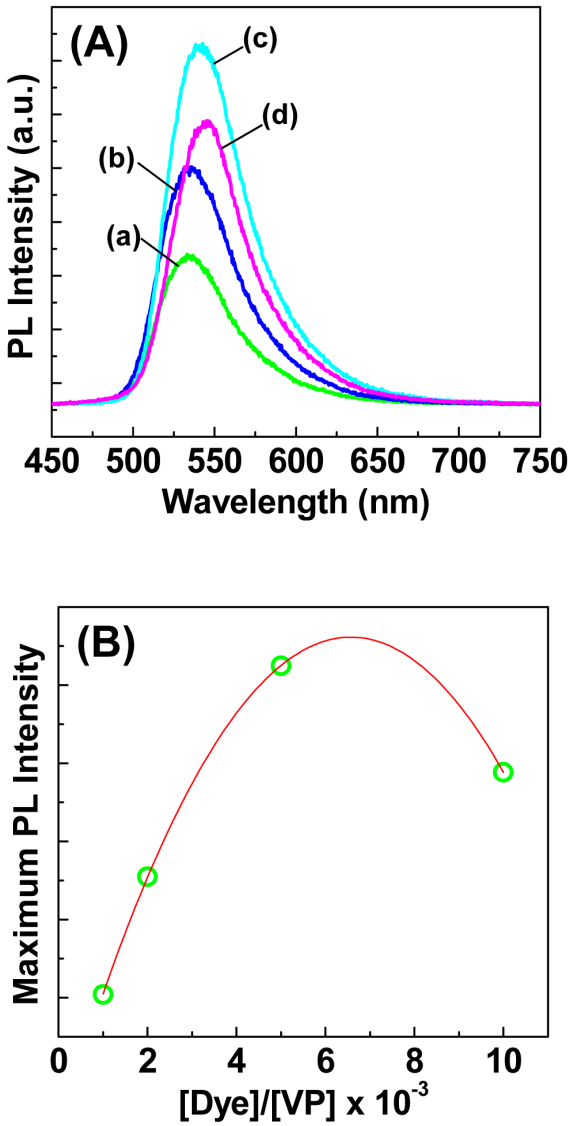

Figure 4.2. Steady-state fluorescence (A) and maximum fluorescence intensity (B) from single-layered films of PS-PVP micelles with dyes in the PVP cores. The molar ratio of [R123]/[VP] was adjusted as 0.001 (a), 0.002 (b), 0.005 (c), and 0.01 (d).

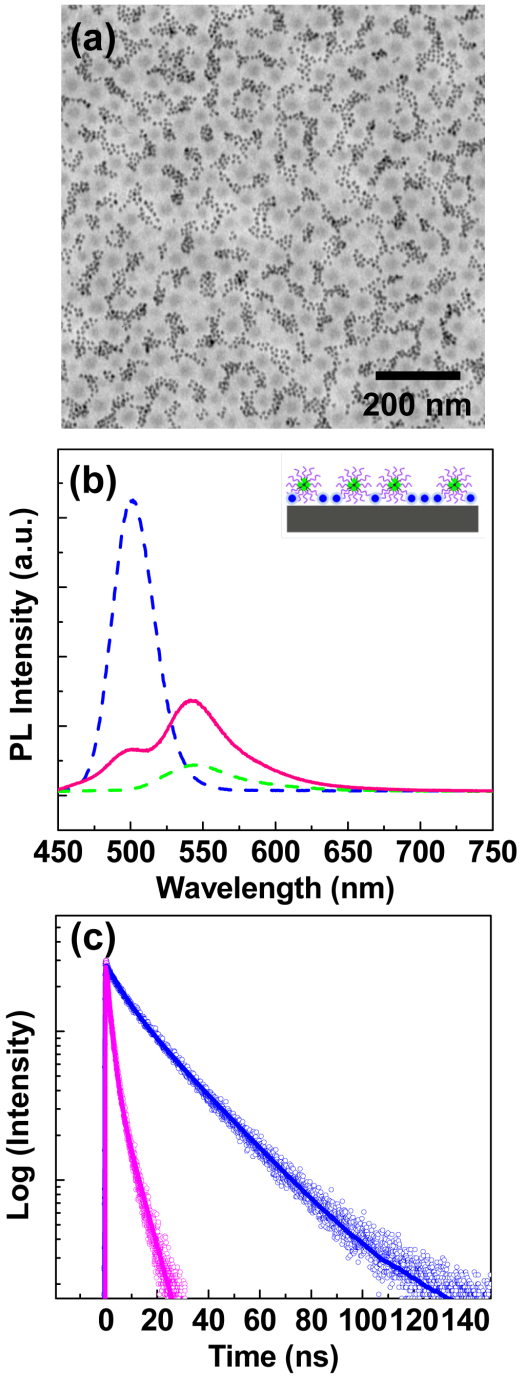

Figure 4.3. (a) TEM image of a single-layered film of PS-PVP micelles with dyes in the cores and QDs in the periphery. (b) Steady-state fluorescence spectra from micellar film with only QDs (blue dashed), with only dyes

(green dashed), and with QDs and dyes (pink solid). (c) Time-resolved fluorescence monitored at 500 nm from micellar film with only QDs (blue) and with QDs and dyes (pink).

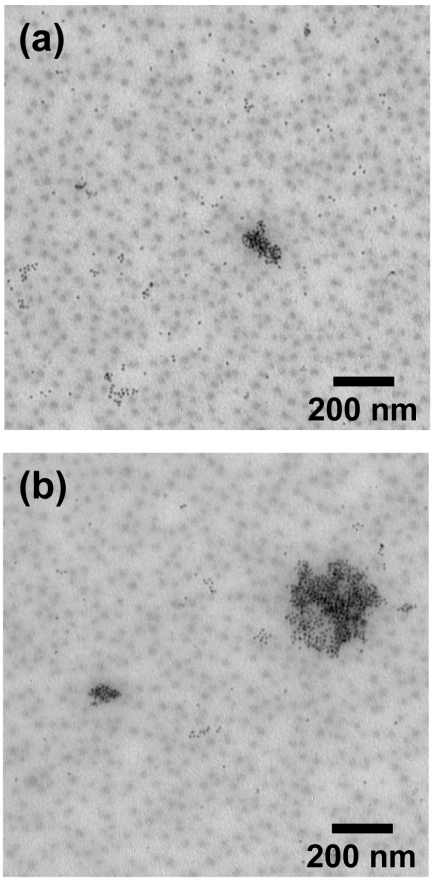

Figure 4.4. TEM images of a single-layered film of PS-PVP micelles containing PS-coated QDs. (a) and (b) were collected from different areas.

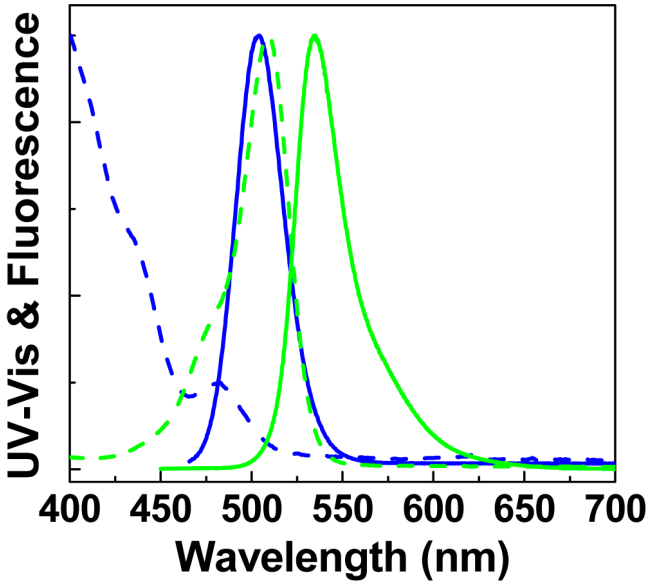

Figure 4.5. Normalized UV-Vis (dashed) and fluorescence (solid) spectra of micelles with QDs (blue) and with dyes (green).

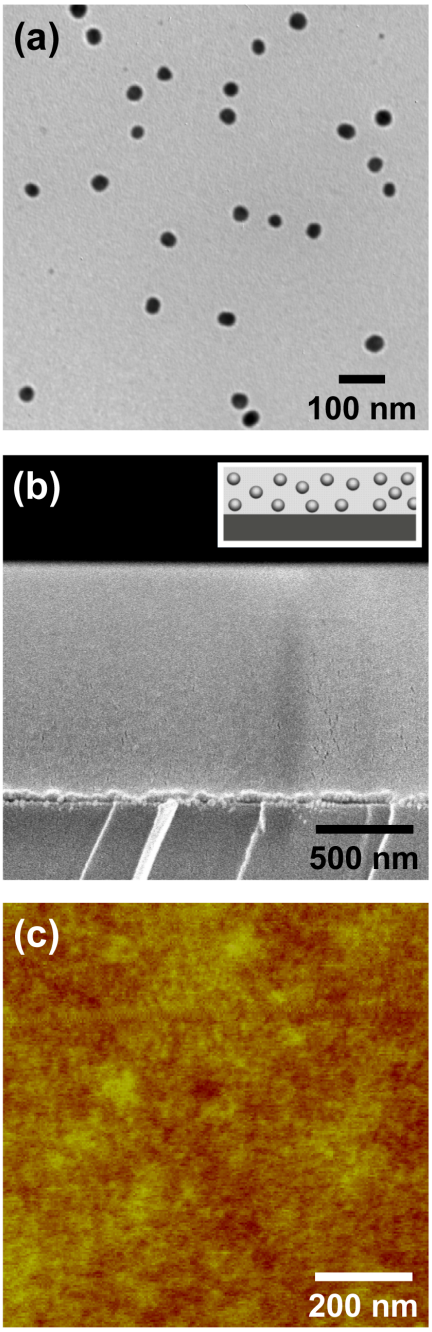

Figure 4.6. TEM image (a) of Ag NPs and cross-sectional SEM image (b) and AFM image (c) of thin films of Ag NPs.

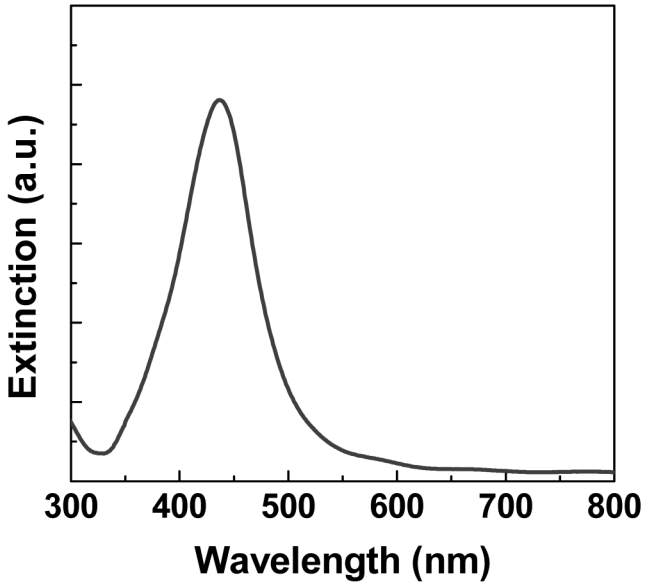

Figure 4.7. UV-Vis spectrum of thin film of Ag NPs.

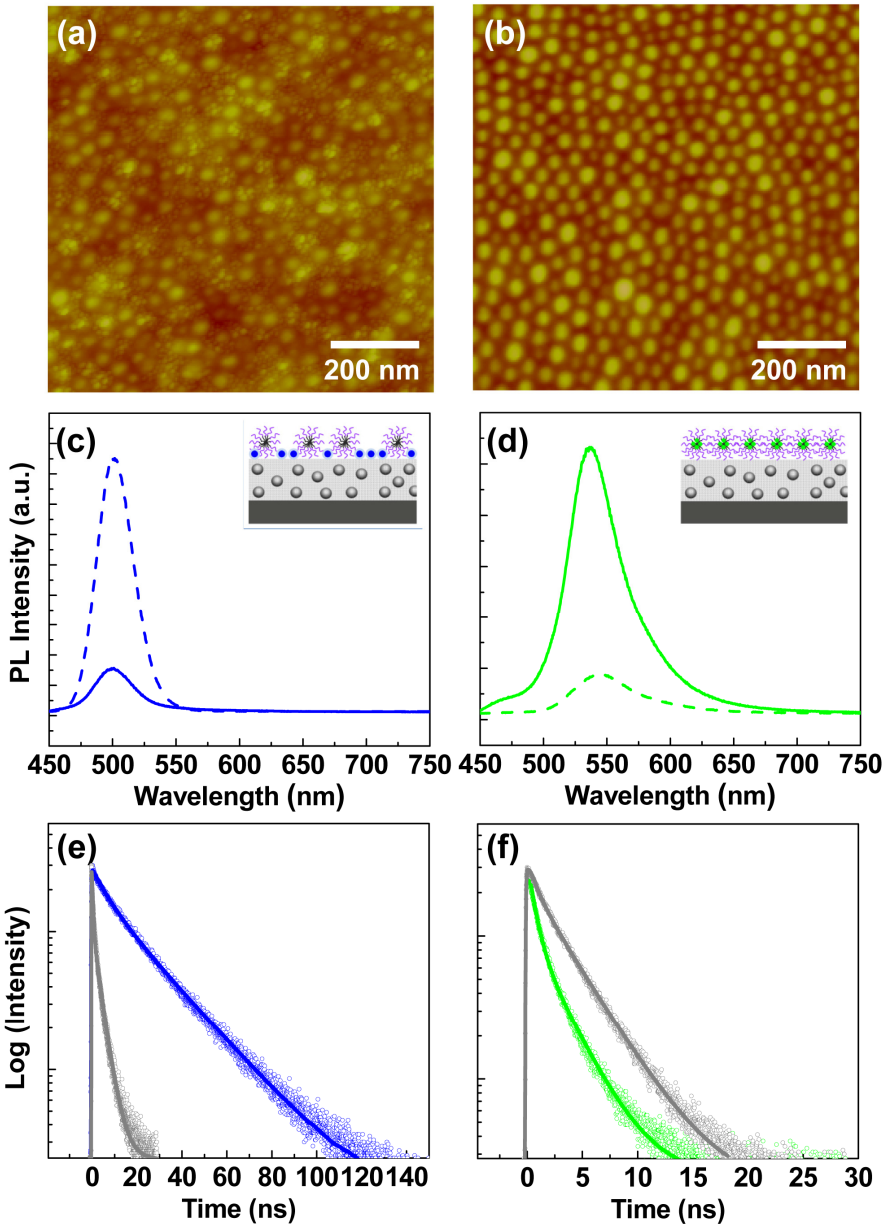

Figure 4.8. (a, b) AFM images of a single-layered film of PS-PVP micelles with QDs in the periphery (a) and with dyes in the core (b) on the NP film. (c, d) Steady-state fluorescence spectra from micellar film with QDs in the periphery (c) and with dyes in the core (d). (e, f) Time-resolved fluorescence spectra from micellar film with QDs in the periphery (e) and with dyes in the core (f). The monitoring wavelengths were 500 nm and 540 nm for QDs and dyes, respectively.

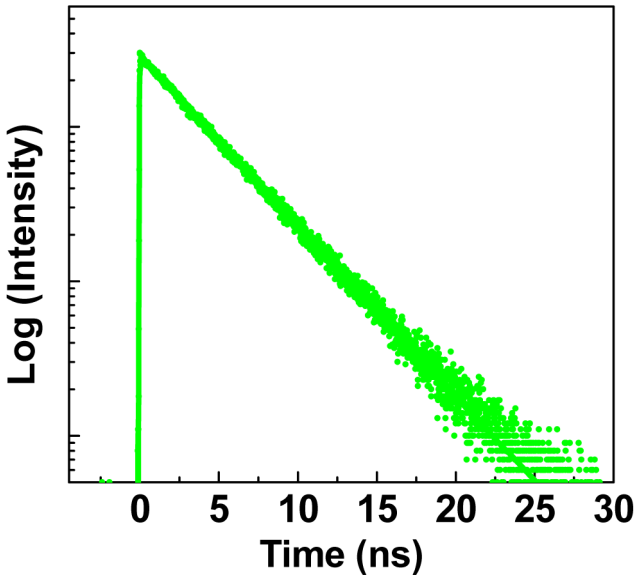

Figure 4.9. Time-resolved fluorescence spectrum of dye molecules in a dilute ethanol solution. The monitoring wavelength was 540 nm and the concentration was 1×10^{-5} M.

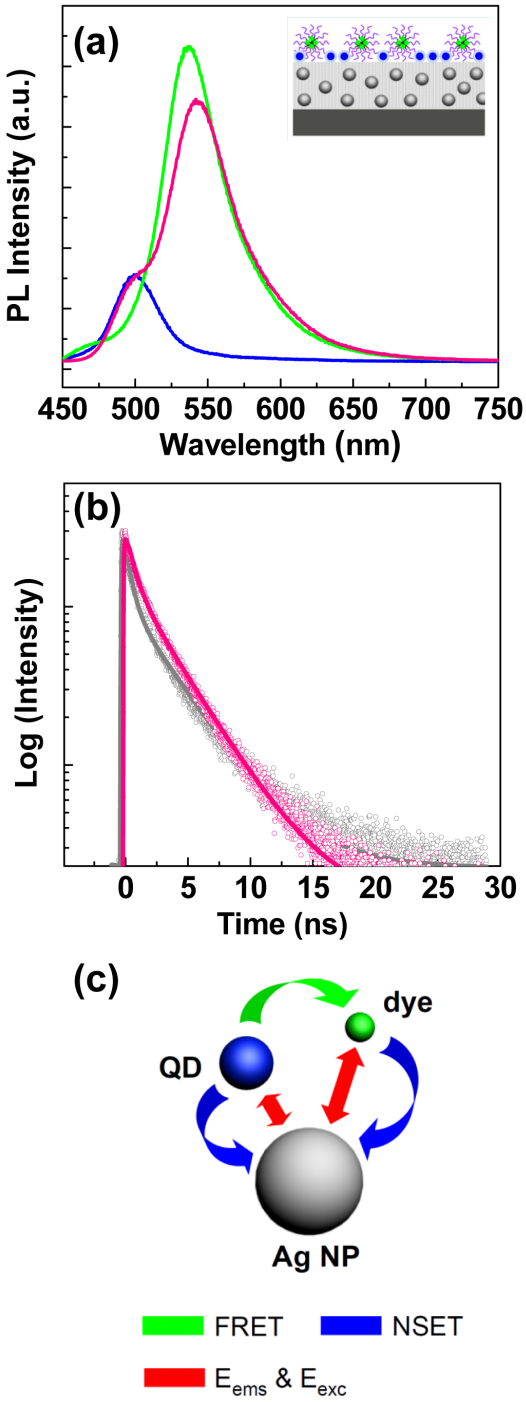

Figure 4.10 (a) Steady-state fluorescence spectra from a single-layered film of micelles on NP film with only QDs (blue), with only dyes (green), and with

QDs and dyes (pink). (b) Time-resolved fluorescence monitored at 500 nm from a single-layered film of micelles on the NPs film with only QDs (pink) and with QDs and dyes (gray). Multiexponential fits were included as solid lines. (c) Schematics of near-field interactions among QDs, dyes, and Ag NPs in the micellar hybrid. Green, blue, and red arrows were used for presenting FRET, NSET, and excitation/emission enhancement factors, respectively.

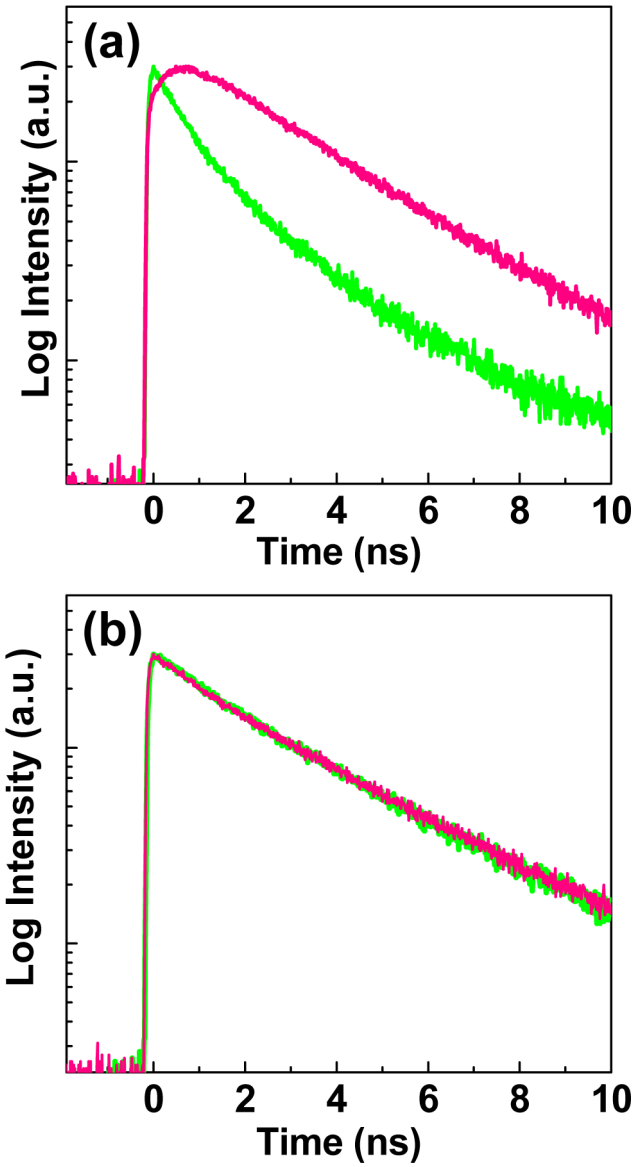

Figure 4.11. TRF spectra of dye acceptors from micellar film with only dyes (green) and with dyes and QDs (pink). (a) on a bare substrate; (b) on the NP film. The monitoring wavelength was 540 nm.

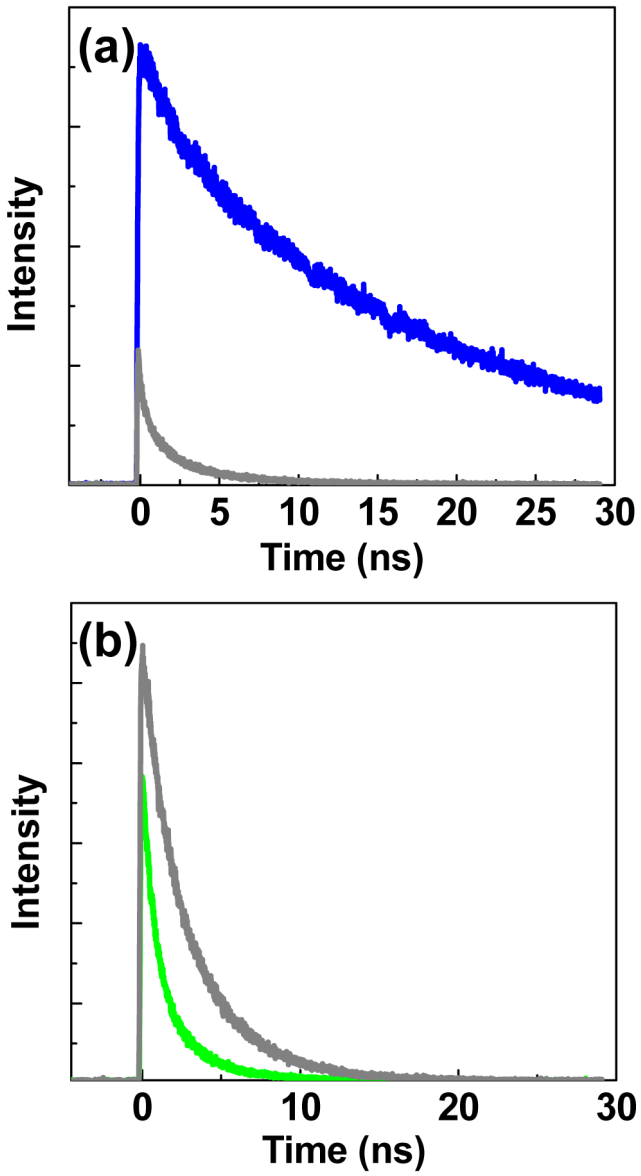

Figure 4.12. (a) Time-resolved fluorescence spectra from a micellar film with QDs in the periphery on a bare substrate (blue) and on the NP film (gray). (b) Time-resolved fluorescence spectra from a micellar film with dyes in the cores on a bare substrate (green) and on the NP film (gray).

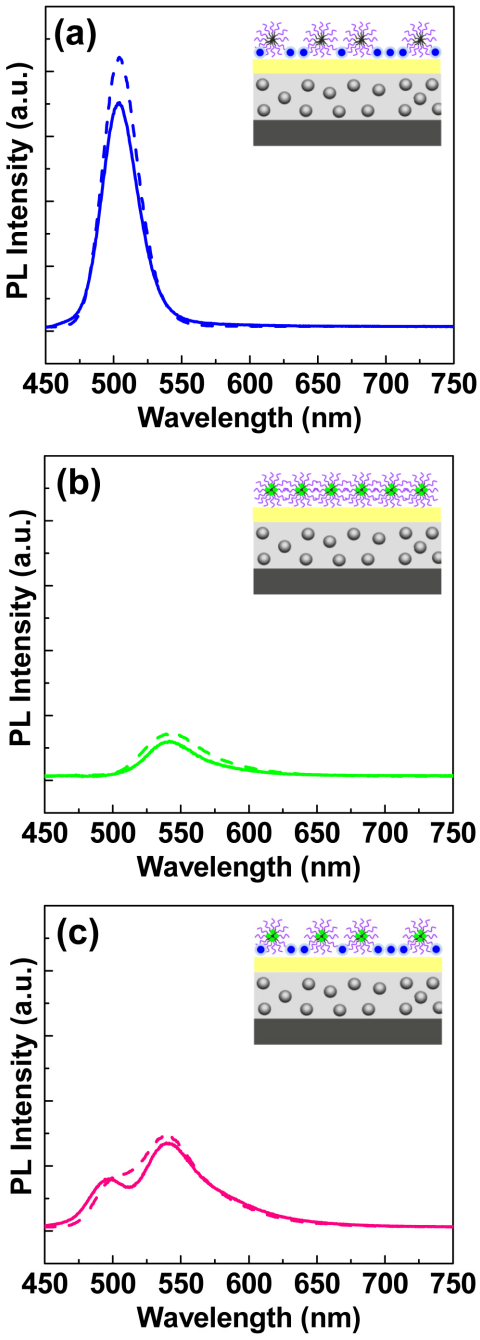

Figure 4.13. The influence of a spacer layer of P2VP. Steady-state fluorescence spectra were obtained from micellar film on a bare (dashed line) and P2VP/NP (solid line) substrates. (a) micelles with only QDs; (b) micelles with only dyes; (c) micelles with both QDs and dyes.

samples	α_1	τ_1 (ns)	α_2	τ_2 (ns)	α_3	τ_3 (ns)
dyes (bare)	0.358	0.62	0.642	2.70	-	-
dyes and QDs (bare)	-0.338	0.59	0.561	2.42	0.101	4.68
dyes (NP film)	0.093	0.75	0.907	3.42	-	-
dyes and QDs (NP film)	0.062	0.61	0.938	3.41	-	-

Table 4.1. Time components obtained from TRF spectra in Figure 4.11.

	E	E_{exc}	E_{ems}	k_{rad}^0 (ns^{-1})	k_{nr}^0 (ns^{-1})	k_{rad} (ns^{-1})	k_{nr} (ns^{-1})	k_{NSET} (ns^{-1})
QDs	0.16	5.7	0.028	0.038	0.008	0.009	0.008	0.373
Dyes	6.8	3.2	2.11	0.230	0.280	0.299	0.016	-

Table 4.2. Enhancement factors and rate constants of QDs and dyes in the absence and presence of the NP film. The subscript of 0 always indicates intrinsic variables in the absence of metal NPs.

Abstract (in Korean)

나노소재의 플라즈모닉 응용을 위한 자기조립 고분자에 관한 연구

김 기 세
화학부 고분자 전공
서울대학교 대학원

형광체, 반도체 양자점, 금속 나노입자와 같은 광기능성 나노소재간 광학적 커플링의 제어는 포토닉, 플라즈모닉, 나노, 바이오 시스템 등의 다양한 응용에 활용되고 있으며 소자 특성의 구현에 있어 중요한 역할을 한다. 예를 들어, 형광체, 전도성 고분자 등의 광기능성 소재는 유기 태양전지와 발광 다이오드 등을 포함한 광전자 소자에 활용되고 있는데, 이들 소자에서 형광소재간 커플링인 Fluorescence Resonance Energy Transfer (FRET)를 유도하게 되면 에너지 주개와 받개간 효과적인 빛의 흡수와 에너지 전달이 가능해져 광전자 소자의 효율을 향상시킬 수 있다. 또한, 이러한 형광소재간 커플링 뿐만 아니라 형광소재와 금속 나노입자간 커플링을 활용할 수도 있다. 즉, 금속 나노입자와 빛의 상호작용으로 금속 나노입자 표면 자유전하의 집단적인 진동에 의해 유도 되는 금속 나노입자의 Localized Surface Plasmon Resonances (LSPRs) 특성을 이용하면 나노입자 인근에 위치한 형광소재의 고유 특성인 발광 소멸속도 또는 비발광 소멸속도의 조절이 가능하여 형광증폭, 에

너지 전이 효율 증대, 금속 나노입자로의 에너지 전이, 유도방출 등의 독특한 발광특성을 구현할 수 있으며, 이러한 원리의 이해는 보다 다양한 응용에의 가능성을 갖게 한다.

형광체, 반도체 양자점, 금속 나노입자 상호간 광학적 커플링은 이들 상호간 상대적인 거리 및 위치에 크게 영향을 받기 때문에, 이러한 커플링 현상을 이용하여 형광체의 발광특성을 제어하기 위해서는 박막형태에서 광기능성 소재간 상대적인 위치에 대한 나노스케일 제어가 요구된다. 이를 위해 자기조립에 의해 나노구조 형성이 가능하여 다양한 기능성 소재의 도입 및 위치 제어가 가능한 블록공중합체 마이셀과 이온성 고분자의 Layer-by-Layer (LbL) 조립체를 활용할 수 있다.

본 연구에서는 나노스케일에서 정밀한 크기 조절이 가능한 블록공중합체 마이셀과 LbL 조립체의 나노구조를 활용하여 형광체, 반도체 양자점, 금속 나노입자 상호간 광학적 커플링을 조절하여 박막형태에서의 발광특성을 제어하였다.

제 1장에서는 이온성 고분자의 LbL 조립체를 활용하여 이종 형광체간 거리 및 위치를 조절하여 에너지 전이를 제어함으로써 박막형태에서 발광특성을 제어하였다. 에너지 전이 제어를 고려하여 스펙트럼 중첩이 있는 녹색 발광색의 Rhodamine 123 (R123)을 에너지 주개로 활용하고, 적색 발광색의 Rhodamine B (RB)를 에너지 받개로 활용하였다. 또한 박막형태에서 이들 형광체간 에너지 전

이를 제어하기 위해 이온성 고분자의 교대 적층에 의해 나노스케일의 박막 제조가 가능한 LbL 조립체를 활용하였으며, 박막내 형광체 도입을 고려하여 이온성 고분자와 형광체의 복합체를 제조하였다. 형광체가 도입된 이온성 고분자와 도입되지 않은 순수한 이온성 고분자를 스핀코팅 방법을 이용해 교대적층하여 박막을 제조하였다. 녹색 형광체 (R123)와 적색 형광체 (RB)의 상호간 거리 및 위치를 순수한 이온성 고분자의 교대적층 횟수로 조절하여 이들간 에너지 전이를 조절함으로써 박막형태에서 동시발광, 발광색 변환 등의 발광특성을 구현하였다.

제 2장에서는 박막형태에서 복수개의 형광체간 에너지 전이를 제어하여 단일 여기파장에서도 형광증폭, 증폭된 형광의 동시 발광 등의 발광특성을 구현하였다. 이를 위해 서로 다른 발광특성을 갖는 청색, 녹색, 적색의 형광체를 이온성 고분자 측쇄에 공유결합하여 순수한 이온성 고분자와 교대적층하여 LbL 조립체를 제조하였다. 청색 여기광원을 효과적으로 흡수하는 청색 형광체를 녹색과 적색 형광체 각각에 인접하게 위치하도록 적층하여 청색에서 녹색, 청색에서 적색으로의 에너지 전이를 유도함으로써 녹색, 적색 형광체의 형광증폭을 구현하였다. 또한 청색, 녹색 형광체와 청색, 적색 형광체가 인접하게 위치하도록 함과 동시에 이들간 거리를 조절하여 녹색 형광체에서 적색 형광체로의 에너지 전이를 제한함으로써 증폭된 녹색, 적색 형광의 동시 발광을 구현하였다.

제 3장에서는 블록공중합체 마이셀 나노구조를 활용하여 금속 나노입자와 형광체간 커플링을 제어함으로써 금속 나노입자의 플라즈몬에 의한 형광증폭을 구현하였다. 자기조립에 의해 코어 및 코로나의 나노구조를 형성하는 블록공중합체 마이셀에서 형광체는 마이셀 코어에 선택적인 도입이 가능하여 마이셀 코어에 위치한 형광체와 금속 나노입자는 마이셀 코로나에 의해 거리를 두고 위치하게 되며, 이들 상호간 거리는 블록공중합체의 분자량을 제어함으로써 조절이 가능하다. 이를 이용하여 은 나노입자가 코팅된 기판 위에 형광체가 도입된 마이셀 용액을 스핀코팅하여 은 나노입자와 함께 마이셀 단층박막을 제조하였다. 이렇게 제조된 형광체가 도입된 마이셀과 은 나노입자 박막으로부터 형광체의 발광증폭을 구현하였다. 또한 동일한 마이셀 나노구조에서 서로 다른 발광파장을 갖는 형광체 각각을 다른 마이셀 코어에 독립적으로 도입할 경우, 각각의 형광체는 마이셀 코로나에 의해 이격되어 에너지 전이가 제한되어 동시발광이 가능할 뿐만 아니라 이와 동시에 금속 나노입자의 플라즈몬에 의해 개별 형광체의 형광 증폭이 가능하여 박막형태에서 이종 형광체의 증폭된 형광의 동시발광을 구현하였다.

제 4장에서는 마이셀 나노구조 박막에서 형광체, 반도체 양자점, 금속 나노입자 상호간 거리 및 위치를 조절하여 이들 상호간 커플링을 제어하였다. 금속 나노입자 인근에 위치한 형광소재는 금속 나노입자의 플라즈몬 여기에 따른 국부적인 전기장의 증대와 그에

따른 발광 소멸 속도 또는 비발광 소멸속도 등의 변화에 의해 형광 증폭 또는 소광이 구현 되는데 이는 근접장에서의 형광소재간 커플링인 에너지 전이 현상과 유사하다. 따라서, 서로 다른 발광파장을 갖는 형광체와 반도체 양자점간 에너지 전이는 인접한 금속 나노입자에 의해 변화할 것으로 기대할 수 있으며, 마이셀 나노구조를 활용하여 형광체, 반도체 양자점, 금속 나노입자의 상호간 위치 및 거리를 나노스케일에서 제어하여 에너지 주개인 반도체 양자점에서 에너지 받개인 형광체로의 에너지 전이가 금속 나노입자에 의해 제한 될 수 있음을 확인하였다. 이러한 연구 결과는 상향식 나노기술의 기본 개념인 자기조립 고분자가 형성하는 나노구조를 조절하여 광학 특성을 제어하는 연구이고, 서로 다른 종류의 소재간 커플링 효과를 제어하여 발광 파장과 발광 세기 등을 조절하는 연구이기에 상호의존 특성에 의한 광학특성 구현을 가능하게 하여 광전자 디바이스, 바이오 센서 등의 분야에 응용이 가능한 원천 기술을 제공할 수 있을 것으로 전망한다.

주요어: 자기조립, 블록공중합체 마이셀, 이온성 다층박막 자기조립체, 형광, 표면 플라즈몬

학 번: 2006-20355

Abstract (in German)

Selbstorganisierende Polymere zur Anwendung von Plasmonen in Nanostrukturierten Materialien

Ki-Se Kim
Institut für Chemie
Graduiertenschule
Seoul National University

Die Kontrolle von Nahfeld-Wechselwirkungen von Fluoreszenzfarbstoffen, halbleitenden Quantenpunkten und Metall-Nanopartikeln spielt eine Schlüsselrolle für einen großen Anwendungsbereich. Beispiele dafür finden sich in photonischen, plasmonischen, nanotechnologischen und biologischen Systemen. So wird die als Fluoreszenz Resonanter Energie Transfer (FRET) bezeichnete Wechselwirkung zwischen mehreren Farbstoffen bereits in optoelektronischen Elementen eingesetzt, wie den organischen Solarzellen sowie in Leuchtdioden, in denen eine effiziente Quantenausbeute und der Energietransfer von Donor zu Akzeptor eine entscheidende Rolle für die Effizienz des Elements spielen. Weiterhin kam der kollektiven Oszillation von Elektronen in Metall-Nanopartikeln, die als lokalisierte Oberflächenplasmonenresonanz bezeichnet wird, große Aufmerksamkeit zu, da die Wechselwirkung zwischen Licht und Materie durch das Einfügen von Metallnanopartikeln in die Umgebung eines

Fluorophors oder eines Fluoreszenzfarbstoffes, eines Quantenpunktes oder eines konjugierten Polymers gezielt beeinflusst werden kann. Lokalisierte Oberflächenplasmonenresonanz bewirkt eine deutliche Erhöhung der lokalen Felder in der Nähe der Metall-Nanopartikel und beeinflusst somit strahlende und nicht strahlende Übergänge von Fluorophoren. Dies führt zu fundamentalen, interessanten Phänomenen wie der Plasmonisch Verstärkten Fluoreszenz, dem Plasmonisch Verstärkten FRET, dem Nanometall Oberflächen Energie Transfer, den Oberflächenplasmonen durch stimulierte Emission von Strahlung und vielen mehr. Als Konsequenz der Kenntnis über diese Vorgänge ermöglichen sich umfangreiche Möglichkeiten der Anwendung in der Optoelektronik, der Optik, dem Cell-Imaging und der Biologie. Da die Kopplung von Fluoreszenzfarbstoffen, Quantenpunkten und Metall-Nanopartikeln stark von dem gegenseitigen Abstand und der Position im Nanometerbereich abhängt, ist die genaue Kontrolle der relativen Lage in dünnen Filmen entscheidend für neuartige Photolumineszenzeigenschaften in photonischen Anwendungen.

Die Selbstorganisation von Blockcopolymer-Mizellen und Layer-by-Layer (LbL) Anordnung von Polyelektrolyten sind vielversprechende Möglichkeiten um die Position von photoaktiven Spezies innerhalb eines dünnen Films mit einer auf Nanometer Ebene hohen Genauigkeit effektiv zu kontrollieren.

In dieser Arbeit wird dargelegt, wie Nanostrukturen von selbstorganisierten Polymeren zur effektiven Kontrolle von Nahfeld-Wechselwirkungen wie FRET, Nanometall Oberflächen Energie Transfer und

Oberflächenplasmonen gekoppelte Fluoreszenz zwischen photoaktivem Nanomaterial in dünnen Filmen genutzt werden können.

In Kapitel 1 wird die kontrollierte Fluoreszenz innerhalb eines dünnen Films zweier in unterschiedlichen Schichten eines LbL -Systems eingearbeiteten Farbstoffe beschrieben. Aufgrund der spektralen Überlappung wurden Rhodamin 123 (R123) und Rhodamin B (RB) als Donor bzw. Akzeptor ausgewählt. Zur Herstellung eines mehrlagigen dünnen Filmes wurde ein Komplex des jeweiligen Farbstoffes mit Natrium-Polystyrol-4-sulfonat (PSS-R123 und PSS-RB) dargestellt und anschließend alternierend mit Polyallylamin-Hydrochlorid (PAH) durch Rotationsbeschichtung auf einen Träger aufgebracht. Die LbL Anordnung wurde in der Reihenfolge [PAH/PSS-RB]/[PAH/PSS]$_n$/[PAH/PSS-R123] angefertigt. Da der Abstand zwischen R123 und RB durch die zwischen den Farbstoffkomplexen befindlichen Anzahl an Doppelschichten [PAH/PSS] (n) exakt kontrolliert werden kann, ist es durch die Kontrolle der Effizienz des Energietransfers möglich die Emission von Licht des dünnen Filmes zu regulieren.

In Kapitel 2 wird die exakte Kontrolle von mehrfachem FRET innerhalb einer LbL Anordnung beschrieben, deren Ziel eine gleichzeitige Emission mit erhöhter Intensität mehrerer Farbstoffe bei nur einer Anregungswellenlänge im blauen Bereich des Lichts ist. Drei verschiedene Fluoreszenzfarbstoffe werden dabei mit einem Polyelektrolyten verbunden und dann in einem LbL System eingebracht. So wird ein Farbstoff, der im blauen Lichtbereich absorbiert, in einer Schicht eingebracht, die in der Nähe von Schichten mit grün emittierenden bzw. rot emittierenden Farbstoffen liegt,

wobei die emittierenden Farbstoffe durch das Einbringen von reinen Polyelektrolytschichten so weit voneinander getrennt sind, dass die Distanz außerhalb deren Försterradius liegt. Diese LbL Anordnung gestattet daher einerseits FRET zwischen dem absorbierenden Farbstoff und den emittierenden Farbstoffen, verhindert aber andererseits FRET zwischen den emittierenden Farbstoffen, sodass eine gleichzeitig verstärkte Emission des grünen und roten Farbstoffes ermöglicht wird.

Die intensive Korrelation zwischen Mizellen und Oberflächenplasmonen gekoppelter Fluoreszenz wird in Kapitel 3 erläutert. Die Entmischung von Blockcopolymer-Mizellen ermöglicht das Einbringen von Fluorophoren in die Nähe von Metall-Nanopartikeln um dadurch eine Verstärkung der Fluoreszenz zu ermöglichen, was durch andere Anordnungsmethoden nicht trivial zu erreichen wäre. Es wird ein Film aus einer einzelnen Schicht von Blockcopolymer-Mizellen mit Farbstoff auf einem mit Silber-Nanopartikeln beschichteten Substrat aufgetragen. In diesem Film befinden sich die Farbstoffe im Kern der Mizelle, wohingegen die Silber-Nanopartikel um die Corona der Mizelle herum angeordnet sind. Dadurch kann der Abstand zwischen Farbstoff und Nanopartikel durch das Festlegen der Blockcopolymer-Mizelle kontrolliert werden um Fluoreszenzverstärkung durch die Silber Nanopartikel zu erhalten. Darüber hinaus kann mit derselben Nanostruktur der Mizellen eine gleichzeitige Emission zweier verschiedener Farbstoffe mit erhöhter Intensität erreicht werden, indem die unterschiedlichen Farbstoffe getrennt in verschiedenen Mizellen eingebracht werden, wobei die Corona der Mizellen verhindert, dass

FRET auftritt. Durch diese Fähigkeiten von Blockcopolymer-Mizellen bestehen viele Möglichkeiten der plasmonischen Anwendungen. Als zukunftsweisende Richtung sei auf die chemische Modifikation der Copolymere hingewiesen, auf denen ein dünner Metallfilm abgeschieden werden könnte. Indem die Corona einer Mizelle, welche Farbstoffe im Kern der Mizelle enthielte, mit einer Metallschale beschichtet würde, könnten beide Funktionen des Plasmons und der Fluoreszenz erhalten werden, was eine vielversprechende Möglichkeit für Cell-Imaging und in der Diagnostik wäre.

In Kapitel 4 wird die Nahfeldwechselwirkung unter Quantenpunkten, Farbstoffen und Metall-Nanopartikeln in nanostrukturierten mizellaren dünnen Filmen beschrieben. Bekanntermaßen kann die Oberflächenplasmonenresonanz von Metall Nanopartikeln die intrinsischen Eigenschaften von in der Nähe befindlichen Farbstoffen verändern. Feldverstärkung und das Modullieren von strahlenden Übergängen sind wichtige Grundlagen zum Verständnis zahlreicher experimenteller Befunde wie dem Verstärken und dem Verringern der Emission der in der Nähe von Metall-Nanopartikeln befindlichen Fluorophore. Es gibt offenbar Ähnlichkeiten zwischen Oberflächenplasmonen gekoppelter Fluoreszenz und FRET, zumal beide räumliche Nahfeld-Wechselwirkungen sind. Daher wird hier die Hypothese aufgestellt, dass die Donor-Akzeptor Wechselwirkung des FRET durch die Anwesenheit von Metall-Nanopartikeln verändert werden kann. Als hier beschriebener Ansatz werden Diblockcopolymer-Mizellen verwendet, welche eine weite Anwendung in der nanoskalierten Anordnung von funktionellem Material finden. Durch das Anwenden von

Selbstorganisations-Techniken von Copolymer-Mizellen kann die räumliche Anordnung von halbleitenden Quantenpunkten, Fluoreszenz-Farbstoffen und Metall-Nanopartikeln beeinflusst werden, wodurch FRET in Hybrid Anordnungen durch plasmonische Effekte ausgeschaltet werden kann.

Schlüsselwörter: Selbstorganisation, Blockcopolymer-Mizellen, Layer-by-Layer Anordnung, Fluoreszenz, Oberfläche Plasmon

Matrikelnummer: 2006-20355

Curriculum Vitae

Name: Ki-Se Kim

Date of Birth: November 25, 1980.

Educations

2006. 3 ~ 2012. 8 Seoul National University, Ph. D degree in the Department of Chemistry (Polymer Chemistry)
University of Mainz, Joint Ph. D. degree in the Department of Chemistry, Pharmacy and Geosciences
Thesis: Self-Assembling Polymers for Plasmonic Applications in Nanostructured Materials

1999. 3 ~ 2006. 2 Kyungpook National University, Bachelor's degree in the Department of Polymer Science & Engineering

Publications

<International>

[1] **K. S. Kim**, J. H. Kim, H. Kim, F. Laquai, S. I. Yoo, B. H. Sohn "Plasmon-Enhanced Simultaneous Emission in a Single-Layered Assembly of Micelle-Encapsulated Fluorophores and Metal Nanoparticles" submitted (*Adv. Funct. Mater.*) , **2012**

[2] **K. S. Kim**, J. H. Kim, H. Kim, F. Laquai, E. Arifin, J. K. Lee, S. I. Yoo, B. H. Sohn "Switching Off FRET in the Hybrid Assemblies of Diblock Copolymer Micelles, Quantum Dots, and Dyes by Plasmonic Nanoparticles" Accepted in *ACS Nano,* **2012**

[3] **K. S. Kim**, S. I. Yoo, M. Kim, B. H. Sohn "Controlled Fluorescence Resonance Energy Tranansfer from Multiple Fluorophores in Layer-by-Layer Assemblies" *Macromol. Chem. Phys.* **2010**, *211*, 2382.

[4] **K. S. Kim**, S. I. Yoo; T. S. Lee, B. H. Sohn "Controlled Light Emission in Spin-Assisted Layer-by-Layer Assemblies with Fluorophores" *J. Nanosci. Nanotechnol.* **2010**, *10*, 6896.

[5] J. H. Kim, **K. S. Kim**, S. I. Yoo, B. H. Sohn "Dispersion of Micelle-Encapsulated Fluorophores in a Polymer Matrix for Control of Color of Light Emitted by Light-Emitting Diodes" *Thin Solid Films,* **2011**, *519*, 8161

[6] N. Haberkon, S. Kim, **K. S. Kim**, M. Sommer, M. Thelakkat, B. H. Sohn, P. Theato "Template-Assisted Fabrication of Highly Ordered Interpenetrating Polymeric Donor/Acceptor Nanostructures for Photovoltaic Applications" *Macromol. Chem. Phys.* **2011**, *212*, 2142.

[7] S. M. Jeon, **K. S. Kim**, S. I. Yoo, B. H. Sohn "Controlled Fluorescence Resonance Energy Transfer between ZnO Nanoparticles and Fluorophores in Layer-by-Layer Assemblies" *J. Nanosci. Nanotechnol.* **2010**, *10*, 6819.

[8] P. J. Roth, **K. S. Kim**, S. H. Bae, B. H. Sohn, P. Theato, R. Zentel "Hetero-Telechelic Dye-Labeled Polymer for Nanoparticle Decoration" *Macromol.Rapid Commun.* **2009**, *30*, 1274.

[9] S. I. Yoo, S. H. Bae, **K. S. Kim**, B. H. Sohn "Nanostructures of Diblock Copolymer Micelles for Controlled Fluorescence Resonance Energy Transfer" *Soft Mater.* **2009**, *5*, 2990.

[10] S. I. Yoo, S. J. An, G. H. Choi, **K. S. Kim**, G. C. Yi, W. C. Zin, J. C. Jung, B. H. Sohn "Controlled Light Emission by Nanoencapsulation of Fluorophores in Thin Films of Diblock Copolymer Micelles" *Adv. Mater.* **2006**, *46*, 6595.

Patents

<Domestic>

[1] **K. S. Kim**, H. Kim, B. H. Sohn, "내 오염성이 우수한 역삼투 분리막 및 그 제조방법" 2011. 10. 06.(특허 출원)

[2] S. I. Yoo, K. S. Kim, B. H. Sohn, "블록공중합체 마이셀을 이용한 형광체층 형성 방법" 2010.08.05.(특허 등록)

Presentations

<International>

[1] **K. S. Kim**, B. H. Sohn "Nanoscale Assembly of Fluorophores and Metal Nanoparticles by Nanostructures of Block Copolymer Micelles for Plasmon Enhanced Emission" *Materials Research Society Meeting*, Boston, MA, USA, **2011**.

[2] **K. S. Kim**, B. H. Sohn "Coupling between metal nanoparticles and fluorescent dyes with layer-by-layer assembled polymer films" *International Chemical Congress of Pacific Basin Societies*, Honolulu, Hawaii, USA, **2010**.

[3] **K. S. Kim**, B. H. Sohn "Nanostructured Multilayers of Fluorophore-Labeled Polyelectrolytes for Controlled Fluorescence Resonance Energy Transfer" *Research Training Group Symposium*, Mainz, Germany, **2009**.

[4] **K. S. Kim**, S. M. Jeon, B. H. Sohn "Layer-by-Layer Assembled Thin Films of Fluorophore-Labeled Polyelectrolytes for Controlled Fluorescence Energy Transfer" *American Chemical Society, Philadelphia, PA, USA,* **2008.**

[5] **K. S. Kim**, S. I. Yoo, B. H. Sohn "Spin-Assisted Assembly of Multilayers of Polyelectrolytes with Fluorophores" *American Chemical Society, Boston, MA, USA,* **2007.**

<Domestic>

[1] **K. S. Kim**, B. H. Sohn "Surface Plasmon Enhanced Emission of Fluorophores by Micellar Nanostructures on Metal Nanoparticles" *International Research Training Group Symposium*, Seoul, **2011**.

[2] **K. S. Kim**, B. H. Sohn "Layer-by-Layer Assembly of Fluorophore-Labeled Polyelectrolyte" *International Research Training Group Symposium*, Seoul, **2009**.

[3] **K. S. Kim**, S. I. Yoo, J. H. Lee, B. H. Sohn "Layer-by-Layer Assembly of Fluorophore-Labeled Polyelectrolytes" *The Polymer Society of Korea*, Daejon, **2008**.

[4] **K. S. Kim**, S. I. Yoo, B. H. Sohn "Controlled Light Emission from Spin-Assembled Thin Films" *The Polymer Society of Korea*, Jeju, **2007**.

[5] **K. S. Kim**, B. H. Sohn "Fabrication of Polyelectrolyte Multilayers with Fluorophores" *The Korean Chemical Society*, Daegu, **2007**.